Seeing the unseen: Inferring dark matter subhalo properties from stellar streams

---

Tariq Hilmi
URN: 6366559
Supervisor: Dr. Denis Erkal
Co-Supervisor: Prof. Justin Read

Astrophysics PhD
University of Surrey
April 5, 2024

Declaration

This thesis and the work to which it refers are the results of my own efforts. Any ideas, data, images or text resulting from the work of others (whether published or unpublished) are fully identified as such within the work and attributed to their originator in the text, bibliography or in footnotes. This thesis has not been submitted in whole or in part for any other academic degree or professional qualification. I agree that the University has the right to submit my work to the plagiarism detection service TurnitinUK for originality checks. Whether or not drafts have been so assessed, the University reserves the right to require an electronic version of the final document (as submitted) for assessment as above.

The work has appeared or will appear in the following scientific publication:
Inferring dark matter subhalo properties from simulated subhalo-stream encounters, Hilmi, Tariq ; Erkal, Denis ; Koposov, Sergey E. ; Li, Ting S. ; Lilleengen, Sophia ; Ji, Alexander P. ; Lewis, Geraint F. ; Shipp, Nora ; Pace, Andrew B. ; Zucker, Daniel B. ; Limberg, Guilherme ; Usman, Sam A.

Abstract

With stellar stream discoveries increasing dramatically in the past decade, a vast assortment of perturbed streams have allowed us to constrain properties of both baryonic structure in the halo along with the Milky Way history in general. In this thesis, I primarily pursue a promising aspect of streams of probing for dark matter substructure. The abundances and masses of dark matter substructure in galaxies is highly dependent on the nature of the dark matter particle, and streams may allow us to recover their properties, in turn better constraining the dark matter particle. In the process of this, I first demonstrate that by using mock streams generated in realistic Milky Way potentials, we can use observations of a perturbed stream track to recover subhalo properties. This includes present day realistic observations we can expect from photometric and spectroscopic data from Gaia and the Dark Energy Survey. This had only been demonstrated on circular orbits using the analytic impulse approximation prior to this. With this proof of concept shown, I explore how this can be done with real data including the ATLAS-Aliqa Uma stream, which has a very significant kink along its track with features in its radial velocities associated with it too. I improve upon typical likelihood estimation on streams using Kernel Density Estimation, to best consider their 2-dimensional on sky structure. While unsuccessful in producing quantitative fits, I reveal new styles of subhalo-stream interactions which can leave kink like features or spurs from very old impacts between subhaloes and streams. As a result, I show that the nature of a streams morphology and kinematics could potentially help decipher the nature of a potential subhalo-stream encounter. Additionally, I discuss additional parameters we should consider for future fits to these encounters to some real streams such as ATLAS-ALiqa Uma. Most important is likely the progenitor properties, which can affect properties such as the stream orientation, width and velocity dispersion. Finally, I explore how the Galactic bar and spiral structure, including a newer, more accurate bar model, could affect streams such as ATLAS-Aliqa Uma, which has an apocentre of $\sim$ 40 kpc but relatively close pericentre of $\sim$ 13 kpc. We confirm with previous work that they cannot produce the kink. On one instance though, they slightly influenced the orientation of the track. This could play a role in fitting streams as this could affect progenitor properties. While the focus of the work here is on fitting dark matter subhaloes due to the implications of the subhalo properties on constraining the dark matter particle, the findings of these baryonic structures hint at how streams could be used more in the future to in turn, provide better constraints on these structures.

Acknowledgements

The PhD experience as a whole has been a great time and there are so many people to thank. I first must acknowledge my primary supervisor, Dr. Denis Erkal, who made all this possible. The endless guidance from him and ideas kept me busy with interesting research even when things didn't work out. I always appreciated how much care he always had for how myself, and his other students were getting along especially during the lockdown period. Many thanks also go out to my secondary supervisor, Prof. Justin Read, who would be an endless fount of knowledge and new ideas which were always interesting to hear about. It will be a shame that we could not try every idea he had but it would always help in making my research sound very important.

The Astrophysics group as a whole has been great to be part of and it will be sad to leave them. In particular I am thankful to everyone in my cohort who started together, and made the start and end of the PhD in particular a great time in spite of anything we may have been going through. I really feel I've made the most of my time here thanks to them, and the wider astrophysics group as a whole. Special thanks also go out to my office, the many coffees we did, arguably insightful discussions and works of art on the whiteboard.

Lockdown was obviously a big impact on everyone for both their work and social life, so I would like to thank, Kate, my housemate, member of the astrophysics group and all round a great person. All things considered, many parts of lockdown still remained a pretty fun time. I may only remember about 5% of the films we watched most evenings, but it wouldn't have been the same living in Guildford without you.

My time at Surrey definitely wouldn't have been the same if I had never learned to Scuba dive with the Scuba Society. It definitely made for finding different loves I have in life outside of research, and big thanks go out to my regular dive buddies, Arman, Bertie and Andrew for all the fun. Our underwater adventures and wonderful encounters with many a crab will not be forgotten.

Finally, my thanks go out to my family, and my mum and dad's unconditional support on what I wanted to do since first applying to University. This is certainly not how I thought doing a physics would end up but it's been a wonderful time and it's all thanks to you too.

Contents

Abbreviations **ix**

1 Introduction **1**

1.1 Dark matter and galaxy structure . . . 1
  1.1.1 Galaxy formation through hierarchical clustering . . . 1
  1.1.2 The Cold Dark Matter paradigm . . . 2
  1.1.3 Alternate dark matter particles . . . 3
    Warm Dark Matter . . . 3
    Fuzzy Dark Matter . . . 5
    Self Interacting Dark Matter (SIDM) . . . 6
    Alternate models to dark matter . . . 6
1.2 An overview of MW structure . . . 6
  1.2.1 The disk . . . 7
    The Galactic Bar . . . 8
    Spiral structure . . . 8
  1.2.2 The halo and its satellites . . . 9
    The Sagittarius dwarf galaxy and stream . . . 10
    The Large Magellanic Cloud . . . 10
1.3 Stellar streams . . . 11
  1.3.1 Observations of streams . . . 12
  1.3.2 The tidal radius . . . 13
  1.3.3 Stellar stream formation . . . 16
  1.3.4 Perturbations to stellar streams . . . 17
1.4 Constraining dark matter substructure . . . 17
  1.4.1 Stellar streams as probes for dark matter substructure . . . 18
    Analytic solutions to subhalo-stream encounters . . . 19
    Simulating subhaloes with streams . . . 21
    The modified Lagrange Cloud Stripping method . . . 21
    Thesis structure . . . 22

2 Inferring dark matter subhalo properties from simulated subhalo-stream encounters **24**

2.1 Abstract . . . 24
2.2 Introduction . . . 25
2.3 An overview of the setup . . . 27
  2.3.1 Generating an unperturbed stream . . . 27
  2.3.2 Modelling the subhalo-stream encounter . . . 30

2.3.3 Generating the perturbed stream 30
2.4 Fitting subhalo properties 31
2.4.1 The mock impact 31
Scenario 1: No observational errors 33
Scenario 2: Present day observational error 33
Scenario 3: Future predicted observational errors 33
2.4.2 Likelihood Estimation 34
2.4.3 A recent impact time 36
2.5 MCMC Analysis 36
2.5.1 Scenario 1: Fits with no observational errors 38
2.5.2 Scenario 2: Fits using current observational uncertainties 39
2.5.3 Scenario 3: Fits using future observational uncertainties 39
2.6 Discussion 45
2.6.1 Subhalo Localisation 45
2.6.2 Information content of perturbed streams 45
2.7 Conclusions 46
2.8 Acknowledgements 47
2.9 Data Availability 47

3 Measuring the properties of a Milky Way subhalo with the ATLAS-Aliqa Uma stream 52
3.0.1 Advances in AAU observations 52
3.1 Changes to the encounter setup 54
3.2 Fitting the perturbed stream 54
3.2.1 Restriction of the simulated data 55
3.2.2 Modifications to the likelihood 55
Kernel Density Estimates about the kink 55
3.3 A stochastic exploration of parameter space 59
3.4 MCMC fits of the kink 59
3.4.1 Exploration and fits using dynesty 60
3.4.2 Fits using emcee 61
3.5 The potential nature of a subhalo encounter with the AAU stream 61
3.5.1 A recent encounter from a dense, compact object 61
3.5.2 A very old encounter further along the stream 64
3.6 Discussion 64
3.6.1 The qualitative fits to AAU 64
Subhalo properties 68
3.6.2 MCMC fits 71
Limitations to the likelihood estimation 74
Additional parameter exploration 76
3.7 Conclusions 76

4 An exploration of the baryonic candidates of AAU 78
4.1 Perturbations from the disk 78
4.1.1 Spiral Structure using the Cox & Gomez potential 79
4.1.2 Galactic bars using the McGough potential 82
4.2 Results & Discussion 86
4.2.1 Spiral structure 86

4.2.2 Galactic bar 90
4.3 Conclusions 91
4.3.1 Use of the McGough bar 93

5 Conclusions **94**
5.1 Future work 95

List of Figures

1.1 Dark matter clumps under Cold Dark Matter versus Warm Dark Matter . . 2
1.2 The subhalo mass function under different dark matter paradigms 4
1.3 A simple representation of galaxy structure under barred spiral galaxies . . 9
1.4 The appearance of the Sagittarius dwarf galaxy and stream 11
1.5 Typical detection of stellar streams using a simple RGB composite plot . . . 14
1.6 The behaviour of stars stripped from their progenitor stream 15
1.7 The formation of a stream gap following a subhalo encounter 20

2.1 The subhalo-stream encounter setup and parameters 29
2.2 Our mock perturbed stream compared to the same stream generated without a subhalo-stream encounter 31
2.3 How our mock encounter compares to observed ATLAS-Aliqa Uma data . . 32
2.4 The expected amount of data available of the ATLAS-Aliqa Uma stream from 4MOST and the Large Synoptic Survey Telescope 35
2.5 The positions of nearby stream particles after one is perturbed in its velocity or distance modulus 37
2.6 A corner plot of our subhalo fits to a stream with no observational errors . . 40
2.7 A corner plot of our subhalo fits to a stream with present day like observational errors 41
2.8 A corner plot of our subhalo fits to a stream with predicted future observational errors from 4MOST and Gaia DR5 42
2.9 The recovery of the mass and scale radius for subhalo fits under different qualities of observational data 43
2.10 The recovery of present day sky positions for subhaloes when fit using different qualities of observational data 44
2.11 Our mock perturbed stream and its observables data for the no error scenario 48
2.12 Our mock perturbed stream and its observables data for the present day error scenario 49
2.13 Our mock perturbed stream and its observables data for the future predicted error scenario 50
2.14 Recovery of subhalo positions in galactocentric coordinates 51

3.1 Newer observations to the AAU stream 53
3.2 Kernel Density Estimation at the ATLAS-Aliqa Uma kink for a recent, very dense subhalo 56
3.3 A comparison of the kernel type used in our Kernel Density Estimation . . . 57
3.4 Stream observables for a recent, very dense subhalo interaction 62
3.5 Track and velocity dispersions for a recent, very dense subhalo interaction . 63

3.6 Key stream observables for an older subhalo-stream encounter further up the stream . . . 65
3.7 Kernel Density Estimation at the ATLAS-Aliqa Uma kink for a much older subhalo encounter . . . 66
3.8 Velocity features at the kink for an older impact . . . 67
3.9 The sky positions of stream and subhalo for the recent impact . . . 69
3.10 The sky positions of stream and subhalo for the older impact . . . 70
3.11 The impact location along the stream for the older subhalo-stream encounter 71
3.12 The orientation of the subhalo angular momentum compared to Sagittarius 72
3.13 Key stream observables for the MCMC fit . . . 73
3.14 Kernel Density Estimation at the ATLAS-Aliqa Uma kink for the MCMC fit 74
3.15 Velocity features at the kink for the MCMC fit . . . 75

4.1 A face-on view of our 2 and 4-armed Cox & Gomez spiral structure . . . 80
4.2 A radial density profile of our Cox & Gomez spiral structure . . . 81
4.3 A face-on view of our implemented McGough bar potential . . . 83
4.4 A density profile of our implemented McGough bar potential along both its major and minor axis . . . 84
4.5 The dispersions of an unperturbed AAU progenitor fit . . . 87
4.6 A comparison between the fiducial Cox & Gomez spiral setup and fast rotating spirals . . . 88
4.7 Differences in stream track and radial velocities due to the different spiral arm setups . . . 89
4.8 A comparison between the fiducial McGough bar setup and our MW like bar 91
4.9 Differences in stream track and radial velocities due to the different bar setups 92

Abbreviations

4MOST	4-metre Multi-Object Spectroscopic Telescope
AAU	ATLAS-Aliqa Uma
CDM	Cold Dark Matter
CMD	Colour Magnitude Diagram
DESI	Dark Energy Spectroscopic Instrument
DES	Dark Energy Survey
FDM	Fuzzy Dark Matter
GC	Globular Cluster
KDE	Kernel Density Estimation
LMC	Large Magellanic Cloud
LSST	Large Synoptic Survey Telescope
MCMC	Markov-Chain Monte Carlo
MW	Milky Way
RGB	Red Giant Branch
SDSS	Sloan Digital Sky Survey
S5	Southern Stellar Stream Spectroscopic Survey
WDM	Warm Dark Matter

Chapter 1

Introduction

1.1 Dark matter and galaxy structure

The concept of dark matter stems early on from observations of galaxy clusters. The velocity dispersion of these galaxies in the cluster was unusually high, far higher than what should be expected given their visible mass and following Newtonian dynamics. Even accounting for dust and gas that would have been difficult to observe at the time, their masses would not be able to explain the observed velocity dispersion here without the introduction of an invisible, non-baryonic mass now classified as dark matter (Zwicky, 1933). We later found within galaxies themselves, that stars in the disk follow a flat rotation curve. On the plane of the disks of galaxies, beyond a few kpc from the galactic centre, the circular velocities of stars flattens out to the same velocity regardless of their distance to the centre. This feature of galaxies could be explained using dark matter if we were to follow Newtonian dynamics, further cementing the idea (Rubin et al., 1982b,a; Debattista & Sellwood, 1998; Sofue & Rubin, 2001). Gravitational lensing is another technique that has been found to support dark matter, where the curving of light around galaxy clusters once again required far higher masses than could be observed (Tyson et al., 1998). Using lensing, we also had found a significant piece of evidence in favour of dark matter in the form of the bullet cluster. Here, during the collision between two galaxy clusters, most of their visible baryonic mass in the form of hot gas collided and compressed, while the collisionless matter in the form of stars and any potential dark matter passed through eachother. The points of strongest lensing, hence, greatest mass however was not concentrated in the centre where the gas collided, instead being located where the stars and dark matter haloes would be, which further supported how most of galaxy mass was dark matter (Clowe et al., 2006). Now, with enough evidence mounted, dark matter is a widely accepted theory on our understanding of the Universe and plays a very important role on galaxy formation and evolution, making up ∼80% of the mass of the Universe (Garrett & Dūda, 2011).

1.1.1 Galaxy formation through hierarchical clustering

Following most modern models of dark matter, there is a general agreement on how galaxies form through the hierarchical clustering of dark matter haloes. During this process, we end up with larger and larger dark matter haloes which start attracting baryonic matter, eventually reaching a large enough size to spark star formation (White & Rees, 1978). The first signs of this process stem from our very own Galaxy, with the presence of massive ob-

Figure 1.1: A comparison between dark matter haloes of a MW-like galaxy of 2 different dark matter models, Cold Dark Matter (left) and Warm Dark Matter (right). Each plot showcases a region of 1.5x1.5 Mpc. The differences in substructure between models is shown, with cold dark matter forming high numbers of clumps throughout the halo with high variance in size, while the warm dark matter halo features only the larger subhaloes and the smaller subhaloes have been washed out in the early Universe. Image adapted from Mark Lovell et al. (2012), Figure 3 (Lovell et al., 2012).

jects orbiting it including Magellanic Clouds and other classical satellites, each showcasing vastly different masses to one another. Later, observations of the Sagittarius dwarf galaxy shows a merger event taking place in the night sky, with such intense tidal interactions from its close encounters with the Milky Way (MW) stripping stars to also create the Sagittarius stream (Ibata et al., 1994). Since then, even on smaller scales than a dwarf galaxy as large as Sagittarius, we now have found that other stellar streams nearby the sun which reveal how they had past mergers with the MW too (Helmi et al., 1999). We also have found numerous remnants of past mergers, the most notable being the Gaia-Enceladus dwarf galaxy which is believed to have merged into the MW roughly 10 Gyr ago and even given rise to structures such as our thin and thick disk (Belokurov et al., 2018; Helmi et al., 2018).

1.1.2 The Cold Dark Matter paradigm

The Lambda Cold Dark Matter (CDM) theory in particular is the leading model we use. The importance of this dark matter particle compared to other theories such as Warm Dark Matter (WDM) is how in the early Universe it will be non-relativistic, or slower than other candidate particles, remaining trapped in small overdensities which form dark matter subhaloes. Other dark matter particles instead are faster and relativistic, escaping these overdensities which result in on average, a higher minimum mass for subhaloes. These subhaloes are then what undergo the hierarchical clustering to eventually form galaxies (Berezinsky et al., 2003; Diemand et al., 2005). Particles masses allowed by CDM span a range of magnitudes as low as 10^3 eV, though can reach masses above 10^{11} eV. This is on the heavier end of dark matter particle candidates hence the classification of Weakly Interacting Massive Particles (WIMPs) (Steigman & Turner, 1985; Queiroz, 2017). On larger scales, CDM works the best compared to other models in recreating the large scale Universe in simulations based off of our current observations (Moore et al., 1999). Due to how CDM forms lower mass subhaloes than other models in the early Universe, we would then expect a large abundance of them even in the present day (Fiacconi et al., 2016). These abundances are shown in Figure 1.2, where it increases as subhalo mass decreases. While we do detect satellites with masses in line with predictions from CDM, we have not found an abundance of them quite as high as expected. This missing satellites problem, and how this can be solved, are one of the biggest challenges to the CDM paradigm (Kauffmann et al., 1993; Klypin et al., 1999).

There are a few solutions to this, and it is generally split into two ideas. One is that many of these subhaloes that would be in the Milky Way are simply too small to host stellar populations. This was backed by the observations of ultra-faint satellites in 2007 from the Keck Observatory, which saw dwarf galaxies with stars making up for in some cases, under a thousandth of their mass Simon & Geha (2007). While a threshold was not established for how heavy a dark matter subhalo needed to be to host stars, the possibility was clear that there could exist some hosting even less stars or potentially none that obviously would make direct observations almost impossible. This would not completely solve all the pitfalls of CDM however, with another notable issue being the cusp core problem which sees observed density profiles of haloes being much more flat, or cores, at small radii compared to simulations which feature very steep and dense cusps instead (Flores & Primack, 1994; Moore, 1994; Moore et al., 1999; de Blok et al., 2001; Oh et al., 2011, 2015). The second idea is focused on alternatives to CDM, usually in the form of different particles that define dark matter instead of WIMPS. These could give rise to different subhalo abundances, along with density profiles that more closely match cores, and the main alternative models are explored below:

1.1.3 Alternate dark matter particles

Solutions relating to these pitfalls of CDM usually relate to revisions to the dark matter particle, either in its properties or behaviour (Spergel & Steinhardt, 2000). There is a wide range of alternative dark matter models that have been worked on so far to either be applied alongside, or in place of CDM. We outline the process of substructure formation below, with a brief overview of the main dark alternative dark matter candidates below, along with their main differences to CDM.

Warm Dark Matter

Warm dark matter (WDM) is an alternative dark matter model where the dark matter particle mass is significantly lighter than in CDM. In order to understand how this affects structure formation and the predictions of WDM, we must first further explore the process by which substructure formed in the early Universe, prior to galaxy formation by hierarchical clustering. The very early development of the Universe is generally split into two main eras, being the radiation dominated phase, followed by a transition into the matter

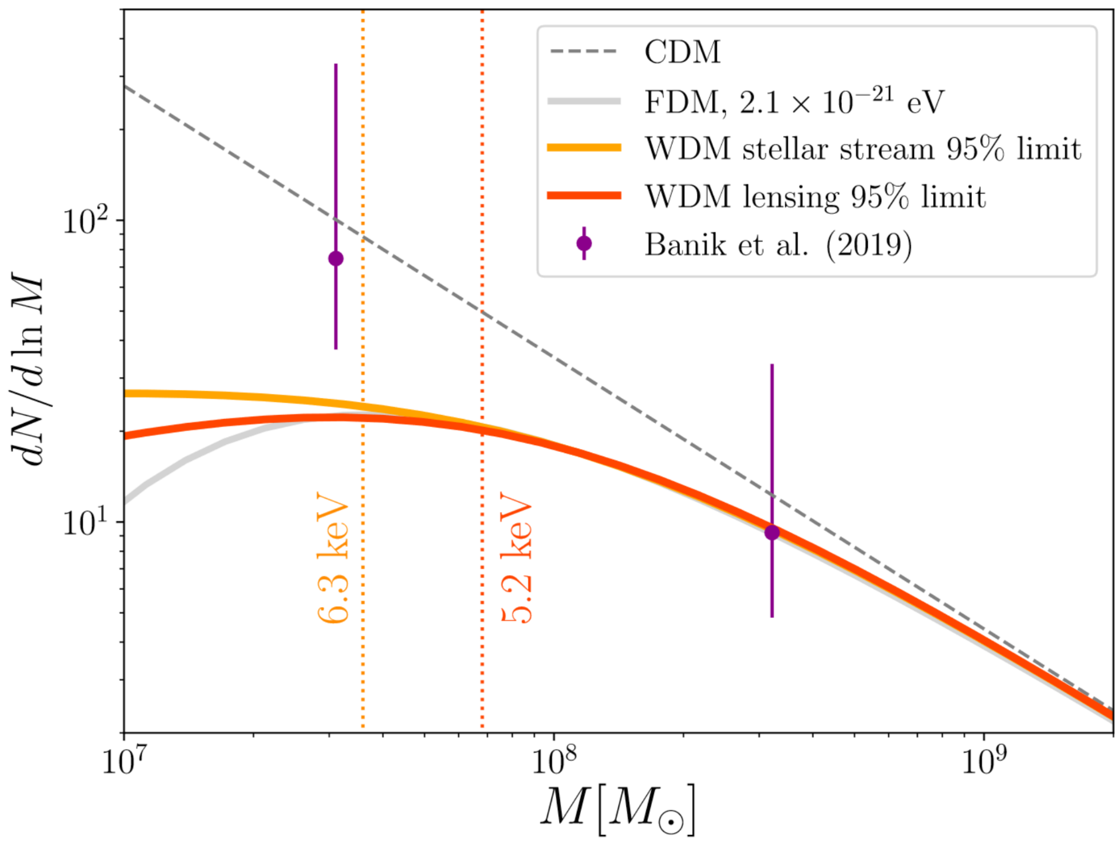

Figure 1.2: Normalised subhalo mass functions comparing the relative abundance between CDM, WDM and FDM. A standard CDM model is shown in the grey dotted line with and has no minimum mass limit, unlike the other models. For WDM, 2 lines are shown denoted by the method used to constrain the potential WDM particle, with these methods described in Section 1.4. The orange line for a 5.2 keV particle is the constraint using gravitation lensing in Gilman et al. (2020), while the yellow line for a 6.3 keV particle is constrained using stellar streams from Banik et al. (2021a). The vertical dotted lines of these respective colours additionally represent the minimum mass for a subhalo. FDM is then also shown for a candidate described in Schutz (2020) for the solid light gray line. While no vertical line is shown denoting a hard minimum mass limit, it roughly will be in line with the limits of WDM here. Figure taken from (Schutz, 2020)

dominated phase (Kawasaki et al., 2000; Hannestad, 2004). Particularly in the radiation dominated phase, the Universe will remain very smooth and homogeneous. Additionally, during this time, small scale fluctuations can develop slowly, and as the Universe transitions to being matter dominated, a steep reduction in the Jean's length causes them to grow rapidly and eventually collapse due to gravitational instability. This process leads dark matter clumps forming, which ultimately seed galaxy formation as mentioned above (Berezinsky et al., 2003; Diemand et al., 2005).

Warm dark matter models (WDM) are constructed of particles between 10^{-5} and 10^3 eV, with the heavier end here being the most similar to CDM (Bode et al., 2001a; Lovell et al., 2012). On larger scales, WDM manages to maintain a similar evolution to CDM. These warmer particles allow for smoother structure as thermal motion in the early Universe erases small scale substructure, as seen in Figure 1.1. Another very clear difference to CDM in the figure is the significantly reduced abundance of the small scale haloes present, instead being smoothed out with their mass contained within the filaments. Generally, subhalo masses under a WDM paradigm tend to be restricted to around $10^8\,\mathrm{M}_\odot$ as shown in Figure 1.2 (Lovell et al., 2014)

The key difference with WDM here is that these lighter particles remain relativistic far longer than CDM particles during the rapid expansion in the radiation dominated phase. They retain a significant enough thermal velocity which gives rise to a high free-streaming length, defined by λ_{fs}, especially compared to CDM. This is an important parameter in the context of the dark matter particle and the early Universe, and the equation for this is below and also discussed in Schneider et al. (2012):

$$\lambda_{\mathrm{fs}} = \int_0^{t_{\mathrm{EQ}}} \frac{v(t)dt}{a(t)} \approx \int_0^{t_{\mathrm{NR}}} \frac{cdt}{a(t)} + \int_{t_{\mathrm{NR}}}^{t_{\mathrm{EQ}}} \frac{v(t)dt}{a(t)} \tag{1.1}$$

Here, t_{EQ} is the is the time at which the Universe achieves matter-radiation equality, during the transition from being radiation dominated to matter dominated. t_{NR} meanwhile represents the time at which the dark matter particles become non-relativistic, with v and a being the velocity of the dark matter particle and scale factor describing the expansion of the Universe. At times before t_{NR} where the particles are relativistic, their velocity is simply equal to the speed of light hence the substitution of c in that integral.

This parameter can be looked at as what governs the maximum size of perturbations that would be effectively washed out and hence, would never collapse and form a clump. While this is somewhat simplified such as assuming free-streaming ends after the matter-radiation equality, it provides a good means of comparison of dark matter particles (Bond & Szalay, 1983a). Based off of the equation, particles that remain relativistic the longest will tend to have a higher free-streaming length, due to the higher weighting they would give to the first term of the equation which uses c for the velocity. Additionally, the slower particles such as from CDM would both be relativistic for less time, and have a lower velocity afterwards resulting in far smaller free-streaming lengths. This demonstrates well how the properties of the dark matter particle can govern the early formation of dark matter clumps, leading to different dark matter substructure today as shown by the minimum masses in Figure 1.2.

Fuzzy Dark Matter

Fuzzy dark matter (FDM), also described as quantum or ultralight dark matter is constructed of particles far lower in mass than WDM, being of the order 10^{-22} eV (Hu et al., 2000; Mocz et al., 2019). These particles have a more wave-like behaviour, and exhibit quantum effects unlike their heavier counterparts. This wave-like nature causes it to be generally more smooth at larger scales, like WDM. At smaller scales, their de Broglie wavelength, of order a few kpc due to the low particle mass, causes an interference pattern which give to small scale density perturbations for subhaloes to form (Burkert, 2020). FDM in the early Universe has its own way of suppressing low mass subhaloes forming instead of free-streaming. Instead, quantum pressure is exerted on collapsing overdensities, and should these overdensities not be sufficiently massive and dense, this pressure will overcome it and suppress subhaloes of low masses forming. This mechanism prevents many subhaloes existing of masses less than around $10^7\,\mathrm{M}_\odot$ to $10^8\,\mathrm{M}_\odot$, generally just below the the mass at which we believe dwarf galaxies can form stars (Marsh & Silk, 2014; Du et al., 2017; Schutz, 2020). In addition, this interference and quantum pressure mean that haloes have a far flatter density profile relative to WDM or CDM (Bar-Or et al., 2019).

Self Interacting Dark Matter (SIDM)

Self interacting models started out as an expansion of CDM to better fit observation pitfalls from Spergel & Steinhardt (2000). Today, the idea of self interacted models are not tied to any specific particle mass necessarily, but instead the idea that dark matter particles can interact with one another under specific conditions. The most important result that would result from self interacting models, which typically most particle candidates still are not good at solving is the cusp core problem. The extremely high densities present at very small radii of haloes and subhaloes would be the conditions that allow for interactions between dark matter particles, and the energy and resulting outwards pressure from these force a flatter density profile into more of a core instead of a cusp (Weinberg et al., 2015; Tulin & Yu, 2018; Outmezguine et al., 2023). This gives them a good advantage in that they can maintain CDM like structure at larger scales, and cores at smaller scales. Self interacting WDM models take a slightly different approach, and instead the impact of self interactions are explored in the early Universe. Here, these self interactions can suppress free-streaming instead which can allow lower mass subhaloes to still form. This would allow for even particularly hot models of dark matter, which usually under-predict the number of substructure, to better fit observations (Raffelt & Silk, 1987; Hannestad & Scherrer, 2000).

Alternate models to dark matter

In addition to invoking dark matter to explain phenomena such as the rotation of galaxy clusters or the flat rotation curve, there have been proposed solutions that instead modify how gravity works. The theory of MOdified Newtonian Dynamics (MOND) for example can either heavily suppress the previously thought impact of dark matter, or completely remove the need for it (Milgrom, 1983; Sanders & McGaugh, 2002). Without these high abundances of low mass subhaloes, there would be no issues of missing satellites, and instead a large number of satellites form as tidal dwarf galaxies from previous interactions between galaxies, generally giving much lower predictions for the number in satellites in our galaxy compared to CDM (Bournaud et al., 2007; Gentile et al., 2007). Without the existence of dark matter subhaloes with this theory, using stellar streams to probe for them could be an important result for the evolution of MOND. Discovery of a stream, or any object with no clear visible baryonic perturber would further cement dark matter as the most likely theory versus the current understanding of MOND.

1.2 An overview of MW structure

The MW is a barred spiral galaxy, named after the massive visible structures on its disk of a galactic bar and spiral structure, as in Figure 1.3. Excluding objects such as dwarf galaxies which are usually satellites to larger host galaxies, these spiral galaxies are the most common in the Universe and feature large amounts of ongoing star formation even today (Lintott et al., 2011a). Such description follows the classifications first used by Hubble who first observed these structures on some external galaxies, leading to the classification system widely used today (Hubble, 1922, 1926). The key structures of the MW reside in a relatively flat galactic disk (Struck, 2015). In addition to this disk, a more vertically expanding component lies in the centre of the MW in the form of the bulge (Gonzalez et al., 2012). Most of the MW mass however, is distributed instead in a roughly spherical shape mostly owing to the encompassing triaxial dark matter halo, which is significanly more spherical than the disk (Newberg & Yanny, 2006; Hayashi & Navarro, 2006; Prada et al., 2019).

With how galaxies form through hierarchical clustering, which ultimately formed this dark matter halo, we naturally expect there to exist plenty of structures present throughout the MW and other galaxies, remaining in the halo as satellites and remnants of hierarchical clustering. The Large Magellanic Cloud is one example and the largest dwarf galaxy satellite in the MW, massive enough object to distort the halo of the MW and also affect baryonic structures throughout it (Springel et al., 2006; Law et al., 2009; Erkal et al., 2019; Vasiliev & Belokurov, 2020; Vasiliev et al., 2020; Petersen & Peñarrubia, 2021; Lilleengen et al., 2023). Galaxies like the MW also host a plethora of far smaller structures. There are the aforementioned stellar streams which I discuss further in Section 1.3. We also observe Globular Clusters (GCs), star clusters with masses up to millions of solar masses completely devoid of dark matter. Finally, as suggested above by the CDM paradigm, we also expect the MW to host subhaloes, which in contrast to GCs would be similar mass objects made entirely of dark matter with no stellar population (White & Rees, 1978; Davis et al., 1985; White & Frenk, 1991).

1.2.1 The disk

The disk houses the bulk of all stars, gas and dust within galaxies, hence, making up for the majority of their baryonic mass (Tayler, 1993). As mentioned above, stars in the disk follow a flat rotation curve, which for the MW these stars reach circular velocities of $\sim 240\,\mathrm{km\,s^{-1}}$ (Sofue, 2013). As is the case with the MW, disks can also contain two relatively massive structures which classify the galaxy itself, the Galactic Bar and Spiral Structure.

Galactic bars and most spiral structure propagates through the disk as a density wave, effectively travelling through a medium of stars and gas in a circular motion about the galactic centre. Their formation is believed to be linked to induced gravitational instabilities in the disk, though the exact source of these is still up to debate. They are then maintained by rotation of the disk which continuously drives these density waves over large timescales (Sellwood et al., 2019). This gives them a behaviour more as a rigid body, and are typically simulated as such. This allows them to rotate faster than limitations imposed by the flat rotation curve seen in stars in the MW disk (Debattista & Sellwood, 1998). This mechanism is what gives rise to such high densities of stars that make up these structures, and result in high asymmetries of the potential through the galactic disk. This in turn can apply various perturbations to stars both within the disk and beyond (de Vaucouleurs, 1958; Dehnen, 2000).

The Galactic Bar

The bar is an especially dense and more massive structure of the disk, particularly when compared to spiral structure. In the case of the MW, the bar additionally dominates most of the bulge mass as well, expanding more vertically than the disk Binney et al. (1997); Gonzalez et al. (2012). The MW bar has a mass of the order $10^{10}\,\mathrm{M}_\odot$ contained within a length, or semi-major axis of simply a few kpc (Portail et al., 2017b,a; Li et al., 2022). These lie in the centres of such galaxies and rotate much faster than spiral structure (Eskridge et al., 2000; Marinova & Jogee, 2007). Specifically for the MW bar, this $10^{10}\,\mathrm{M}_\odot$ object rotates at a pattern speed of $\Omega = 41 \pm 3\,\mathrm{km\,s^{-1}\,kpc^{-1}}$, which corresponds to a rotation every $\sim 150\,\mathrm{Myr}$ (Portail et al., 2017a; Bovy et al., 2019; Sanders et al., 2019). Passages of the the longer side of the bar will apply significantly higher gravitational forces than when perpendicular to it at its semi-minor axis, and considering how quickly a bar rotates compares to the orbital periods of stars it can have large effects on the orbits of individual stars and larger nearby structures. This makes the bar an excellent structure to study through simulations to better understand the evolving forces throughout the MW. Conversely, understanding the perturbations the bar applies to well observed regions can in turn help better constrain its properties such as using the velocity space of the local neighbourhood, where our position in the MW could position us near a resonance between the epicyclic frequency of stars and the rotation of the bar. While the bar itself is difficult to observe through the dust and stars in the disk, this is one such method we can constrain properties such as its length and pattern speed based off of where these resonances occur (Dehnen & Binney, 1998b; Dehnen, 1999, 2000).

Spiral structure

Spiral arms are the defining structures of over half of the galaxies in the Universe (Lintott et al., 2011b). They contain higher densities of stars than the rest of the disk, and rotate about the galactic centre as trailing arms, where the end of the spiral points away from the direction of rotation (de Vaucouleurs, 1958). The density wave like nature of most spirals is especially important here, as the flat rotation curve would otherwise mean they would rapidly wind up over time due to the longer orbital periods for stars at higher radius. This would give spiral arms a lifetime of only a few orbits before they become indistinguishable from the background in the disk. Instead, this quasi-stationary nature of spiral arms allows them to maintain this consistent shape for (Lin & Shu, 1964; Minchev, 2016). Similar to the bar, this makes them good candidates for studying perturbations to structures due to the gravitational effects of a passage of a large rigid body such as a spiral arm. Their longevity arising from the density wave nature also allows for a relatively simple potential in the context of simulations, so are often simulated with no time dependence (Cox & Gómez, 2002; Monari et al., 2016; Banik & Bovy, 2019).

Spiral arms come in two main flavours which define their relative size and density relative to the disk. Spirals which are larger and very dense relative to the disk, continuous throughout and small in number are referred to as grand design. Conversely, spirals which are numerous and smaller are referred to as flocculent, which give rise to a more scattered and patchy potential across the disk. These do not follow the density wave nature as strictly, and are

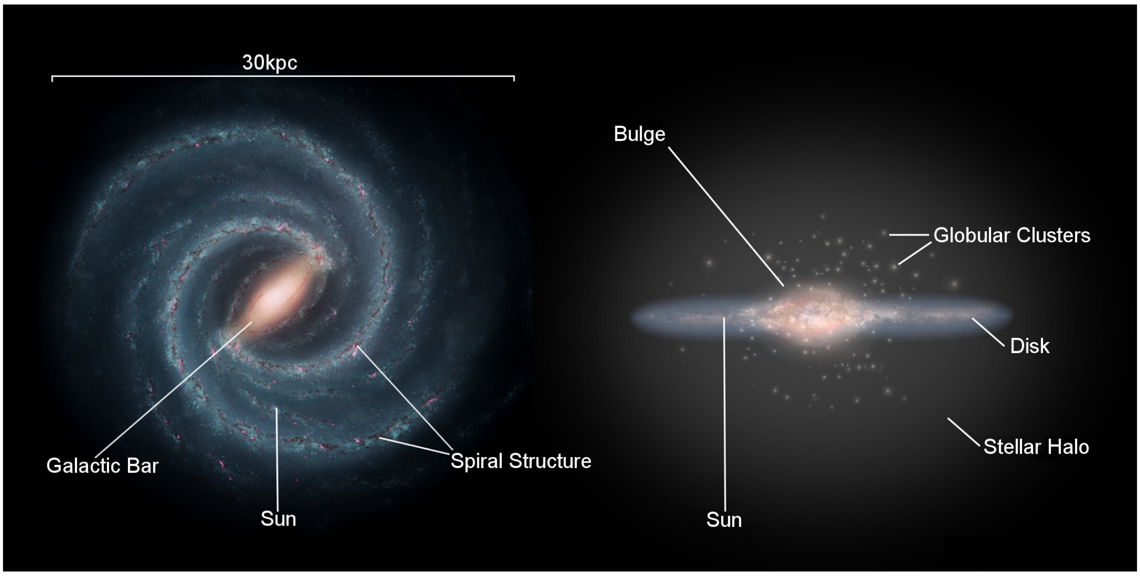

Figure 1.3: A simple representation of a Milky Way-like barred spiral galaxy and its key features, shown as a face-on (left) and edge-on (right) profile to highlight both the key structures in the disk and stellar halo. The scale of the dark matter halo far exceeds the scale in the figure and is excluded, though would envelop the entire galaxy. Image adapted from ESA, *Anatomy of the Milky Way* (2016)

often fairly short lived with new spirals quickly forming again from small scale gravitational instabilities. Generally, galaxies which contain a galactic bar are more likely to have grand design spiral structure (Elmegreen et al., 2003). The MW is believed to more dominated by a grand design spiral structure, consisting of the Perseus the Scutum-Centaurus arm. Their higher relative density and lower numbers compared to flocculent spirals would impose higher disk asymmetries, and also result in larger perturbations to structures in the MW (Lindblad, 1959; Elmegreen & Elmegreen, 1995; Bittner et al., 2020). The outer MW however shows a transition to more flocculent spirals, with observations near the end of the Perseus arm showing other short, low density structures hinting at flocculent spirals (Quillen, 2002).

1.2.2 The halo and its satellites

Encompassing the entirety of the galactic disk exists a roughly spherical population of stars in what we call a stellar halo. This consists of some of the oldest and most metal poor stars in galaxies in very low densities compared to the disk. While the mean background of stars and gas is very diffuse in the halo, as explained in Section 1.1.1 the abundance of satellites throughout the halo, ranging in size from GCs to massive dwarf galaxies lead to this idea of galaxies forming through merging of haloes alongside their stellar populations (Helmi, 2008). As a result, dwarf galaxies make for the most common type of galaxy found in the Universe (McConnachie, 2012). All structures in the halo have motion in all 3 dimensions, and unlike those outlined in section 1.2.1, are not confined to motion in the disk only (Gilmore et al., 1989; Majewski, 1993; Bland-Hawthorn & Freeman, 2000; Freeman & Bland-Hawthorn, 2002).

Today, we have observed more than 50 dwarf galaxies and 150 GCs (Harris, 2010; McConnachie, 2012; Simon, 2019), and we now know the MW is not unique in having very high populations of these satellites from observations of other galaxies such as M31, the Andromeda galaxy (Martin et al., 2006; Collins et al., 2011; Kalirai et al., 2010). As one would expect with how galaxies form, we now know that galaxies with higher luminosities and baryonic mass tend to also host larger populations of dwarf galaxies and GCs (Harris et al., 2013). Below, we also cover 2 of the largest of the structures in the halo, each of which have revealed much on both the formation of our own galaxy along with how smaller structures evolve in their presence.

The Sagittarius dwarf galaxy and stream

Sagittarius is a dwarf galaxy of particular interest due to how it is currently infalling into the MW, and was the first dwarf discovered to be tidally disrupting in the Milky Way (Ibata et al., 1994). This merger event in turn, lead to a better understanding of the origins of other structures in the MW as well. The appearance of Sagittarius as it is tidally disrupted in the MW is similar to how some stellar streams look, which appear as long trails of stars following roughly the same orbit (Majewski, 2003; Majewski et al., 2003). The stream aspect of Sagittarius primarily came from discoveries of metal poor carbon stars in the halo, which formed this stream like shape while having very similar metallicities to Sagittarius. It was found that these likely belonged to Sagittarius long ago, and that the process of Sagittarius merging into the MW has begun to tear it apart and strip its stars into the massive Sagittarius stream we see today (Totten & Irwin, 1998; Mauron et al., 2004, 2005, 2007; Lagadec et al., 2010). I will discuss streams further in Section 1.3.

With a mass of order up to $6 \times 10^{10}\,\mathrm{M}_\odot$ (Gibbons et al., 2017), compared to a Milky Way halo mass of $5.40 \times 10^{11}\,\mathrm{M}_\odot$ enclosed within 50 kpc (Wilkinson & Evans, 1999), the abundance of data of Sagittarius alone have allowed us to uncover so much information on galaxies. With further observations, it only bolstered the idea of how galaxies formed as we were able to associate several GCs as belonging to Sagittarius as well, instead of belonging to the MW (Irwin, 1999; Bellazzini et al., 2003; Carraro et al., 2007; Massari et al., 2019).

The Large Magellanic Cloud

Another one of the most impactful dwarf galaxies to the MW, the Large Magellanic Cloud (LMC) is especially massive, more so than Sagittarius and has been shown to give detectable effects to the MW, including a significant reflex motion that has dislodged the MW disk from the Galaxy centre of mass (Petersen & Peñarrubia, 2021; Erkal et al., 2021). Furthermore, the orbit of the LMC could be traced due to the overdensities in the stellar halo it leaves in its wake (Conroy et al., 2021). With a mass of $1.38 \times 10^{11}\,\mathrm{M}_\odot$ and orbital distance of $\sim$ 50kpc, the LMC is capable of applying significant perturbations to a great deal of the galaxy's structure, especially those further out in the halo which would receive less influence from the MW disk such as large numbers of stellar streams (Scowcroft et al., 2016; Pietrzyński et al., 2019; Erkal et al., 2019). The LMC's orbital plane is also aligned with the flattening of the Milky Way's halo, hinting at how it may be capable of

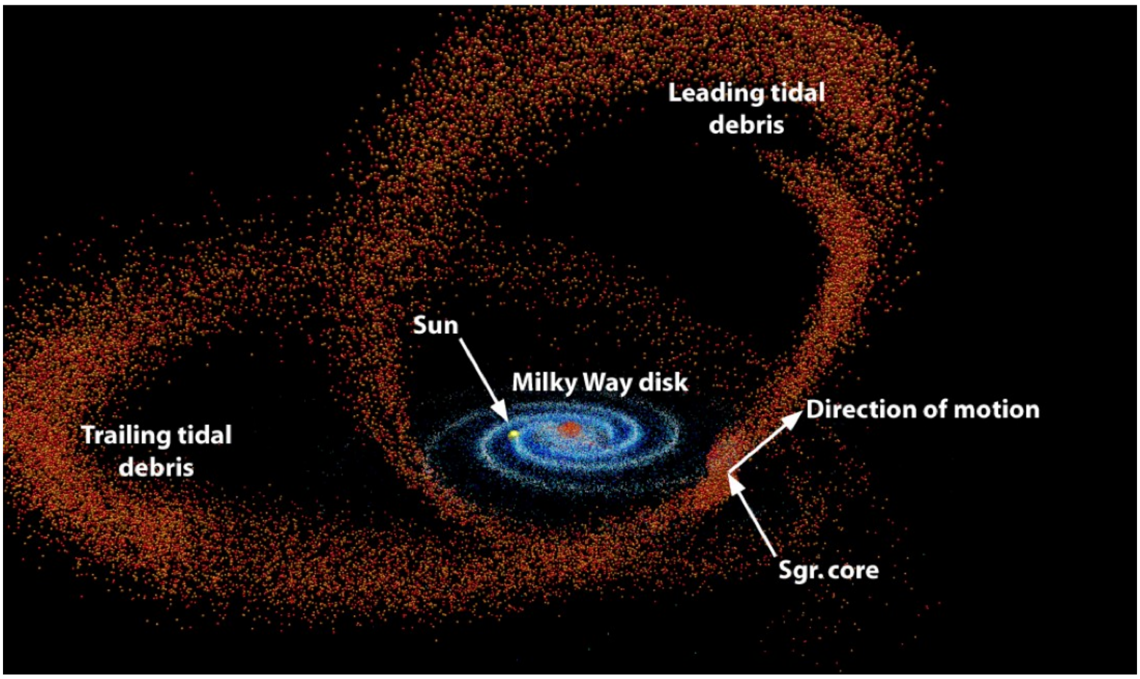

Figure 1.4: A diagram of the Sagittarius stream around the Milky Way disk. Here, spiral structure can be seen in the plane of the disk, meanwhile the stellar stream shows fully 3-dimensional motion orbiting about the galactic centre. Around the core, or progenitor, the consequence of tidal stripping and the resulting motions of the stars can clearly be seen by the different radii of the leading and trailing sections. Stars that were stripped at smaller radii than the progenitor would have lost energy and angular momentum, causing their orbits to shift and follow a shorter radius and period than the progenitor. The opposite holds for stars at higher radii here, needing to take on more distant orbits with longer periods and trailing behind. Image from David R. Law, (Law & Majewski, 2010a,b)

stretching out the the MW halo due to the immense gravitational forces it exerts on its host galaxy (Erkal et al., 2019; Vasiliev et al., 2020).

1.3 Stellar streams

The first observations of stellar streams started from 1974, however, in these cases without knowledge of their dynamical nature (Mathewson et al., 1974; Majewski et al., 1996a). It was only until 1996 where conclusive evidence was obtained and a group of approximately 20 stars was observed in the halo all sharing roughly the same motion (Majewski et al., 1996b). This further added to the idea of galaxies forming through hierarchical clustering as we began to uncover how streams themselves formed through the disruption of smaller GCs or even dwarf galaxies in the case of larger streams such as Sagittarius covered above (Ibata et al., 1994; Newberg & Carlin, 2016)

1.3.1 Observations of streams

The detection of stellar streams has evolved over time as new instruments allowed for improved approaches to finding stellar streams, which were previously somewhat difficult to detect due to their often large distances from the galactic centre and ourselves. Detection of streams often started with Wide-field photometric surveys, as they quickly covered a large portion of the sky such as the Sloan Digital Sky Survey (SDSS) (York et al., 2000). Even with simply positions, densities and the distance modulus of stars in a region of the sky, streams can relatively easily stand out as a slight stellar overdensity. Particularly if these stars form a trail with similar distance moduli, it means what is being observed is most likely a stellar stream. This is evident in Figure 1.5 with an observation of the stream of the Sagittarius dwarf by Belokurov et al. (2006) using SDSS Data Release 5, though earlier data releases of this same survey had previously been used to additionally discover the Sagittarius stream in the first place (Yanny et al., 2000; Ibata et al., 2001). Here, there is a clear higher density of stars with a gradient in their distance modulus, shown by the stars along the stream getting more blue, hence closer, as we go to lower values in right ascension. This particular example shows further structure such as a bifurcation or split along the stream, with two tails visible at declination of around 30 deg and 20 deg. Since then, many other streams were detected in SDSS, of particular interest being thin streams where we would be able to see faint perturbations and overdensities such as the GD-1 and Palomar 5 stream (Odenkirchen et al., 2001a, 2003; Grillmair & Dionatos, 2006a; Ibata et al., 2017). These streams make for excellent candidates to study the smaller scale forces affecting objects in the halo and can be used to better map out the forces and matter throughout the MW halo (Koposov et al., 2010).

With discoveries of many stellar streams using SDSS, various photometric surveys have continued to try and map out all streams in the MW and use these to better understand the ongoing forces and history of the MW in general. Limitations imposed on SDSS, owing to weather patterns and artefacts meant lower surface brightness streams especially would be very hard to detect (Finkbeiner et al., 2016). Still, newer surveys continue to detect streams, including the ATLAS survey (Shanks et al., 2013) with detection of the ATLAS stream (Koposov et al., 2014), Pan-STARRS1 3π (Juric, 2012; Slater et al., 2013, 2014) with PS1 streams (Bernard et al., 2016) and the Dark Energy Survey (DES) (The Dark Energy Survey Collaboration, 2005; Dark Energy Survey Collaboration et al., 2016) with a handful of streams including Elqui and Aliqa-Uma (Shipp et al., 2018). On top of simply detection, these surveys can aid in deciphering their progenitors. Isochrones can be fit to the Colour Magnitude Diagram (CMD) of the stream's observed stars. Specifically, this can be done to the match the Red Giant Branch (RGB) and main sequence stars of the stream's member stars, and the age and metallicity used to generate this isochrone can therefore give estimates on these properties for the stream. Combined with the width of these streams, quite often we are able to see potential progenitor candidates from photometric surveys, with the general rule being thicker streams originating from higher mass progenitors (Johnston et al., 2001; Bonaca et al., 2012). Additionally, estimates of the dispersion in metallicities can reveal the type of progenitor, with a higher dispersion owing to a dwarf galaxy progenitor due to the star formation occuring over time. In contrast, GC stars would have only one burst of star formation, and hence, would have little metallicity dispersion (Willman & Strader, 2012; Leaman, 2012).

While streams can be identified relatively easily using photometric surveys such as SDSS, there lie some cases where they require using kinematic detection from spectroscopic surveys on stars such as, M-giants and turnoff stars (Vivas et al., 2001; Duffau et al., 2006; Carlin et al., 2012; Majewski et al., 2012; Sheffield et al., 2012). Furthermore, these surveys can lead to information such as the velocity dispersion which can provide further aid in the progenitor origins of stellar streams. A good example of this is Pisces stream by Martin et al. (2013), where the kinematically cold nature in the dispersion of this thin stream further verified a globular cluster origin or ultra-faint dwarf, in accordance to findings from photometric surveys by (Bonaca et al., 2012). The potential of these surveys expands further into determining the orbit of streams too. The Orphan-Chenab (OC) has had long studied velocities since its discovery, being a stream with no clear progenitor (Grillmair, 2006; Belokurov et al., 2006, 2007). The difficult determination using these velocities lead to estimations of its orbit to often conflict with one another such as the early work that followed in Fellhauer et al. (2007) and Jin & Lynden-Bell (2007), which lead to different candidate progenitors. Later on, use of SEGUE spectroscopy and imaging data allowed for a more confident fit to the OC stream by (Newberg et al., 2010).

More recently, there have been significant improvements to the approach of detecting stellar streams. The vast assortment of data now available from surveys such as *Gaia*, in particular its second data release has dramatically increased the number of streams we are both aware of and can model (Gaia Collaboration et al., 2018a,b). In combination with this vast array of data available, the STREAMFINDER algorithm, developed by Malhan & Ibata (2018) allowed for automatic detections of streams 2D positional and kinematic data using the errors that the second Gaia data release delivered. Shortly following this, the extensive proper motion data of Gaia lead to a quick discovery and verification of 5 streams in Malhan et al. (2018). This could expand how streams are detected moving forward, with only minor adjustments needing to be made for different surveys/availability of data. As demonstrated moving forward in Ibata et al. (2019), additional streams were discovered after refinements to the algorithm. Gaia has also been used alongside other data releases, including the Dark Energy Survey (DES) to obtain accurate proper motion measurements verify an additional 9 streams (Shipp et al., 2019). To date, we have detected 95 streams, and this number is no doubt likely to rise in timespans of less than a year. A full catalogue of these stellar streams, alongside their dynamical information including 6D stream track information for some, is available in Mateu (2023) alongside their publicly available Python library GALSTREAMS.

1.3.2 The tidal radius

Before exploring stellar stream formation, we first discuss the tidal radius and how it can be derived. The tidal radius is where the inner and outer Lagrange points of a stream progenitor are. As a result, is defines the points of a progenitor where stars are stripped and gradually form the leading and trailing arms of a stream. Its value can be determined using a simple circular orbit with reference to Figure 1.6. A more detailed look into the concept of tidal radius for clusters on elliptical orbits is outlined in von Hoerner (1957) and King (1962).

First, we take the progenitor on its orbit at radius r, orbiting with angular velocity $\Omega = v/r$. Given the circular orbit, its kinetic energy is equal to -1/2 of its potential

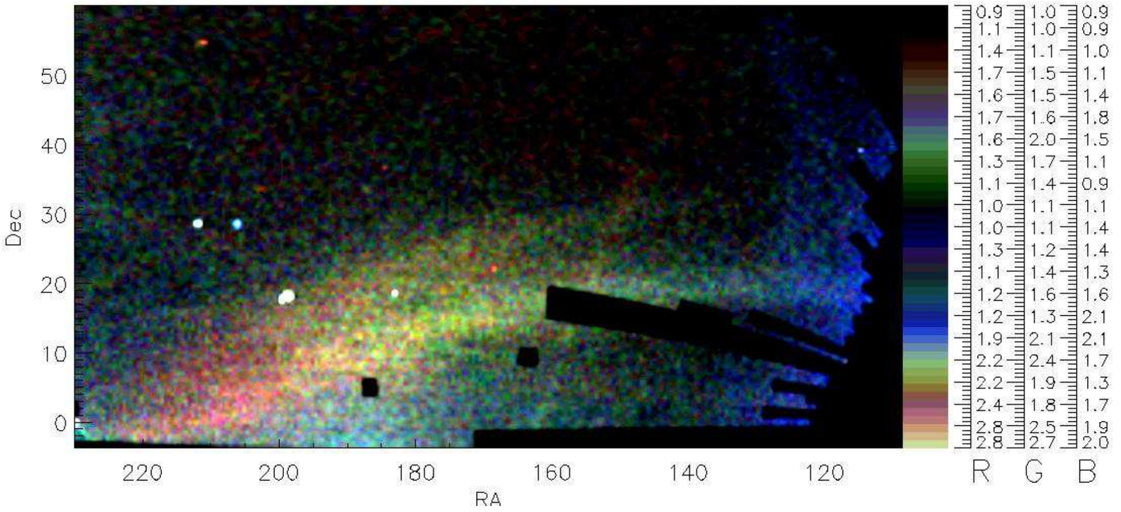

Figure 1.5: An RGB composite plot from the Sloan Digital Sky Survey (SDSS) Data Release 5, demonstrating the imaging and initial detections of a stellar stream across galactic ascension and declination coordinates. An RGB image is constructed here by combining 3 grayscales images, each representing one of these 3 colours and a distance bin in the observed stars. Specifically for this, blue signifies the image of the closest stars in r-mag with $20 < r \leq 20.66$, followed by green for $20.66 < r \leq 21.33$ and red for the furthest at $21.33 < r \leq 22$. The weighting towards one of these 3 colours is therefore determined by the stellar densities of the distance bins relative to eachother, and a palette of 50 different colours is shown, with the 3 respective stellar densities that would result in it on the right. The densities here are in units of 100 stars per square degree. Image used from Belokurov et al. (2006)

energy at all times, or:

$$\frac{1}{2}\mathrm{m}\mathrm{v}^2 = \left(\frac{-1}{2}\right)\left(\frac{-\mathrm{GMm}}{\mathrm{r}}\right) \tag{1.2}$$

Which simplifies to:

$$\mathrm{m}\mathrm{v}^2 = \frac{\mathrm{GMm}}{\mathrm{r}} \tag{1.3}$$

Here, m denotes the progenitor mass compared to the MW mass M. Simplifying this and dividing m out to get accelerations lets us equate the centripetal acceleration to the gravitational acceleration. Note that since this is negative of the potential energy, the derivative of the potential will be positive here:

$$\frac{\mathrm{v}^2}{\mathrm{r}} = \frac{\mathrm{GM}}{\mathrm{r}^2} = \frac{\mathrm{d}\phi}{\mathrm{dr}} \tag{1.4}$$

And given $\Omega = \mathrm{v}/\mathrm{r}$:

$$\Omega^2\mathrm{r} = \frac{\mathrm{d}\phi}{\mathrm{dr}} \tag{1.5}$$

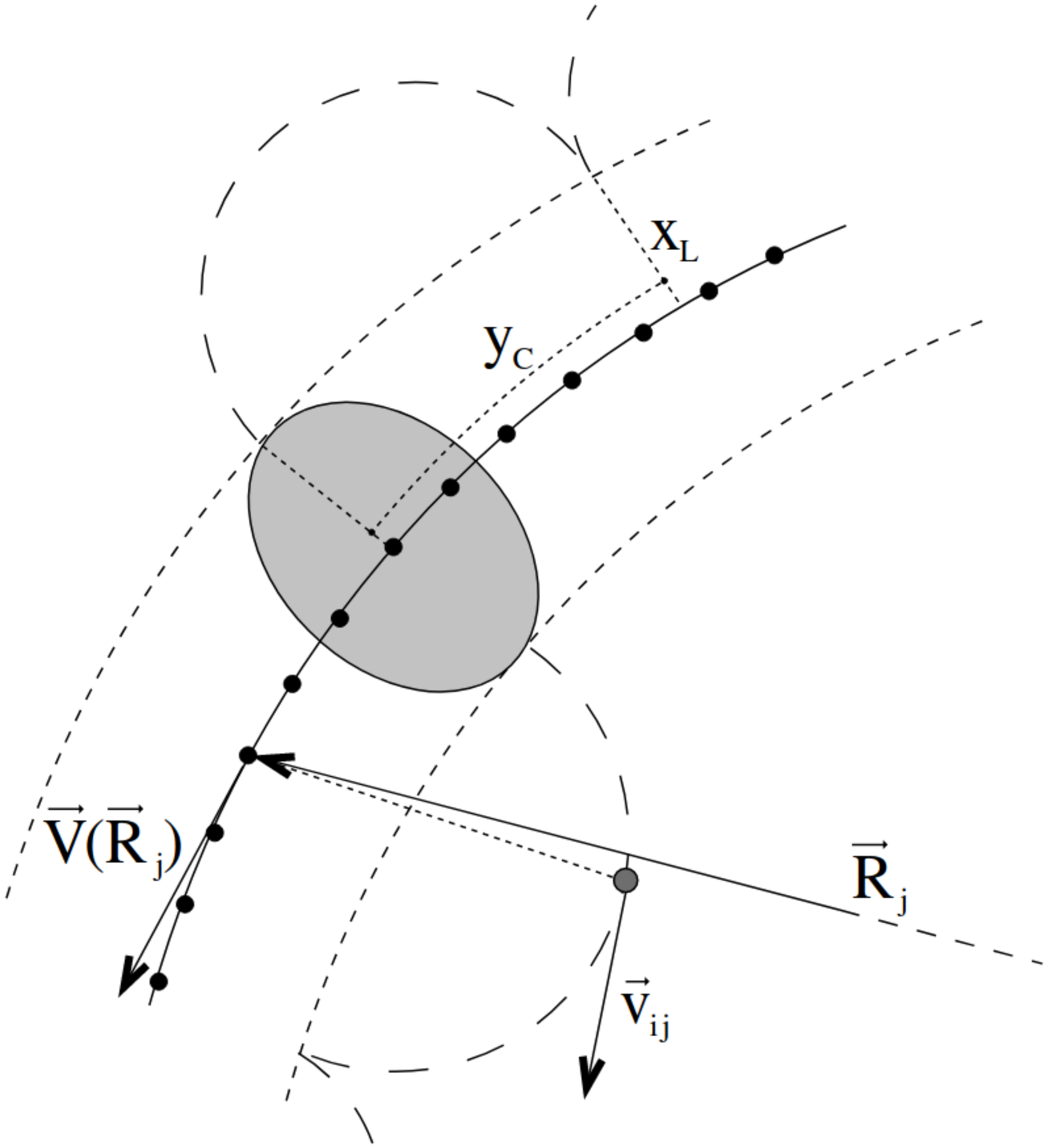

Figure 1.6: A typical schematic of stream formation as stars are stripped from the Lagrange points. Here, the gray ellipse is the progenitor cluster, which extends to its inner and outer Lagrange points at a tidal radius defined by $\mathrm{x_L}$. The orbit of this cluster is shown by the solid black curve with black points along it showing equidistant points. Each of these points has their own corresponding radius and velocity $\tilde{\mathrm{V}}$ and $\tilde{\mathrm{R}}$. A Tidally stripped star meanwhile is represented by the small gray circle, moving in an epicyclic motion with velocity $\tilde{\mathrm{v}}$, with the distance between each epicyclic loop denoted by $\mathrm{y_c}$. Image used from Küpper et al. (2010).

Now, we take a particle further out at radius $\mathrm{r} + \mathrm{r_t}$ which is at the Lagrange point. We use this new radius in Equation 1.5, bearing in mind that due to the Lagrange point, the angular velocity must be the same as the progenitor. Furthermore, we must also account for the additional gravitational acceleration the particle receives from the progenitor itself:

$$\Omega^2(\mathrm{r} + \mathrm{r_t}) = \frac{\mathrm{d}\phi(\mathrm{r} + \mathrm{r_t})}{\mathrm{dr}} + \frac{\mathrm{Gm}}{\mathrm{r_t^2}} \tag{1.6}$$

First we expand out the brackets on the left. Additionally, the small change in r for the potential can be approximated to:

$$\Omega^2\mathrm{r} + \Omega^2\mathrm{r_t} = \frac{\mathrm{d}\phi}{\mathrm{dr}} + \mathrm{r_t}\frac{\mathrm{d}^2\phi}{\mathrm{dr}^2} + \frac{\mathrm{Gm}}{\mathrm{r_t^2}} \tag{1.7}$$

Now, by removing the original identity from Equation 1.5:

$$\Omega^2\mathrm{r_t} = \mathrm{r_t}\frac{\mathrm{d}^2\phi}{\mathrm{dr}^2} + \frac{\mathrm{Gm}}{\mathrm{r_t^2}} \tag{1.8}$$

This equation allows us to isolate the tidal radius $\mathrm{r} + \mathrm{r_t}$

$$\frac{\mathrm{Gm}}{\mathrm{r_t^2}} = \Omega^2\mathrm{r_t} - \mathrm{r_t}\frac{\mathrm{d}^2\phi}{\mathrm{dr}^2} \tag{1.9}$$

$$\frac{\mathrm{Gm}}{\mathrm{r_t^3}} = \Omega^2 - \frac{\mathrm{d}^2\phi}{\mathrm{dr}^2} \tag{1.10}$$

$$\mathrm{r_t^3} = \frac{\mathrm{Gm}}{\Omega^2 - \frac{\mathrm{d}^2\Phi}{\mathrm{dr}^2}} \tag{1.11}$$

Leaving us with the expression for the tidal radius below:

$$\mathrm{r_t} = \left(\frac{\mathrm{Gm}}{\Omega^2 - \frac{\mathrm{d}^2\Phi}{\mathrm{dr}^2}}\right)^{1/3} \tag{1.12}$$

1.3.3 Stellar stream formation

Stellar streams form in the MW mainly from tidal disruption due to its disk, especially for progenitors that have lower radius orbits or pericentres. When in a tidal field, the closer end of the progenitor is pulled towards the galaxy far harder than the other side, as demonstrated in Figure 1.6. The stars, upon being pulled beyond the tidal radius at the Lagrange points can become completely stripped from the satellite progenitor, having velocities just above the escape velocity (Küpper et al., 2008, 2010). Upon leaving the Lagrange points, stripped stars move to different orbits now compared to the progenitor, with those on shorter orbits having a lower time period than it, and the opposite for longer orbits, leaving a leading and trailing portion of the stream as in Figure 1.4. This continues with each orbit, causing stars to stray progressively further from the progenitor and new stars leaving the Lagrange points with similar velocities. This causes streams to gradually grow with time when under regular tidal disruption. The Sagittarius stream, which comes from a massive dwarf galaxy, has the most pronounced progenitor and leading and trailing arms, as shown in this figure as well (Da Costa & Armandroff, 1995; Lynden-Bell & Lynden-Bell, 1995). As explained above in section 1.3.1 however, the vast majority of the thin streams we observe do not have clear progenitors (Grillmair et al., 2015).

1.3.4 Perturbations to stellar streams

Since stellar streams are quite simple structures, i.e. a train of stars roughly on the same orbit, they are sensitive to perturbations. These perturbations can arise from either baryonic effects or from dark matter. To give a sense of the baryonic effects, two streams are believed to be especially affected, the Palomar 5 and Ophiuchus streams. These streams have pericentric passages that lie close enough to the disk that these structures can significantly alter their track, with recent estimates approximately 7.34 kpc for Palomar 5 and 3 kpc for Ophiuchus (Banik & Bovy, 2019; Price-Whelan et al., 2016). In the case of the Galactic bar, when the pericentric passage coincides with the passage of the bar semi-major axis, there are very large difference in force between stream stars aligned with the bar and those still far away from it. This results in a gap forming along the stream, which proceeds to grow over time (Pearson et al., 2017). Alternatively, depending on the bar rotation and whether this is in the same, or opposite direction as the stream, passages of the bar can instead cause a chaotic fanning along the stream, resulting in a series of over and under densities. It is this time dependent nature of the perturbations, due to the rotation of these structures that results in these features along streams, otherwise all stream members would receive the same forces and only their curvature would change (Hattori et al., 2016). Other objects in the disk, such as more compact overdensities in the form of Giant Molecular Clouds (GMCs), also are able to apply larger gaps than the bar or spiral structure (Amorisco et al., 2016)

Stellar streams far out in the halo meanwhile are subject to a lower background potential, which in turn causes them to avoid any perturbations from sources listed above. This makes them good candidates for studying smaller scale perturbations. One such stream, ATLAS-Aliqa Uma (AAU), has noticeable features on its track and no close enough passages to the disk to produce these (Li et al., 2021). This means that encounters with objects in the halo can give quite noticeable effects on the track and density along a stream. Several objects in the halo demonstrate the ability to give significant perturbations, in the form of most satellites we observe in the MW such as GCs and dwarf galaxies. These are especially important objects due to how they would be compact, heavy objects not overly different to a dark matter subhalo. While for lower mass GCs the perturbations would be rather small, they won't be masked as much far out in the halo from the significantly more massive structures in the disk (Thomas et al., 2017, 2018). Exceptions to these would be Sagittarius and LMC however, where here their perturbations to streams would be very pronounced even at longer distance due to their very high masses even compared to the disk. While for certain streams, the effects of GCs and other satellites can often be dismissed based off of model orbits and distances, the LMC and Sagittarius have quite often been able to either significantly perturb or alter orbits of streams (Li et al., 2021). In turn, the perturbed streams can be used to study properties of these objects, such as in Erkal et al. (2019) where the orbit of the OC stream was used to determine the mass of the LMC.

1.4 Constraining dark matter substructure

Naturally, one would first look towards ideas such as gravitational lensing to detect dark matter substructure, given even the lowest mass subhaloes under the WDM and FDM regime would likely exhibit significant lensing if they were in front of a galaxy we are observing. This has succeeded in identifying subhaloes under mass ranges of 10^8 to $10^9\,\mathrm{M}_\odot$, however these are mass ranges allowed for all dark matter paradigms and more than sufficient enough to host populations of stars. Still, there remains the potential for this to detect subhaloes with masses as low as $10^5\,\mathrm{M}_\odot$ with improvements to instruments (Vegetti et al., 2012; Hezaveh et al., 2016). The search for substructure has become increasingly concerned with very low masses, at levels one would not expect star formation to take place at all such as masses of $10^7\,\mathrm{M}_\odot$ or below. A subhalo of this mass would therefore, not be expected to host any population of stars, being a dark matter clump only. Disregarding self-interacting models here, discovering subhaloes of this mass smaller could effectively rule out the lower mass dark matter particles candidates as well, since the lower mass subhaloes are only allowed by CDM (Bullock & Boylan-Kolchin, 2017; Buckley & Peter, 2018).

Other methods of detecting substructure include the Lymen-alpha forest. This has been a good method of mapping out the full scale of the dark matter web throughout the Universe in an attempt to better constrain dark matter. This utilises the consistent absorption lines that would arise due to neutral hydrogen absorbing only specific wavelengths of light in combination with the extremely high luminosities of very distant quasars. The gradual redshifting of this spectra as it travels to us will mean if any more absorption occurred due to a gas cloud between this distant galaxy and us, this absorption line will have a lower wavelength than the initial absorption near the quasar, being less redshifted by the time it reaches us. We can use these absorption lines to create a map of the mass distribution of matter across these distances, and matching these with simulations of different dark matter particles can allow us to better constrain the particle. This method has tended to favour warmer dark matter particles (Viel et al., 2013; Iršič et al., 2017)

Direct acceleration measurements have also been used for detecting substructure. With galaxy stars moving at velocities of order hundreds of kilometres per second, we estimate that over a 10 year period the expected accelerations will give rise to $\sim 10\,\mathrm{cm\,s^{-1}}$ changes in velocity. Doing this for stars throughout the galaxy can allow us to create a scalar field of the forces throughout the galaxy and hence, mass distribution. Silverwood & Easther (2019) predicts that noticeable changes could still be seen for subhaloes with masses as low as $10^7\,\mathrm{M}_\odot$ with scale radii of 250 pc, which is slightly more dense than CDM. Here, these objects would give expected changes in velocities over the 10 years of $1.4\,\mathrm{cm\,s^{-1}}$. Instruments with the primary goal of observing exoplanets are in development and we believe will be able to see to these resolutions, making direct acceleration measurements a promising long term endeavor for both dark matter constraints, along with further evidence for dark matter as a whole (Chakrabarti et al., 2020). Other approaches similar to this also include use of wide binaries such as in Peñarrubia et al. (2016), which can be disrupted in the tidal fields of ultra-faint dwarf spheroidals. These simulated objects had masses $\approx 3\mathrm{x}10^5\,M_\odot$, far greater than their luminosity of magnitude $\mathrm{L} \lesssim 10^4\,\mathrm{L}_\odot$. The disruption of these binary systems can then help discern both the mass and density profile of ultrafaints, in turn being used to better constrain the dark matter particle.

1.4.1 Stellar streams as probes for dark matter substructure

In addition to being great probes of baryonic substructure, stellar streams are also sensitive to dark matter substructure. Recently, the GD-1 and AAU stream in particular have distinct features such as spurs and branches off the track we would struggle to fit using baryonic structures only. Instead, subhaloes have been used and showed some reasonable fits to the sky positions of the streams (Bonaca et al., 2019; Li et al., 2021). By recovering the parameters of these subhaloes such as their masses and scale radius, not only would it make for good dynamical evidence of dark matter substructure, but further help constrain the dark matter particle should it be a sufficiently low mass subhalo (Mocz et al., 2019). Fitting substructure to streams is by no means an easy feat however, and the distant streams we would be most concerned with in particular would naturally come with less data. This will no doubt improve with new surveys from instruments such as the Large Synoptic Survey Telescope (LSST) (Ivezić et al., 2019), the 4-metre Multi-Object Spectroscopic Telescope (4MOST) (de Jong et al., 2012) or the Dark Energy Spectroscopic Instrument (DESI) (DESI Collaboration et al., 2016a,b). This can make it difficult to run full simulations of the generation of some streams, particularly those where we have no clear signature of its progenitor.

Analytic solutions to subhalo-stream encounters

Taking more of an analytic approach on trying to both understand and fit a subhalo to a perturbed stellar stream has yielded promising results on how far we can take streams in general to probe for dark matter. Erkal & Belokurov (2015a,b) used a mix of simulating a stellar stream on a circular orbit, with approximating the subhalo interaction as an impulse approximation. The idea behind this is that the orbital period of the stellar stream is a significantly larger timescale than the actual encounter with the subhalo, so this brief gravitational interaction of the stars receiving a kick towards the subhalo can be assumed to be roughly instantaneous. The evolution of how the stream looked where this encounter took place could then be studied.

The general process for flyby encounters and their effects is demonstrated in Figure 1.7 followed an initial compression of the stream, where the high potential of the subhalo attracts nearby stream stars, either dragging stars away from their direction of motion and slowing them down, or towards it and accelerating them. These changes in velocities then require the stars to take on different orbits as this encounter causes stars to either gain or lose energy and angular momentum. This effect here is similar to how streams form from tidal disruption. Here, the stars that lost energy slow down and enter closer orbits to the galactic centre, while those gaining energy do the opposite. The lower energy stars, now on lower radius orbits move along the stream due to their shorter orbital period, with the opposite for the higher energy stars, and a gap begins to form around where the flyby took place. With enough time these stream particles overtake those less involved in the impact and a caustic forms. This would then appear as an effective gap along the stream, or in the case of lower mass subhaloes would still leave a drop in density of the stream where the encounter took place.

This has additionally been applied to real data such as the Pal-5 stream in Erkal et al. (2017). Here, over and under densities along the stream hinted at this very behaviour of gap formation, and by applying a simular technique using an impulse approximation summarised in Sanders et al. (2016), the features could be fit using this encounter. This impulse approximation has an advantage in that for the real data it allowed a different technique to modelling the stream without simulating its full evolution in an N-body sense, instead using cubic splines to model the stream.

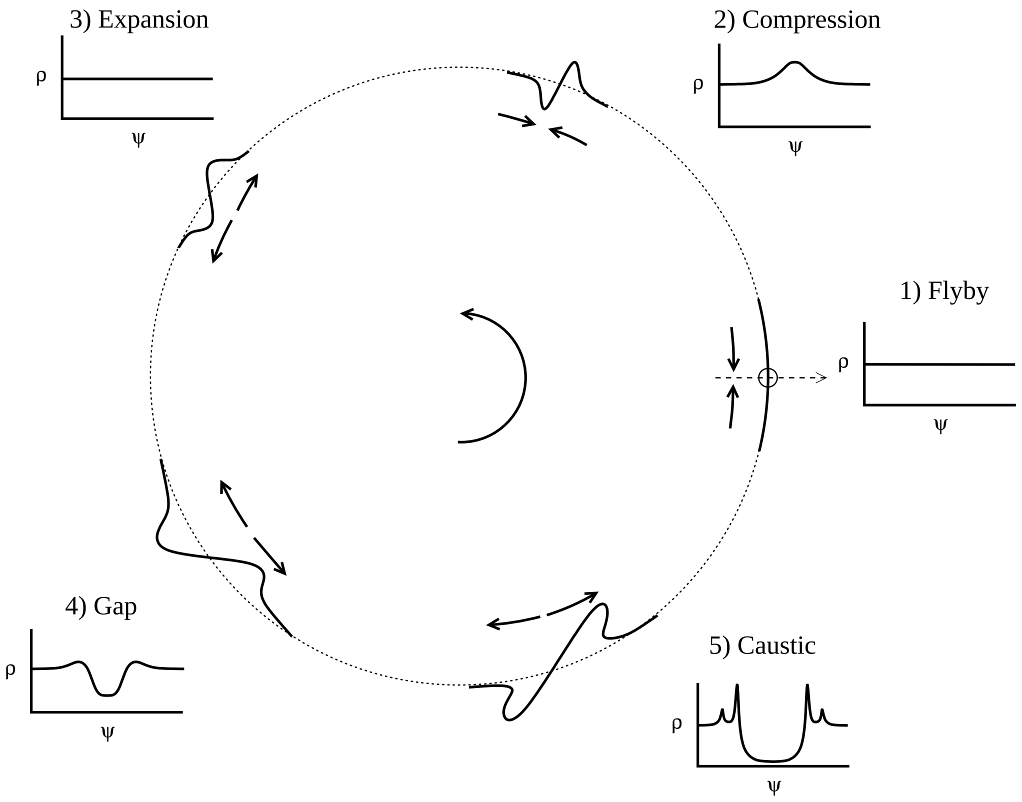

Figure 1.7: Demonstration of the formation and development of a stream gap from a perturbation from a subhalo like object. For this example, the stream is rotating counter-clockwise on a circular orbit following the dotted line. There are then 5 snapshots displayed for the 5 phases of the flyby, as the solid black lines with corresponding graphs of the density with respect to the angle along the stream. Each graph is centred on ψ which denotes the point of closest approach between the subhalo and stream. The 5 phases are as follows: 1, Flyby, the stream immediately before the flyby maintains a uniform distribution throughout in density. 2, Compression, the subhalo pulls particles towards its position during closest approach, hence, the density of the stream at ψ increases to higher than the rest. 3, Expansion, particles that were pulled towards ψ take on different orbits. Those pulled further along the stream now have more energy, take on an orbit with a longer period, and gradually fall behind, and vice versa for those pulled backwards. 4, Gap, continuing these new orbits for the stars involved in the compression leads to them moving even further along and down the stream, and the density around ψ now drops compared to the rest. 5, Caustic, particles not involves in the stream begin to overtake the perturbed stars as they continue to drift along and down the stream, and caustics begin to form. Image used from Erkal & Belokurov (2015a)

Another approach to the subhalo interactions using the impulse approximation involves not a single impact, but the generation of a stream in the presence of large population of subhaloes (Bovy et al., 2017a). Here, when in the presence of and perturbed by a realistic population of low mass subhaloes, the features mentioned above can be hard to discern due to the quantity of encounters. This does not mean it is impossible to find remnants of prior subhalo-stream encounters in streams however. Instead, they could find fluctuations within the power spectrum of the density and stream track. These correlated with subhalo mass, so analysis of this of observed streams could potentially reveal a suite of past encounters and could work for subhaloes as low mass as $10^5\,\mathrm{M}_\odot$. This was also applied to the Pal-5 stream and showed promise of recreating features in its density profile through subhaloes, albeit in a different fashion to Erkal et al. (2017).

Simulating subhaloes with streams

In order to get a more realistic scenario for subhalo-stream encounters, another approach is to integrate the subhalo on its own orbit in addition to the stream instead of the analytic impulse approximation. This technique can be seen in work such as Bonaca et al. (2019), where features in the GD-1 stream were being fit using subhaloes, including gaps along the stream and spurs branching off of the track by as much as 1 deg perpendicular to the stream. The affect of this encounter did still produce similar behaviours in the stars as the analytic impulse approximation by Erkal & Belokurov (2015a). Obviously this recreated the gap well, but in order to create the spur in the stream, the subhalo they used needed to be extremely dense, being modelled by a Hernquist profile of mass $5\mathrm{x}10^6\,\mathrm{M}_\odot$ but scale radius only 10pc. A subhalo of this mass would be expected to have a scale radius at least 10 times more than this under CDM. Currently, no luminous satellites appear to get close enough to this stream, however, we have only determined orbits for around half of the roughly 50 known dwarf galaxies in the MW and this could potentially shed new light on this McConnachie (2012). Furthermore, the streams generated here do have a series of simplifications made on them, particular to how they are generated. The progenitor is integrated and stars are regularly injected at the Lagrange points, forming a perfectly thin stream or particle train, compared to real streams which exhibit a wide range of widths and velocity dispersions.

GD-1 is not the only stream known to have stars perturbed perpendicular to the track in this fashion, with AAU having a kink which has stars along the track displaced by as much as 2 deg (Li et al., 2021). With the discovery of this kink feature only a few years ago, this makes it a good candidate to uncover more potential subhalo interactions. Our work here had the goal of not only attempting to fit this stream, but to do so using a more realistic method based off of the above techniques. The technique we employ will be the same method as in Erkal et al. (2019) along with integrating the full orbit of the subhalo such as in Bonaca et al. (2019).

The modified Lagrange Cloud Stripping method

For generating streams in our work below, we use a modified Lagrange Cloud Stripping method, with further details of it outlined in Gibbons et al. (2014), which is the same method used in Erkal et al. (2019). This method avoids the need to generate a fully N-body GC and strip stars from it using the background potentials, which would be highly computationally intensive. Instead, we simply model the progenitor analytically as a Plummer sphere with mass and scale radius detailed below, and inject new particles which make up the stream itself during integration. Compared to fully modelling an N-body cluster, this method had been shown to be up to 3 orders of magnitude faster. We need to inject these particles at the inner and outer Lagrange points, which is where stars are stripped from their progenitors and form the stream as seen in Figure 1.6, parameterised by $\mathrm{x_L}$. By definition, this Lagrange point is at a radius of the progenitor shifted by the tidal radius $\mathrm{r_t}$ either towards the galactic centre for the inner Lagrange point, or away from the galactic centre for the outer Lagrange point.

The first step of our stream generation is to use an input of present day positions of a progenitor, and do an initial rewind for a duration which we label here $\mathrm{T_{max}}$. For all our streams, we set this to 4 Gyr. Following this, stripped stars are then injected and placed at the inner and outer Lagrange points. This is done by placing them on a line that connects the progenitor to the galactic centre with offset in radius $\pm\,\mathrm{r_t}$, where this instantaneous tidal radius is calculated above in equation 1.12.

This equation demonstrates how by using a higher mass progenitor, particles will be injected at higher distances and hence will result in thicker streams which matches our understanding from observations. The stars which are injected are given velocities drawn from a Gaussian distribution to match the stream dispersion, and continuously injected at times drawn from a Gaussian until the integration reaches the present day at $\mathrm{T} = 0$. The overall rate at which we inject stars here is set to be 2000 stars per orbit, where stars are injected evenly between the inner and outer Lagrange point. Stars injected in the inner Lagrange point as expected will move forward along the stream and make the leading arm, with those at the outer Lagrange point forming the training arm. Throughout the 4 Gyr integration, by the present day we end up with a stream of $\sim$ 12000 stars. The stars here are collisionless with each other and the progenitor. The rest of the background potentials of the MW we use are outlined in the following section. All integration uses a simple 2nd order kick-drift-kick algorithm (Springel, 2005).

Starting out from the present day followed by integrating backwards is necessary in the context of fitting streams. This ensures that the stream generated will be located at the specified coordinates of where the progenitor was. This also allows the background potentials to be easily modified without drastically affected the present day stream position, as by first integrating backwards in a newly modified potential, it simply means the progenitor will change at $\mathrm{T} = -\mathrm{T_{max}}$ accordingly the maintain the same present day location. For when additional potentials are added, such as the bar or a dark matter subhalo, we also rewind the stream progenitor in the presence of them as they could alter the progenitor orbit.

Thesis structure

Outlined in this thesis, our primary aim is to use one particular stream, AAU, to detect dark matter substructure. In Chapter 2, we use this modified Lagrange Cloud Stripping method of generating streams to first demonstrate a proof of concept, of how we can continue to recover the subhalo parameters from a perturbed stream. This will serve as an expansion on the work of Erkal & Belokurov (2015b), instead using these fully numerical approaches to subhalo-stream encounters instead of the analytic impulse approximation to a infinitely thin stream. We then apply this to observations of the AAU stream in Chapter

3 to try and recover properties from real subhaloes, as this could potentially make for a very important result in further constraining the dark matter particle. Finally, we explore what baryonic effects might also be playing a role with some more advanced bar models to what has been used before in Chapter 4 and conclude our work in Chapter 5

Chapter 2

Inferring dark matter subhalo properties from simulated subhalo-stream encounters

In this chapter I apply the findings of Erkal & Belokurov (2015a) and Erkal & Belokurov (2015b) on fitting subhalo parameters to perturbed streams to a more realistic MW scenario. By demonstrating that subhalo parameters can be recovered from N-body simulations of streams with realistic properties and orbits, this opens the path to applying this to real streams, and I showcase how this can be done using different qualities of observational data such as what present day instruments can obtain. The work below is laid out exactly as my paper which has been submitted to MNRAS and is awaiting review (Hilmi et al., 2024).

2.1 Abstract

In the cold dark matter paradigm, our Galaxy is predicted to contain >10000 dark matter subhaloes in the $10^5 - 10^8\,\mathrm{M}_\odot$ range which should be completely devoid of stars. Stellar streams are sensitive to the presence of these subhaloes, which can create small-scale features in streams if they pass closely enough. Modelling these encounters can therefore, potentially recover the subhalo's properties. In this work, we demonstrate this for streams generated in numerical simulations, modelled on eccentric orbits in a realistic Milky Way potential, which includes the Large Magellanic Cloud and the subhalo itself. We focus on a mock model of the ATLAS-Aliqa Uma stream and inject a $10^7\,\mathrm{M}_\odot$ subhalo, creating a similar discontinuous morphology to current observations. We then explore how well subhalo properties are recovered using mock stream observations, consisting of no observational errors, as well as assuming realistic observational setups. These setups include present day style observations, and what will be possible with 4MOST and Gaia DR5 in the future. We show that we can recover all parameters describing the impact even with uncertainties matching existing data, including subhalo positions, velocities, mass and scale radius. Modelling the subhalo on an orbit instead of assuming an impulse approximation, we greatly reduce the degeneracy between subhalo mass and velocity seen in previous works. However, we find a slight bias in the subhalo mass (~ 0.1 dex). This demonstrates that we should be able to reliably extract the properties of subhaloes with stellar streams in the near future.

2.2 Introduction

In the cold dark matter paradigm, structure formation proceeds in a hierarchical fashion (e.g. White & Rees, 1978). In the early Universe, small-scale overdensities collapse first, forming small haloes that merge together to form larger and larger haloes. As a result, the dark matter halo of a galaxy like the Milky Way is expected to contain a plethora of dark matter subhaloes spanning a wide range of masses at the present day (Klypin et al., 1999; Moore et al., 1999; Springel et al., 2008). While the most massive of these dark matter subhaloes host dwarf galaxies, below a mass of $\sim 10^8\,\mathrm{M}_\odot$ they are believed to be devoid of stars (e.g. Somerville & Davé, 2015; Jethwa et al., 2018; Nadler et al., 2021).

Detecting these starless dark matter subhaloes would be a confirmation of the dark matter paradigm and would allow us to probe the properties of the dark matter particle itself. For example, in warm dark matter, these subhaloes should only exist down to the free-streaming scale below which the thermal motion of particles in the early Universe washes out substructure (Bond & Szalay, 1983b; Bode et al., 2001b). This free-streaming scale is set by the mass of the warm dark matter particle and thus the detection of low-mass subhaloes can constrain the mass of the dark matter particle. Similarly in fuzzy dark matter, low mass subhaloes are suppressed due to quantum pressure (e.g. Hui et al., 2017). Thus these dark matter subhaloes act as a magnifying glass with which we can examine the properties of the dark matter particle.

Stellar streams in the Milky Way have long been thought of as an excellent detector of these dark matter subhaloes (e.g. Ibata et al., 2002; Johnston et al., 2002; Siegal-Gaskins & Valluri, 2008; Carlberg, 2009). These streams form as globular clusters (GCs) or dwarf galaxies tidally disrupt in the presence of the Milky Way. Once stripped, the stars in the stream follow roughly the same orbit and thus the streams appear to roughly trace great circles on the sky. Despite their seeming coherence, the streams are fragile structures. The passage of a nearby subhalo imparts velocity kicks on the stream stars which subsequently changes their orbit around the Milky Way, creating gaps and wiggles in the stream (e.g. Yoon et al., 2011; Carlberg, 2012; Erkal & Belokurov, 2015a).

In order to extract the properties of subhaloes with stellar streams, two different approaches have been proposed. Bovy et al. (2017b) showed that the statistical properties of the perturbed stream (e.g. the power spectrum of the density fluctuations) can be used to estimate the population of subhaloes that the stream has been exposed to. This is done by repeatedly forward modeling the stream in the presence of varying amounts of substructure and comparing the statistical property of the resulting streams with the observed stream. Banik et al. (2021b,c) used this approach to set one of the tightest constraints on the mass of the dark matter particle using observations of the GD-1 (Grillmair & Dionatos, 2006b) and Palomar 5 (Odenkirchen et al., 2001b) streams. While this approach can be used to measure the statistical properties of the dark matter subhalo population, it cannot be used to identify individual subhalo encounters.

The second approach is to fit individual subhalo impacts and extract each impactor's properties. Erkal & Belokurov (2015b) use an analytic model for a stream initially on a circular orbit that is perturbed by a subhalo using the impulse approximation. They showed that it is possible to extract all of the properties describing the subhalo's flyby (i.e. the subhalo mass, size, impact position and velocity, and impact time) using observations of the perturbed stream. They further showed that this inference is possible even with realistic observational errors similar to what is possible at the present day. Bonaca et al. (2019) attempted a fit to the perturbed GD-1 stream first observed in Price-Whelan & Bonaca (2018). In order to fit the perturbed GD-1 stream, Bonaca et al. (2019) assumed that all of the stars in the stream were on the same orbit, i.e. that GD-1 was an infinitely cold stream. They found that perturbers in the mass range $10^6 - 10^8 \mathrm{M}_\odot$ could produce similar features to what is observed.

The goal of this work is to build on the work of Erkal & Belokurov (2015b) and Bonaca et al. (2019) to fit realistic stream models to perturbed stellar streams. In order to make the stream models as realistic as possible, the models will be generated with the modified Lagrange Cloud stripping technique (Gibbons et al., 2014). For further realism, we also do not assume the subhalo's perturbation can be described with the impulse approximation. Instead, we inject a subhalo that orbits in the Milky Way with the stream in order to self-consistently perturb it.

In order to test how well this inference works, we use a mock stream inspired by the ATLAS-Aliqa Uma (AAU) stream. Initially, the two segments of this stream were discovered individually as the ATLAS stream by Koposov et al. (2014) in the VST ATLAS Survey DR1 (Shanks et al., 2015), and a separate Aliqa Uma stream by from the Dark Energy Survey from Shipp et al. (2018). As a result of their different distances of ∼20 kpc and ∼28 kpc respectively, their differing on-sky alignment, and their being ∼1 deg apart on the sky, ATLAS and Aliqa Uma were initially thought of as two separate streams. Spectroscopic follow-up by the Southern Stellar Stream Spectroscopic Survey (S^5; Li et al., 2019; Li & S5 Collaboration, 2021; Li et al., 2022) then revealed that ATLAS and Aliqa Uma had kinematics and metallicities consistent with a single stream (Li et al., 2021). Li et al. (2021) argued they were one stream (dubbed the AAU stream) with a significant 'kink'-like perturbation. What was most unusual was that outside the kink itself, the stream was relatively unperturbed, with an otherwise thin, smooth track on either side of the kink. Furthermore, they showed that this highly localized perturbation was difficult to recreate using baryonic structures (e.g. dwarf galaxies impacts, the bar, spiral arms, or giant molecular clouds), hence making it an interesting stream to study for the purpose of probing dark matter substructure.

Our paper is structured as follows; in Section 2.3 we describe how we set up a stream-subhalo encounter, including summarising our code and how encounters are described using 8 key parameters. In Section 2.4 we describe our mock impact and outline the different observational uncertainties we use, alongside how we fit the subhalo properties itself. We then outline and describe the results in Section 2.5, and discuss the implications of these results in Section 2.6. Finally, we present our conclusions in Section 2.7.

2.3 An overview of the setup

In this section, we outline the process of generating stellar streams that have been perturbed by a subhalo-like object. We split this into 3 subsections, corresponding to the major steps involved in doing so, with a rough outline detailed below.

Our work aims to fit a perturbed stellar stream in order to extract the properties of the perturber. To do this, we use a setup that follows a consistent set of impact parameters that define when an encounter took place, and the subhalo properties and dynamics relative to the stream. Our procedure of generating a perturbed stream consists of three steps:

- We initially generate a stream in the absence of any subhalo. The stream is integrated up until the impact time so that the subhalo's position at the impact time can be determined.

- We then place a subhalo at the final snapshot of the first step (i.e. at the impact time), with the impact parameters allowing us to determine its position and velocity at this time. We then integrate the subhalo forward to the present day to get its present-day phase space coordinates.

- Finally, we rewind the progenitor and subhalo backward from the present day and then integrate the stream and subhalo up until the present day to generate a stream perturbed by a subhalo. We stress that during the rewinding, our subhalo can affect the progenitor's past orbit, and thus the full effect of the subhalo is self-consistent. While our impact parameters ensure we have that specific encounter, we make no assumption that this is the only impact taking place. The inclusion of the subhalo throughout integration from stream generation to the present day adds the possibility for additional interactions.

We note our approach assumes that the stream progenitor initially disrupts around the Milky Way producing a stream that is then perturbed by a subhalo. While this is quite a general tool for modelling perturbers, it cannot be used to model a globular cluster stream that forms by first disrupting around a dwarf galaxy and subsequently being accreted onto the Milky Way (e.g. Malhan et al., 2020).

2.3.1 Generating an unperturbed stream

The first step is to generate a model of an unperturbed AAU stream following the best-fit model in Li et al. (2021). We use this unperturbed model of AAU since our goal is to create a mock of a stream with a similar morphology to the AAU stream. This stems from the idea that these stream subhalo encounters could make for a good candidate for a feature such as the AAU kink.

We model our stream progenitor as a Plummer sphere (Plummer, 1911) with a mass of $2 \times 10^4\,\mathrm{M}_\odot$ and a scale radius of 10 pc. This progenitor matches fits to the AAU stream in Li et al. (2021), which is a GC progenitor similar to those involved in the formation of the Palomar 5 stream (Erkal et al., 2017). We generate the stream in the following gravitational potential:

- The Milky Way potential determined by McMillan (2017) with accelerations defined using the C++ library of `galpot` (Dehnen & Binney, 1998a). This potential has 6 components; a bulge, spherical NFW dark matter halo (Navarro et al., 1997), thick and thin disk, and atomic and molecular hydrogen gas disks. Following the approach and results of Li et al. (2021); Shipp et al. (2021), we use the same draw of the potential from the posterior chains of McMillan (2017). Li et al. (2021) explored several realizations and selected the one that gives the best fit to an unperturbed AAU stream. For the Sun's position, we use $\mathrm{R}_0 = 8.22844\,\mathrm{kpc}$, and a velocity of $(U_\odot, V_\odot, W_\odot) = (8.40569, 12.0149, 7.28025)\,\mathrm{km\,s^{-1}}$ which are both specified by the draw from posterior chains in McMillan (2017). The parameters of this potential are given in Table A.3 of Shipp et al. (2021).

- The Large Magellanic Cloud (LMC) is modeled as a Hernquist profile (Hernquist, 1990) with a mass of $1.5 \times 10^{11}\mathrm{M}_\odot$ and a scale radius of 17.13 kpc as in Li et al. (2021) who fit the unperturbed portion of the AAU stream. Similar to that work, we choose this mass and scale radius which matches the LMC enclosed mass at 8.7 kpc (van der Marel & Kallivayalil, 2014). We note that this LMC mass is consistent with measurements from stellar streams, LMC satellites, and LMC globular clusters (e.g. Erkal et al., 2019; Erkal & Belokurov, 2020; Shipp et al., 2021; Vasiliev et al., 2021; Koposov et al., 2023; Watkins et al., 2024). We include the LMC alongside the Milky Way potential since it has a large effect on the AAU stream (e.g. Shipp et al., 2019, 2021; Li et al., 2021) and so that the same model can be used to fit the real AAU stream in future work.

In order to generate the stream, we start with the present-day (i.e. $\mathrm{t} = 0$) position and velocity of the progenitor, along with the LMC. The stream progenitor and the LMC are then integrated backward for a total of 4 Gyr, which we will henceforth refer to as $\mathrm{t}_{\mathrm{max}}$. While this integration takes place, the Milky Way position is not fixed due to the reflex motion on it exerted by the LMC (e.g. Gómez et al., 2015; Erkal et al., 2021). This approach allows us to obtain positions for the LMC, MW, and our progenitor which can be used when integrating forwards from $\mathrm{t} = -\mathrm{t}_{\mathrm{max}}$. We use these positions when integrating forwards to avoid recomputing the forces again and interpolate their positions to suit our variable timestep.

The generation of the stream itself uses the modified Lagrange Cloud stripping method (Gibbons et al., 2014) as adapted in Erkal et al. (2019) to include the LMC. We take a progenitor, modeled as a Plummer sphere and inject particles from the progenitor's inner and outer Lagrange points. This is done at randomly selected time intervals drawn from a Gaussian centered on each pericenter, with a mean of 2000 particles injected every pericenter. These particles are injected with velocities drawn from a Gaussian distribution chosen to match the velocity dispersion of the stream. The perturbed stars at the outer Lagrange point will therefore drift behind the progenitor and form the trailing arm of the stream, with those at the inner Lagrange drifting ahead and forming the leading arm. For our 4 Gyr integration to the present day, we end up with a stream of 12,000 stars. We note that for the purpose of simulating the encounter, however, we do not integrate forwards to the present day in this initial step. Instead, we integrate until the time we intend to inject the subhalo for the encounter.

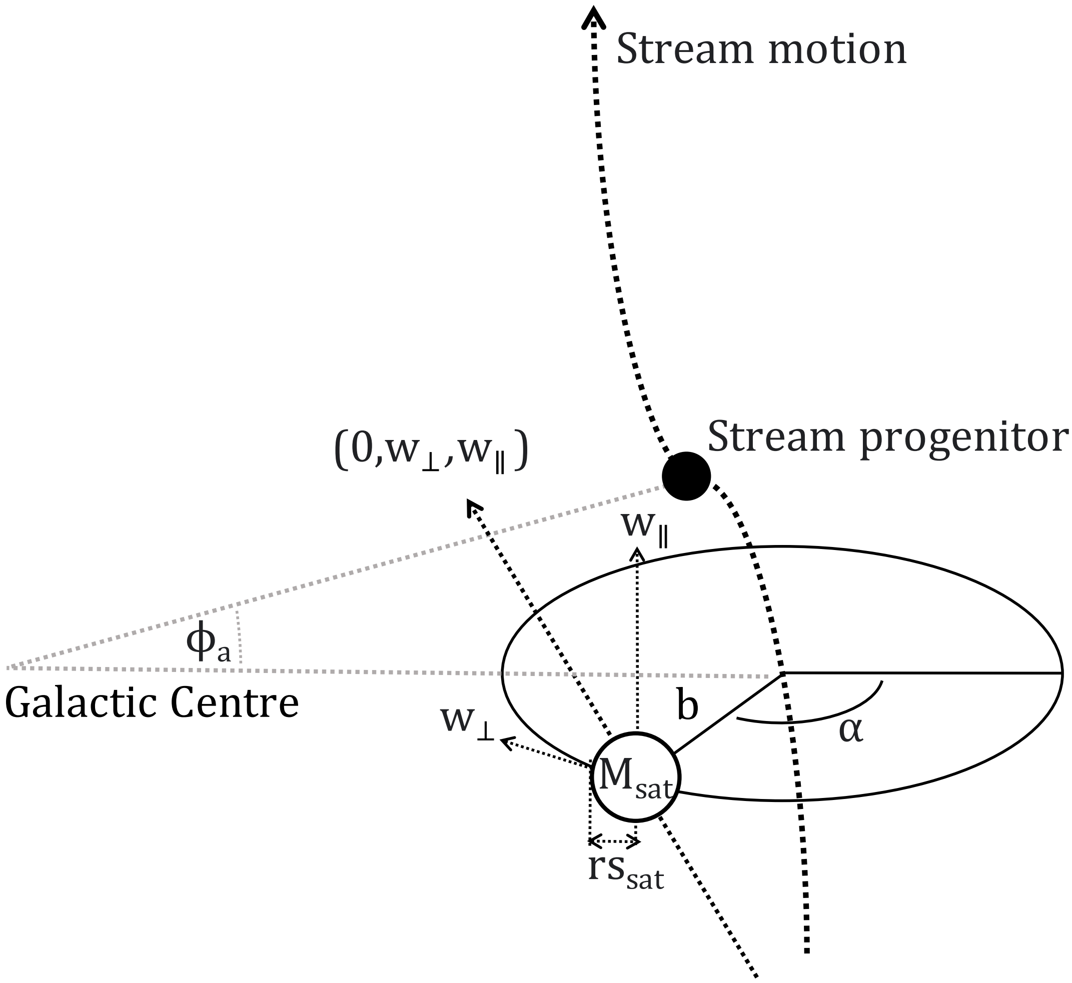

Figure 2.1: The setup of the Subhalo-Stream encounters, showcasing 7 of the 8 key impact parameters (the other being the time it took place prior to the present day, T_a). The setup follows a cylindrical polar coordinate system, centered on the stream at angle ϕ_a

2.3.2 Modelling the subhalo-stream encounter

Next, we describe how we initialize the subhalo properties given the unperturbed stream. Our encounters are modeled following the schematic shown in Figure 2.1. Using the stream produced in Section 2.3.1, we use this to correctly align and position the subhalo with our impact parameters. In total, 8 parameters are used to describe these encounters, which are chosen to match the setup used in Erkal & Belokurov (2015a), and shown in Figure 1 in their respective paper. The parameters are as follows:

b: The impact parameter, i.e. the distance of the closest approach between the subhalo and stream. As a result, this is aligned so that it is roughly perpendicular to the stream and its motion.
α: An angle describing the orientation of the subhalo's closest approach to the stream. For a cylinder aligned along the stream, this angle would represent the cylindrical polar angle. This cylinder would run perpendicular to a line between the Galactic centre and the stream.
$\mathrm{w}_{\perp}$: The velocity of the subhalo perpendicular to the stream. This is aligned as a tangential velocity about α.
$\mathrm{w}_{\parallel}$: The velocity of the subhalo aligned parallel to the stream's velocity vector.
$\mathrm{T_a}$: The impact time, with the encounter set to occur at $\mathrm{T} = -\mathrm{T_a}$
ϕ_a: The angle relative to the stream progenitor the encounter occurred. The other parameters relating to position and velocities are hence, aligned with this.
$\mathrm{M_{sat}}$: The subhalo mass
$\mathrm{rs_{sat}}$: The scale radius of the subhalo, which we assume to be a Plummer sphere

As the above parameters are defined relative to the position and velocities of the stream, we take a mean value of the stars local to where the encounter would be. At ϕ_a, we take a 0.5 deg slice to select only a local sample of stars for this. Once the subhalo can be placed with the relative positions and velocities, we then integrate it forward to the present day so that we can self-consistently rewind the progenitor in the presence of the subhalo in the next step.
Similar to Erkal & Belokurov (2015b), we elect to fit the mass and scale radius of the subhalo independently (i.e. with no constraints on how they are related) as we do not want to restrict the possibility of these encounters to only certain dark matter paradigms. We note that for our fiducial impact, we select a subhalo mass and scale radius that match what is expected in ΛCDM.

2.3.3 Generating the perturbed stream

Finally, a stream is generated in the same process as Section 2.3.1, though with the inclusion of the subhalo from the start of integration time. This is necessary so that we can self-consistently model the full effect of the subhalo, accounting for the orbit it is on and allowing for multiple impacts with the stream. We use the present-day positions of the subhalo and stream and rewind it to $\mathrm{t} = -\mathrm{t_{max}}$, once again doing the same for the MW and LMC. This initial rewind means we can guarantee the stream ends up at the same present-day positions regardless of the subhalo properties, which may otherwise shift the orbit. This is one of the key advantages over carrying out the encounters using initial conditions at $\mathrm{t} = -\mathrm{t_{max}}$.

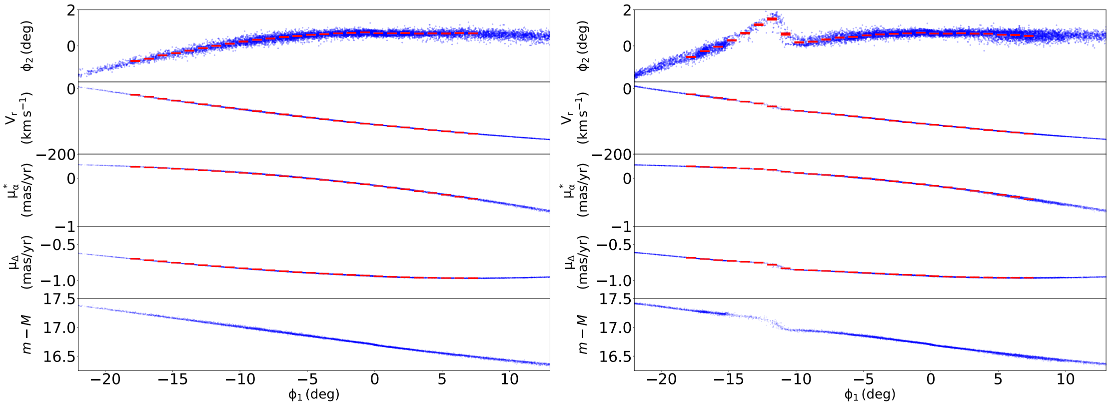

Figure 2.2: A comparison of a stream generated subject to only the background potentials and LMC as described in Section 2.3.1 (left) vs our mock stream that had additionally undergone a subhalo flyby (right). The exact parameters used here are $\mathrm{b} = 0.1\,\mathrm{kpc}$, $\alpha = 250\,\mathrm{deg}$, $\mathrm{v}_{\perp} = 35\,\mathrm{km\,s^{-1}}$, $\mathrm{v}_{\parallel} = -10\,\mathrm{km\,s^{-1}}$, $\mathrm{M_{sat}} = 10^{7}\,\mathrm{M_{\odot}}$, $\mathrm{T_a} = 0.25\,\mathrm{Gyr}$, $\phi_{\mathrm{a}} = -6\,\mathrm{deg}$, $\mathrm{rs_{sat}} = 0.3\,\mathrm{kpc}$. The physical definitions of these parameters are outlined in figure 2.1 and Section 2.3.2. Both panels showcase the main stream observables in each row and these are outlined as follows: *Top row:* Stream track, with errorbars every 1 deg bin showing the mean ϕ_2 position of stars. *Second row:* The radial velocities, with red errorbars in the same bins as the stream track showing mean radial velocities. Third and fourth row: The proper motion with similar errorbars for their respective bins. Bottom row: Distance modulus

2.4 Fitting subhalo properties

Here, we showcase the encounter we use to generate the mock perturbed stream, along with the different sets of data we generate from this with the setups differentiated by the data quality. We then explain our approach to recovering subhalo properties from this mock data by determining the likelihood.

We follow largely the same process as Erkal & Belokurov (2015b) with a more realistic setup. In this work we use a realistic stream model instead of a train of particles on the same orbit which naturally accounts for the growth of the stream. Furthermore, we do not make use of an impulse approximation since our subhalo is integrated alongside the stream in the simulation. Finally, our setup allows us to model streams on eccentric orbits.

2.4.1 The mock impact

The exact parameters of our mock impact are as follows: $\mathrm{b} = 0.1\,\mathrm{kpc}$, $\alpha = 250\,\mathrm{deg}$, $\mathrm{v}_{\perp} = 35\,\mathrm{km\,s^{-1}}$, $\mathrm{v}_{\parallel} = -10\,\mathrm{km\,s^{-1}}$, $\mathrm{T_a} = 0.25\,\mathrm{Gyr}$, $\phi_{\mathrm{a}} = -6\,\mathrm{deg}$, $\mathrm{M_{sat}} = 10^{7}\,\mathrm{M_{\odot}}$, $\mathrm{rs_{sat}} = 0.3\,\mathrm{kpc}$. These were chosen as the resulting stream track has a similar discontinuous morphology to the AAU stream with its kink feature. The same stream and observables,

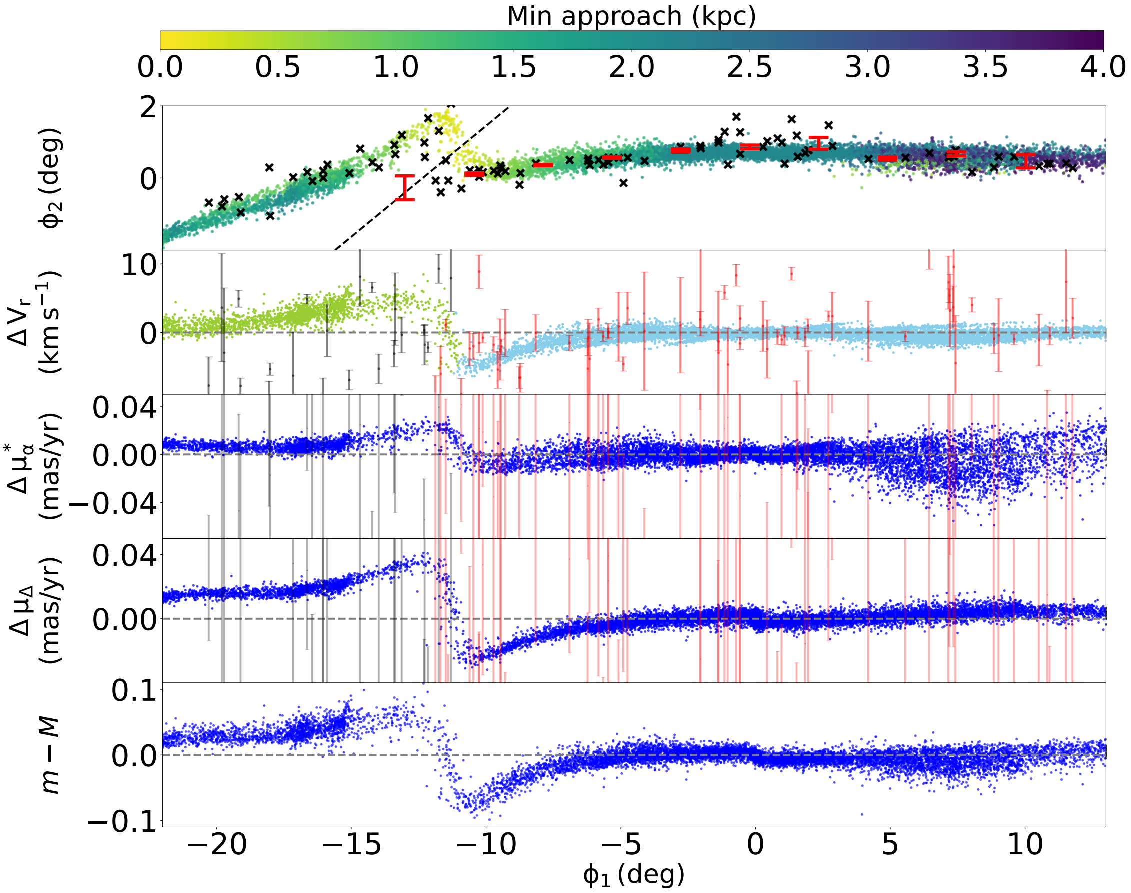

Figure 2.3: Mock data of our perturbed stream with real AAU data overlaid. *Top row:* Stream track, with the minimum approach distance between individual mock stream stars and the subhalo shown in the colour bar. The black data points highlight the on-sky location of the observed stars. We also show a dotted line that separates the observed stars as belonging to either the ATLAS half of the stream (right of the kink) or the Aliqa Uma half (left of the kink). *Second row:* The radial velocity differences between the mock perturbed stream and a fourth-order polynomial fit of V_{GSR} for the unperturbed model, with mock observables shown as red errorbars if in ATLAS and black errorbars if in Aliqa Uma. The model stars belonging to the ATLAS part of the stream are shown in light blue, and Aliqa Uma in green. Third and fourth row: The proper motion differences between the perturbed stream and a fourth-order polynomial fit, with mock observables shown once again as errorbars, much in the same vein as the radial velocities. Bottom row: Distance modulus difference between the perturbed stream and a fifth-order polynomial fit to the unperturbed model.

both with and without the subhalo encounter can be seen in Figure 2.2.

Additionally, we show how the current AAU data compares to this mock impact in Figure 2.3. This showcases features in not only track and radial velocities, similar to what was seen in Li et al. (2021), but for proper motions. In the case of the proper motions, however, the scale of these seen in the mocks is far smaller than the errors of our current observations ($\lesssim 0.04$ mas/yr) so we would not expect to see this in AAU data. In addition, this mock has similar behaviour outside the kink where the rest of the track appears relatively unperturbed.

We make mock observations in three different scenarios, corresponding to different uncertainties in the data. These setups have different observational errors and different numbers of stars in the observables of radial velocities and proper motions. In each scenario, we then generate our final set of mock data by drawing each mock observation from a Gaussian with their respective error distributions.

We note, however, that in all cases we use the same errors for the stream track. In order to ensure that the random seed chosen to simulate the stream does not have a significant effect of the observables, we increase the mock uncertainty in the track by a factor of 5. The resulting observables have similar errors to present-day AAU observations along the stream track, and we, therefore, elect to use the same errors for data in these observables, only changing the quantity and location of data. Further details of each error scenario (hereafter, Scenario 1, Scenario 2, Scenario 3) are explained below.

Scenario 1: No observational errors

In this case, we use mock observations of the mean track of the stream in each observable and do not include any intrinsic uncertainties. Here, data is evenly spaced in 1 deg bins in ϕ_1, and this is generated for each of the track, radial velocities, and both components of proper motions. In total, each observable has 26 data points between ϕ_1 of $-17.75°$ and $7.25°$.

Scenario 2: Present day observational error

In this setup, the quantity of data for observables and their errors closely match today's measurements of the AAU stream. The radial velocities and both proper motions individually consist of 96 stars, and are not evenly spaced throughout ϕ_1 like in the no error scenario. Instead, their positions in ϕ_1 match those of the AAU stream. We additionally modify the stream track data to be spaced more accordingly with our present-day spline fits in Li et al. (2021). The result is 17 data points evenly spaced in 2 deg bins in ϕ_1, with the total range being between between $-20°$ and $12°$.

Scenario 3: Future predicted observational errors

Looking forward, we investigate a mock up a future setup based on the expected performance of the Large Synoptic Survey Telescope (LSST), 4-metre Multi-Object Spectroscopic Telescope (4MOST), and the final data release of *Gaia*. Here, our data for radial velocities now consist of 515 stars with an error ranging between $\sim$1 and $\sim$10$\mathrm{km\,s^{-1}}$, which would be enabled from 4MOST spectroscopic measurements to higher magnitude stars (r-mag of

21 compared to the current limit of 19.8) (de Jong et al., 2012). While LSST would be able to observe a far greater number of stars, the errors show little improvement to current AAU data (errors starting from $\sim 2\,\mathrm{mas\,yr^{-1}}$, which only improves upon approximately half of the current AAU proper motion errors) (Eyer et al., 2012). Our proper motions instead follow predictions from 10 years of *Gaia* observations, where our dataset consists of 96 stars, but we improve on the present sample errors by a factor of ~6.6 due to how the proper motions uncertainty scale as $\mathrm{t}^{-1.5}$ (Gaia Collaboration et al., 2023). This gives a sample with errors ranging between ~0.005 and $\sim 0.05\,\mathrm{mas\,yr^{-1}}$. We keep the stream track data the same as the present-day error scenario.

The mock data that would be expected from these future surveys was made by matching an isochrone to real AAU data, in a similar approach to Erkal & Belokurov (2015b) and Li et al. (2021). Here, this data was matched to the MIST isochrone sets (Dotter, 2016; Choi et al., 2016) with the following parameters giving the best match; Stellar metallicity: $[\mathrm{Fe/H} = -1.99]$, $[\alpha/\mathrm{Fe} = 0.4]$, Helium mass fraction: $[\mathrm{Y} = 0.4]$ and age $\sim 11.2\,\mathrm{Gyr}$. These were then interpolated using the `minimint` Python library (Koposov, 2021). We use an initial mass function (IMF) following Chabrier (2005). This is scaled so that under the range covered by current AAU data ($14.8 \leq \mathrm{r} \leq 19.8$) the resulting luminosity function has the expected number of 96 stars contained within it, which equates to the current availability of radial velocity and proper motion data. The cumulative luminosity function of these stars is shown in Figure 2.4. This estimate results in a sample of 515 member stars that 4MOST will observe at $r < 21$ mag.

2.4.2 Likelihood Estimation

We compute the log-likelihood of our encounters by assuming Gaussian errors for all observables. This gives a likelihood of

$$\ln \mathcal{L} = \sum_i \left(\ln \left(\frac{1}{\sqrt{2\pi\sigma_i^2}} \right) - \frac{(o_i - m_i)^2}{2\sigma_i^2} \right). \tag{2.1}$$

where i denotes the index of the bin in ϕ_1 along the stream, o_i is the centroid for the simulated data in this bin, m_i is the centroid for the model mock data in this bin, and σ_i is the sum in quadrature of the uncertainty in the simulated data and the model mock data. This is carried out on the 4 observables, which are the stream track ϕ_2, radial velocities $\Delta\,\mathrm{v_r}$, and 2 proper motions, μ_α^* and μ_δ. Similar to Erkal & Belokurov (2015b), we assume that these 4 observables are independent, so the total log-likelihood of a subhalo stream encounter is determined by simply summing the likelihood of the 4 individual observables.

Given that Scenario 1 features no observational errors on individual measurements, the observational error here is represented as the uncertainty in the mean of a Gaussian fit to the simulated particles in each bin, i.e. the shot noise associated with having a finite number of particles. Likewise, the stream track for both Scenario 2 and Scenario 3 also has data points representing a bin of multiple stars (17 data points in the track between −20° and 12°). Therefore, for every observable in Scenario 1, alongside the stream track for Scenario 2 and Scenario 3, the error in our simulated data is simply represented by the error in the mean for each bin. The radial velocities and proper motion data for both

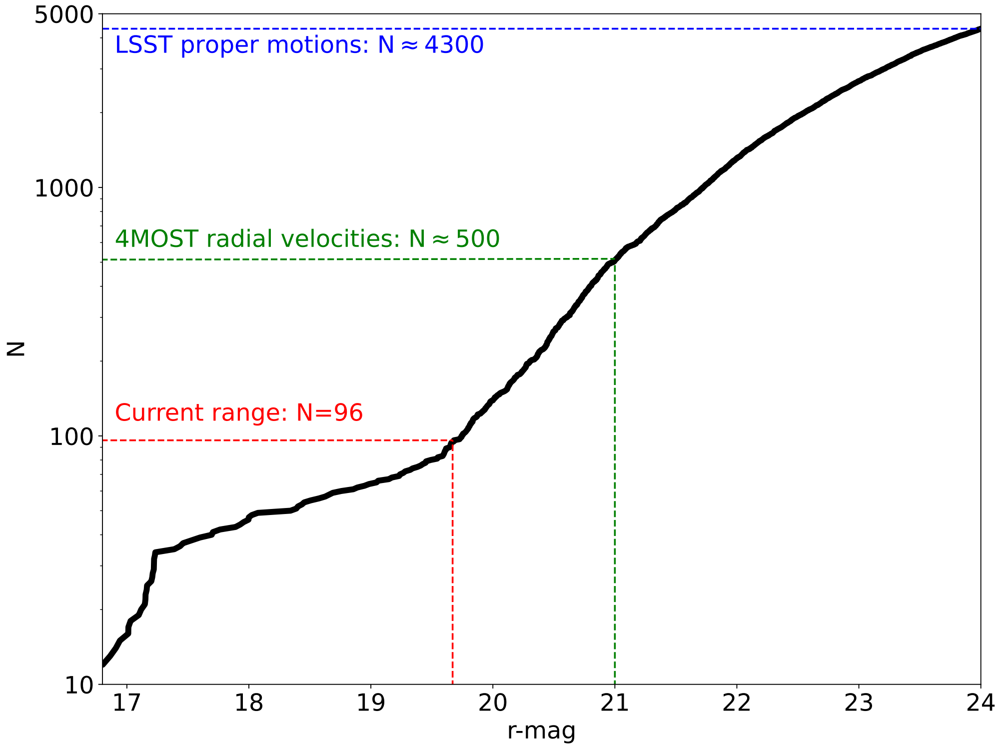

Figure 2.4: Estimates on the number of stars we would have data for as a function of magnitude. The current range described here shows the number of stars for which we have radial velocity and proper motion measurements in present-day AAU data, and we scale the IMF so that this luminosity function contains 96 stars in this range. The magnitude of stars that 4MOST and LSST will enable observations of are marked (21 mag for radial velocity measurements from 4MOST, and 24 mag for LSST proper motions), with the number of stars contained within the IMF in these ranges labeled. We note that we do not make use of LSST proper motions in our Scenario 3 fits and instead use proper motions expected from 10 years of *Gaia* data.

Scenario 2 and Scenario 3 meanwhile represent individual observations of stars. Here, the error in simulated data we use is instead the spread in the data of simulated stars about each bin.

2.4.3 A recent impact time

Our impact time for the mock uses a subhalo which encountered the stream fairly recently (250 Myr). The goal is to generate a stream with morphology similar to the AAU kink. We expect this flyby to apply velocity kicks to stars very close to each other along the track in ϕ_1. A small velocity perturbation, or an offset in distance modulus, would result in different orbital periods for these stars which would cause their position along the stream to change drastically over time as they drift from these original positions. As a result, we find that older encounters are not able to create a similar-looking mock stream to the AAU kink.

We test this using a simple approach of selecting a single stream particle approximately 2 Gyr after stream generation began. We duplicate this particle and apply a kick in one of this duplicate's velocity along the stream, $\mathrm{V_{tot}}$, the radial velocity relative to us, V_r, or a change in its distance modulus, $m - M$. The size of these are $20\,\mathrm{km\,s^{-1}}$ in velocities, and 0.3 in distance modulus. We then follow these two particles forward in the stream for 2 Gyr, shown in Figure 2.5. We can clearly see that shortly after roughly 0.6 Gyr, the particles are each separated by some tens of degrees, which would leave little trace of any feature especially any similar to a kink. While this is a qualitative look at the nature of the encounter, for the purpose of this work we assume this is the most plausible nature surrounding a subhalo-stream encounter that could produce streams with discontinuous morphology such as AAU. The high dimensionality of the space however could mean that further exploration has the potential to reveal different, older impacts that cause similar features.

2.5 MCMC Analysis

In order to explore how well the subhalo properties can be constrained, we use a Markov Chain Monte Carlo (MCMC) sampler to explore our likelihood space. The MCMC is a useful tool for intuitively exploring parameter space. Here, we use the Python library EMCEE (Foreman-Mackey et al., 2013) for our suite of MCMCs. For all of our runs, we use the same priors and they are summarised in Table 2.1.

These priors are based on previous works that modeled subhalo impacts (Yoon et al., 2011; Carlberg, 2012; Erkal et al., 2016). These priors are based on the expected distribution of the closest approaches of subhaloes, which are assumed to be uniformly distributed in position, with a line, which represents the stream (e.g. see Sec. 2 of Erkal et al., 2016).

We note that our prior of a Maxwellian distribution on our total velocity also serves to address the mass-velocity degeneracy that was encountered in Erkal & Belokurov (2015b). In their analytic work, they assumed the impulse approximation which means that the stream particle and subhalo are assumed to move on straight lines during the encounter. Furthermore, their model assumes that the velocity kicks are imparted instantaneously at the time of closest approach. In their model, the velocity kicks imparted by the subhalo are proportional to the subhalo mass divided by the flyby speed. Thus the mass and

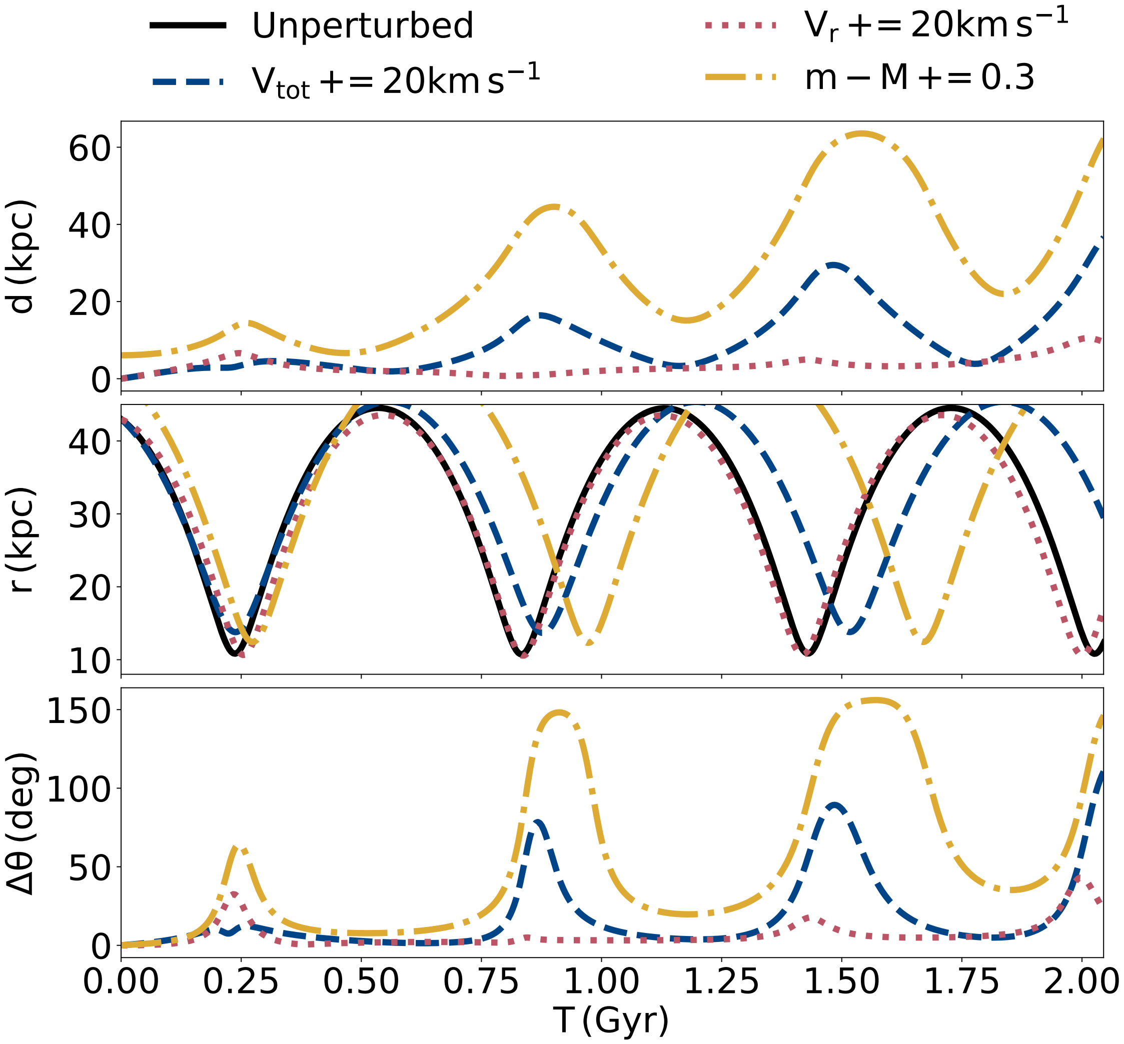

Figure 2.5: The evolution of particle positions for a total of 2 Gyr after applying a perturbation to a duplicate of a particle during stream generation. 3 different perturbations were applied individually here; Red: An increase in velocity along the stream of 20 km s^{-1}, Blue: An increase in the radial velocity in galactic coordinates of 20 km s^{-1}, Green: An increase in the distance modulus of 0.3. The panels are arranged as follows; Top: The distance between the perturbed and unperturbed particle, Middle: The galactocentric radius of both the perturbed and unperturbed particles, Bottom: The difference in sky positions between the perturbed and unperturbed particles.

Table 2.1: An overview of the parameters and priors for our MCMC setups. The descriptions of each parameter are covered in Section 2.3.2, however, here we represent the priors on $w_{\perp}$ and $w_{||}$ by the combined, total velocity of the subhalo $V_{\rm tot}$.

Parameter	Distribution	Prior
b	Uniform	$(0, \inf)$ kpc
α	Uniform	$(0, 360)$ deg
$V_{\rm tot}$	Maxwellian	$(168.2 \pm 97.1)\,{\rm km\,s^{-1}}$
$T_{\rm a}$	Uniform	$(0, 4)$ Gyr
$\phi_{\rm a}$	Uniform	$(-180, 180)$ deg
$M_{\rm sat}$	Uniform	$(0, \inf)\,M_{\odot}$
$rs_{\rm sat}$	Uniform	$(0, \inf)$ kpc

subhalo speed can be arbitrarily scaled and yield exactly the same result. A priori, it is unclear how strong this degeneracy should be in our more realistic setup since we include the subhalo as a particle orbiting in the host potential with the stream. This accounts for the actual orbit of a stream and the subhalo and also accounts for the fact that the acceleration of the subhalo on the stream is not instantaneous. This is especially important at lower relative velocities where the accelerations on stars would be experienced over a very significant period of time instead of instantaneously. Still, similar to their work we include a Maxwellian distribution applied to the total subhalo velocity. Here, we use a dispersion in the total subhalo velocity, σ, which relates to the circular velocity at 10 kpc, $v_{\rm circ}$, following the expression $\sigma = v_{\rm circ}/\sqrt{3}$. This results in $\sigma = 97.1, {\rm km\,s^{-1}}$.

Next, we present the MCMC results for all 3 data quality scenarios. For every scenario, our results shown involve an MCMC using 100 walkers, and we burn-in 1/2 of all steps.

2.5.1 Scenario 1: Fits with no observational errors

First, we consider our approach with no additional observational errors. We evolved our MCMC for 38,370 MCMC steps and show the results in Figure 2.6. The autocorrelation times are ∼600 for each variable, so this number of steps was sufficient to reach more than 50 autocorrelation times. For every panel, the true parameters were recovered within at least 2 sigma, which shows that the parameters could be inferred well for Scenario 1. The likelihood peaks in the figure do not coincide exactly with the true values. This is expected since our mock measurements have been sampled using their respective errors as explained in Section 2.4.1.

We note that some of the correlations in Figure 2.6 are elongated showing some slight degeneracies exist. When comparing either velocities, w, with $M_{\rm sat}$, this is fairly evident, where the high likelihood solutions are stretched along $M_{\rm sat} \propto w$. This degeneracy was present in Erkal & Belokurov (2015a) as an unbroken degeneracy, i.e. arbitrary rescalings of w and $M_{\rm sat}$ led to exactly the same gap. We note that in our setup this degeneracy is broken by the fact that we do not make an impulse approximation and instead integrate the subhalo in the host potential along with the stream. In addition, we do have a prior on the velocity although this prior is much weaker than the constraints shown in Figure 2.6. There is also a similar feature between $T_{\rm a}$ and $\phi_{\rm a}$. This weak degeneracy arises due to the fact the stream is on an eccentric orbit and thus stretches and compresses as it orbits the Milky Way. As a result, if the impact time is slightly later or earlier, the subhalo impact point along the stream will have to be moved slightly to have the same present-day location of the kink.

2.5.2 Scenario 2: Fits using current observational uncertainties

Next, we show the results of Scenario 2 with its present-day observational uncertainties. The resulting chains are shown in Figure 2.7. In this case, we run our MCMC for 61,142 steps. We note that despite this large number of steps, since the largest autocorrelation times are roughly 2,000, this does not reach the target of 50 times the autocorrelation times. In general, the parameters were still well recovered, with most being within 2 sigma of their true values once again. Similar to Scenario 1, the velocity with mass panels alongside the impact time with angle along the stream exhibit faint hints of degeneracies present. However, in the latter case, this is still not much more significant than Scenario 1 in Figure 2.6.

The recovery of $\mathrm{w}_\perp$ and $\mathrm{M}_{\mathrm{sat}}$ was not as successful, where the true value for the mock was over 3 sigma off the results. Since these parameters are strongly correlated and the true values of $\mathrm{w}_\perp$ and $\mathrm{M}_{\mathrm{sat}}$ lie along the correlation, this is likely a result of both the degeneracies between mass and velocity combined with our priors and the larger volume in parameter space at higher velocities. The true impact parameters do give a lower velocity than the predicted circular velocity from our Maxwelian distribution, and this would result in their likelihood being disfavoured slightly compared to high-velocity encounters. It is possible even excluding this prior, these higher velocities and masses still give very similar likelihoods compared to the true impact.

2.5.3 Scenario 3: Fits using future observational uncertainties

Finally, we consider our future error scenario. Here, our chains are run for a total of 85,140 steps with the posteriors shown in Figure 2.8. As with Scenario 2, this is lower than the target of having steps equal to 50 times the autocorrelation times, which in this instance were on average roughly 5,000 as well. The parameters are still well recovered, with most being within 2 sigma of their true values. Compared to Scenario 2, the recovered parameters are closer to the true values and the uncertainties are significantly smaller. We also note the same degeneracies that were seen in both previous error scenarios, albeit with a significantly smaller uncertainty compared to Scenario 2.

We note that both the subhalo mass and the speed of the subhalo are underestimated. As in Scenario 2, this is likely due to a partial degeneracy between the mass and speed of a subhalo, combined with our prior and the larger volume in our parameter space at higher speeds. In addition, while the impact time T_a is still recovered, there is an interesting asymmetry in the posterior. The correlation between T_a and ϕ_a is more significant compared to Scenario 1 and 2 which appears to be driving this distribution. We also note that while the inferred parameters in Scenario 3 appear to have a lot of noise compared to Scenario 2 (e.g. compare Fig. 2.8 and 2.7), the ranges of all of the parameters are significantly smaller so the parameters are recovered with a much higher precision.

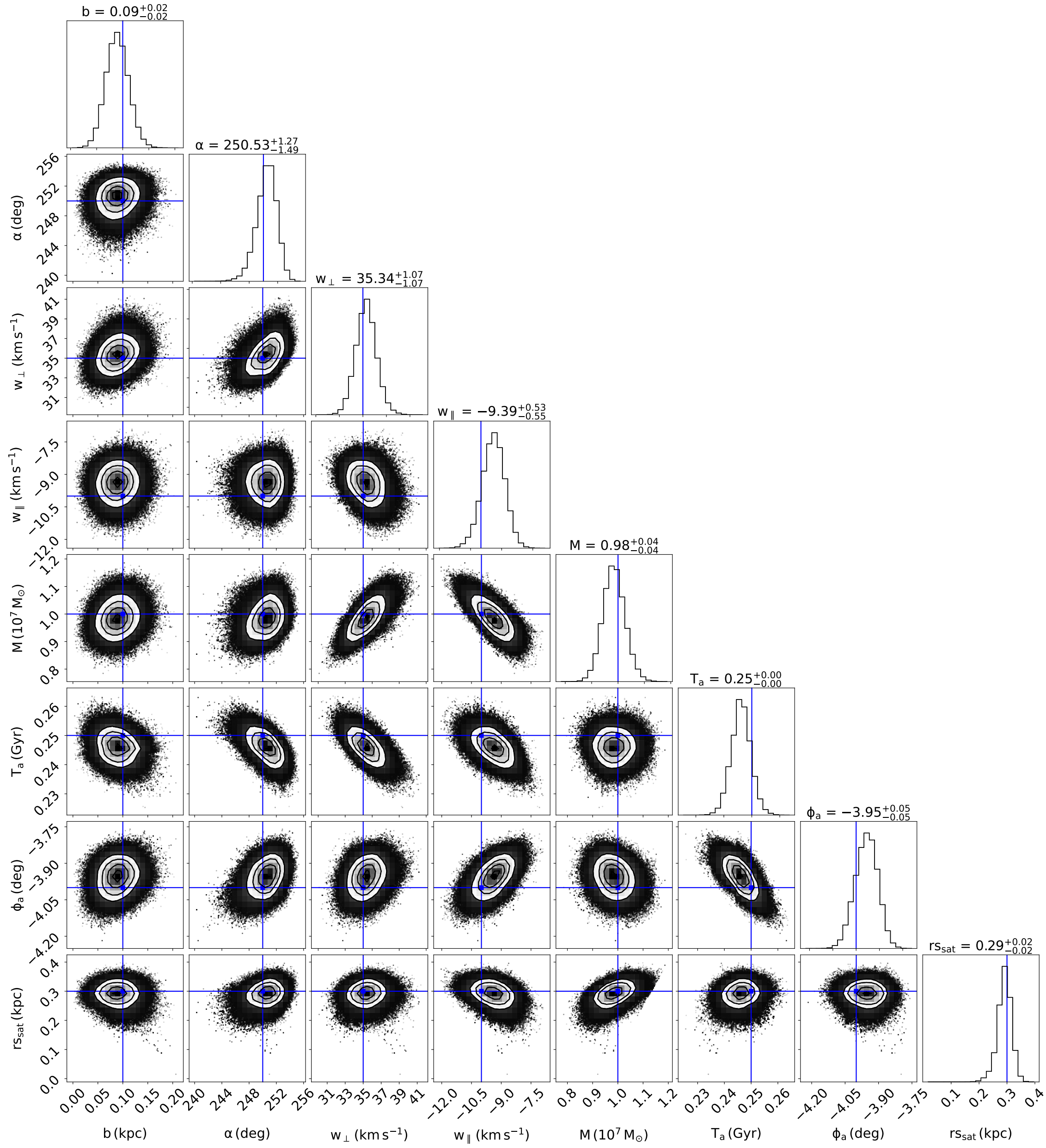

Figure 2.6: Corner plot of ∼40,000 steps of our MCMC in the scenario using no observational errors. The results here are shown after burning half of the steps. All 8 impact parameters are shown, as summarised in Section 2.3.2, with their corresponding 1d histograms along the top of the plot. The contour lines here represent the 3 sigma levels of the steps

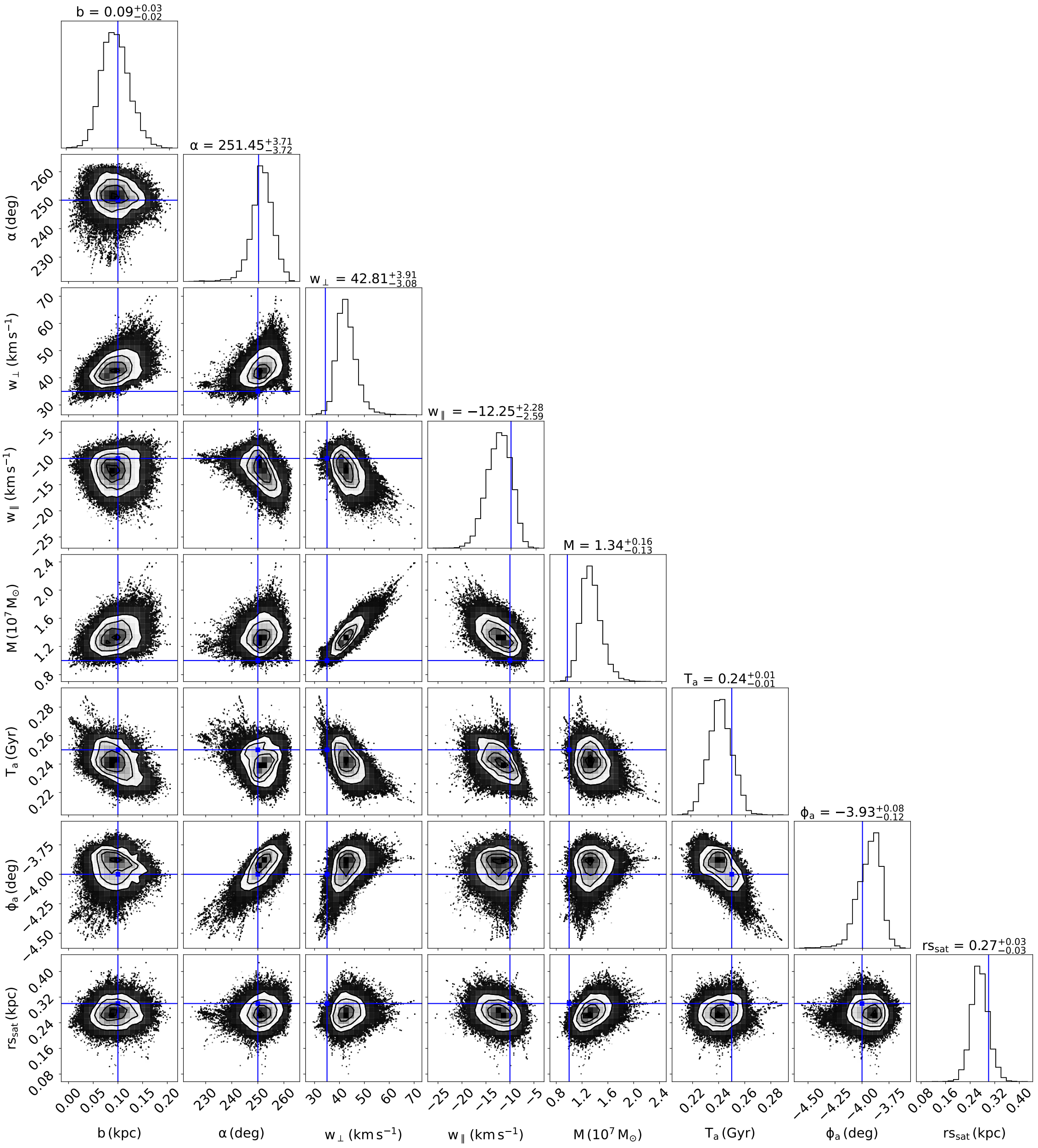

Figure 2.7: Corner plot of 60000 steps of our MCMC in the scenario using present-day observational errors. The results here are shown after burning half of the steps. All 8 impact parameters are shown, as summarised in Section 2.3.2, with their corresponding 1d histograms along the top of the plot. The contour lines here represent the 3 sigma levels of the steps

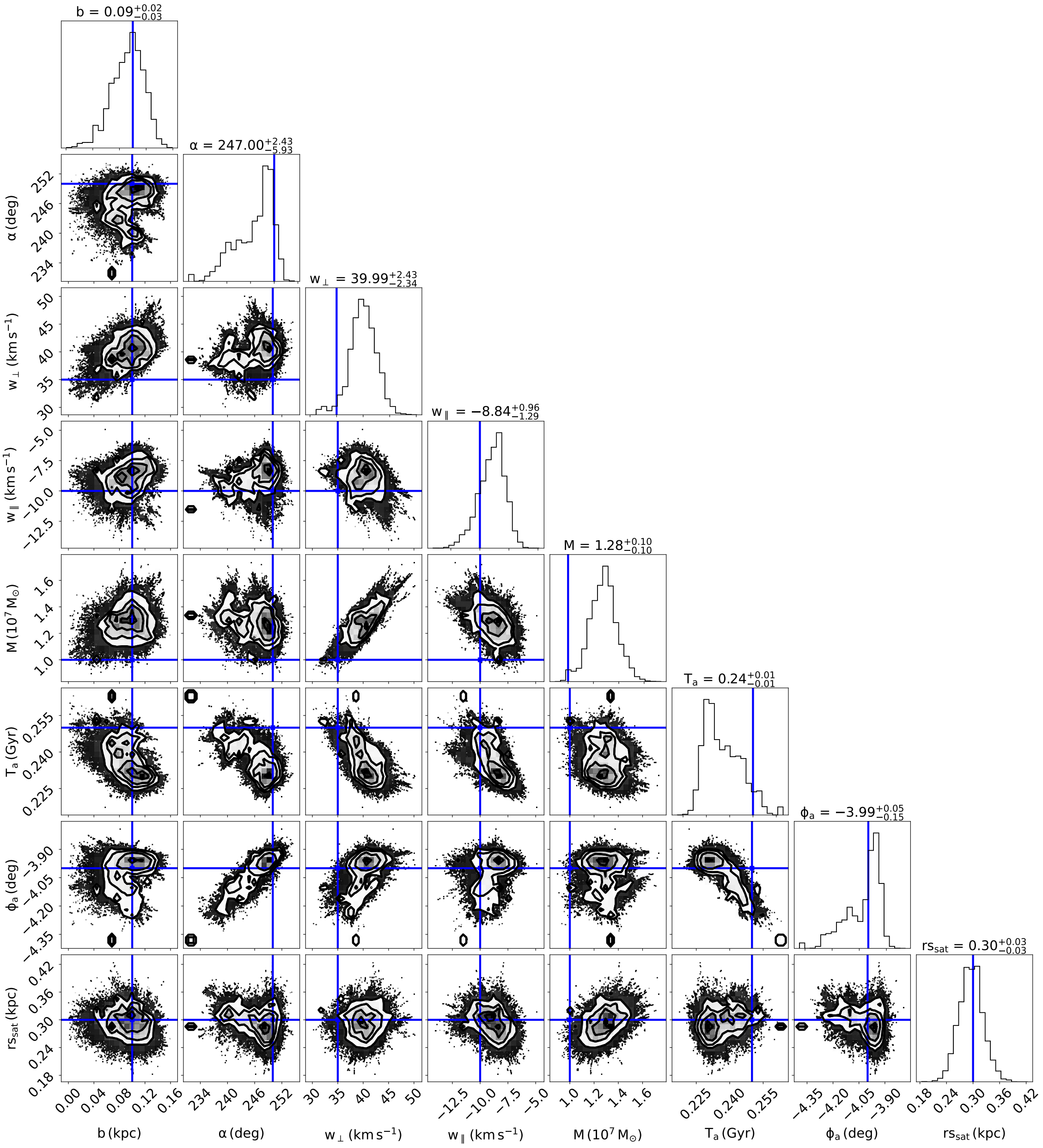

Figure 2.8: The recovery of the mass and scale radius of the subhalo for each of the 3 error scenarios. Yellow: No observational errors, Blue: Present-day observational errors, Red: Future predicted observational errors. The contours for each scenario showcase the 3 sigma levels, and the scatter shows the full range of parameters explored after burning half of all steps. The true mass and scale radius values for the mock impact are shown in black

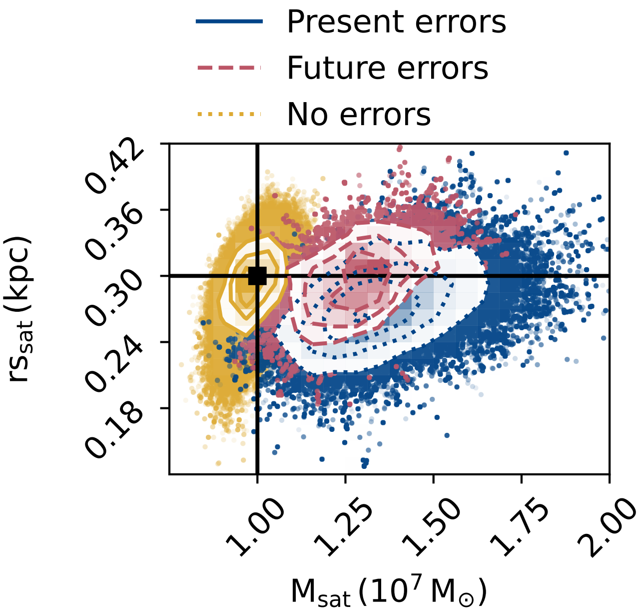

Figure 2.9: The recovery of the mass and scale radius of the subhalo for each of the 3 error scenarios. Yellow: No observational errors, Blue: Present-day observational errors, Red: Future predicted observational errors. The contours for each scenario showcase the 3 sigma levels, and the scatter shows the full range of parameters explored after burning half of all steps. The true mass and scale radius values for the mock impact are shown in black.

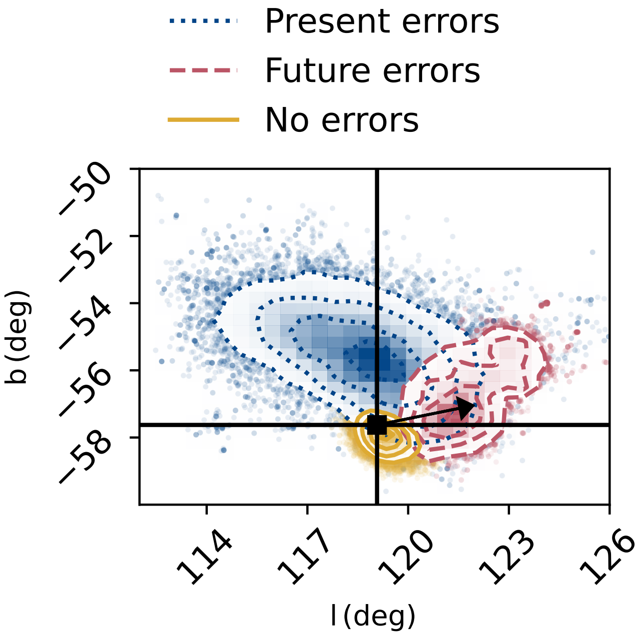

Figure 2.10: The recovery of the sky positions of the subhalo in the present day for 2500 randomly sampled MCMC runs for all 3 scenarios. Yellow: No observational errors, Blue: Present-day observational errors, Red: Future predicted observational errors. The contour levels represent the sigma levels for all 2500 steps, and the scatter shows the full range of possible subhalo positions from the subhalo-stream encounters used. The subhalo position of the mock impact is shown in black, with its direction of orbit also shown.

2.6 Discussion

2.6.1 Subhalo Localisation

Given that the fits can reliably determine the subhalo properties at impact, we explore how well they can localize the subhalo at the present day. For each error scenario, we randomly chose 25000 encounters from the MCMC samples after burn-in of 1/2 to follow their orbits during and after the encounter. Specifically, we obtained the subhalo positions at t = 0, mimicking their expected locations on the present day. In Figure 2.10 we show how well the sky positions of the subhalo can be constrained for each scenario, additionally showing the position and motion of the mock subhalo. This is also shown in galactocentric coordinates in Figure 2.14. Even for the largest errors of Scenario 2, we can expect a relatively tight constraint on its location, which shows great potential for future fits on real observational data. This relatively small area covered will be in part due to the recent impact time, where differences in subhalo velocity between fits will only translate to a minor change in present-day sky positions. Future fits on streams, particularly if the impact time was many orbital periods ago, could show a far broader range in present-day subhalo positions.

If the subhalo's present-day position is well-localized, this can help with searching for possible baryonic perturbers. For example, globular clusters and dwarf galaxies can also perturb stellar streams and the subhalo's present-day position could be compared with known objects. Similarly, the subhalo's present-day location could be compared with maps of gamma-ray emission to each for possible evidence of dark matter annihilation or decay (e.g. Mirabal & Bonaca, 2021).

2.6.2 Information content of perturbed streams

In this work, we have shown that the properties of the impacting subhalo (i.e. its mass, scale radius, impact position and velocity, and impact time) can be recovered from observations of a perturbed stellar stream. Previously, Erkal & Belokurov (2015b) had shown similar results for streams on circular orbits. In that work, they used an analytic model for a perturbed stream which assumed that the stream was a train of particles on the same (circular) orbit. In addition, they also assumed that the subhalo impact was impulsive, i.e. that the stream and subhalo moved on straight lines during the encounter. In that work, they explored the information content of the observations and showed that all parameters describing the subhalo's encounter with the stream could be recovered up to a degeneracy between the subhalo mass and its velocity relative to the stream. As shown in Section 2.5.1, this degeneracy is not as prevalent in our work since we do not assume the impulse approximation and instead inject the subhalo on its orbit. We note that Bonaca et al. (2019) also found a similar result in their fits to the GD-1 stream.

Another relevant result of Erkal & Belokurov (2015b) is that they proved that the subhalo parameters could be extracted using measurements of only three stream observables, e.g. stream track on the sky, radial velocity, and one proper motion. In this work, we used four observables (stream track, radial velocity, and two proper motions) and were able to get robust measurements of all the subhalo properties. This is similar to the setup discussed in Section 5.3.3 of Erkal & Belokurov (2015b) which emphasized that the subhalo properties can be inferred without any density information. This is a useful approach since it does not require that we understand the disruption history of the globular cluster progenitor which can affect the density profile (e.g. Gieles et al., 2021). Thus, the results of this work show that the intuition from Erkal & Belokurov (2015b) should extend to realistic streams on eccentric orbits.

2.7 Conclusions

In this work, we have explored how well the properties of subhaloes can be recovered from observations of stellar streams in a realistic setup. Using synthetic data sets with different amounts of errors, we modeled subhalo-stream encounters in a Bayesian framework and inferred how well we can constrain the properties of these encounters in numerical simulations. We first modeled these setups and described the encounters using 8 key parameters. Then, we focused on generating perturbed streams with similar morphology to the kink in the AAU stream and did so by running a perturbation featuring an almost direct impact of a $10^7\,\mathrm{M}_\odot$ subhalo onto the stream. We summarise our conclusions below:

- While a stream morphology similar to the AAU kink can be reproduced by subhalo-stream encounters, including producing $\sim$ 10 km/s velocity differences across the kink, these encounters appear to require very recent impacts. This is due to the rate at which particles drift apart after receiving a kick in velocity or distance modulus, which would very rapidly drift apart tens of degrees after $\sim$ 0.6 Gyr and leave little trace of any feature.

- In instances where we have effectively no observational errors, we can accurately recover the full suite of 8 impact parameters defining the encounter. This gives us full dynamical data of the subhalo relative to the stream, as these include not only the velocities but also where and when the encounter took place. In addition, we can recover the subhalo mass and scale radius.

- If we include realistic observational uncertainties, there usually are difficulties recovering the velocities of the subhalo and its mass. This is in part due to the mass velocity degeneracy still partially present even in numerical simulations. Still, these tend to be recovered within 3 standard deviations for the worst cases and shows promise in breaking this often encountered degeneracy in previous works (e.g. Erkal & Belokurov, 2015b).

- The recovery above is only minimally reduced by improving the observational errors and adding to the abundance of data as well, and in the case of some other parameters, there is no improvement at all to the recovery. Still, for these other parameters, both maintain a recovery within one standard deviation just like the no-error scenario.

- Of the properties, the mass and scale radius carry a lot of future potential if this could be applied to fitting real streams. These two parameters can be used to test how well the properties of low-mass dark matter subhaloes compare with predictions from cosmological simulations with cold dark matter and alternative dark matter models.

- Regardless of the quality of the observables, we find that we can constrain the present-day sky positions of the subhalo within 10 deg for this recent impact. We can use this for real impacts to perform observations in this region for any luminous objects that may fit the properties of our subhalo, to search for possibly baryonic perturbers, and to search for possible gamma-ray signatures of dark matter annihilation.

The results of this work suggest that it should be possible to use perturbations like those present in AAU to measure the perturber which created them. Furthermore, such fits should already be possible with current observational uncertainties and these fits should improve in precision with upcoming data from surveys like 4MOST and further *Gaia* data releases. As more perturbed streams are observed, fits like these will allow us to build a census of perturbers in the Milky Way. While some of these may be due to baryonic substructure, e.g. due to a dwarf galaxy, some will hopefully have no baryonic culprit and will instead allow us to build an inventory of dark matter subhaloes in the Milky Way.

2.8 Acknowledgements

DE acknowledges support through ARC DP210100855. SK acknowledges support from the Science & Technology Facilities Council (STFC) grant ST/Y001001/1. T.S.L. acknowledges financial support from Natural Sciences and Engineering Research Council of Canada (NSERC) through grant RGPIN-2022-04794. A.P.J. acknowledges support by the National Science Foundation under grants AST-2206264 and AST-2307599. DZ and GFL acknowledge support from the Australian Research Council Discovery Project DP220102254. N.S. is supported by an NSF Astronomy and Astrophysics Postdoctoral Fellowship under award AST-2303841. G.L. acknowledges FAPESP (Proc. 2021/10429-0).

2.9 Data Availability

The models and chains in this work will be made available upon reasonable request to the corresponding author.

Appendix: Mock observables

In this appendix, we show mock observations of our simulated stream in three different observational setups. Figure 2.12 shows mock observations with no additional observational uncertainties, i.e. the uncertainties come from the Poisson uncertainties associated with the finite number of particles in our mock stream. Figure 2.12 shows the mock observations of our simulated stream assuming present-day errors and Figure 2.13 shows the mock observations of our simulated stream assuming future observational errors, i.e. with the proper motion uncertainties assuming 10 years of data from *Gaia* and with the expected radial velocity uncertainty and depth from 4MOST.

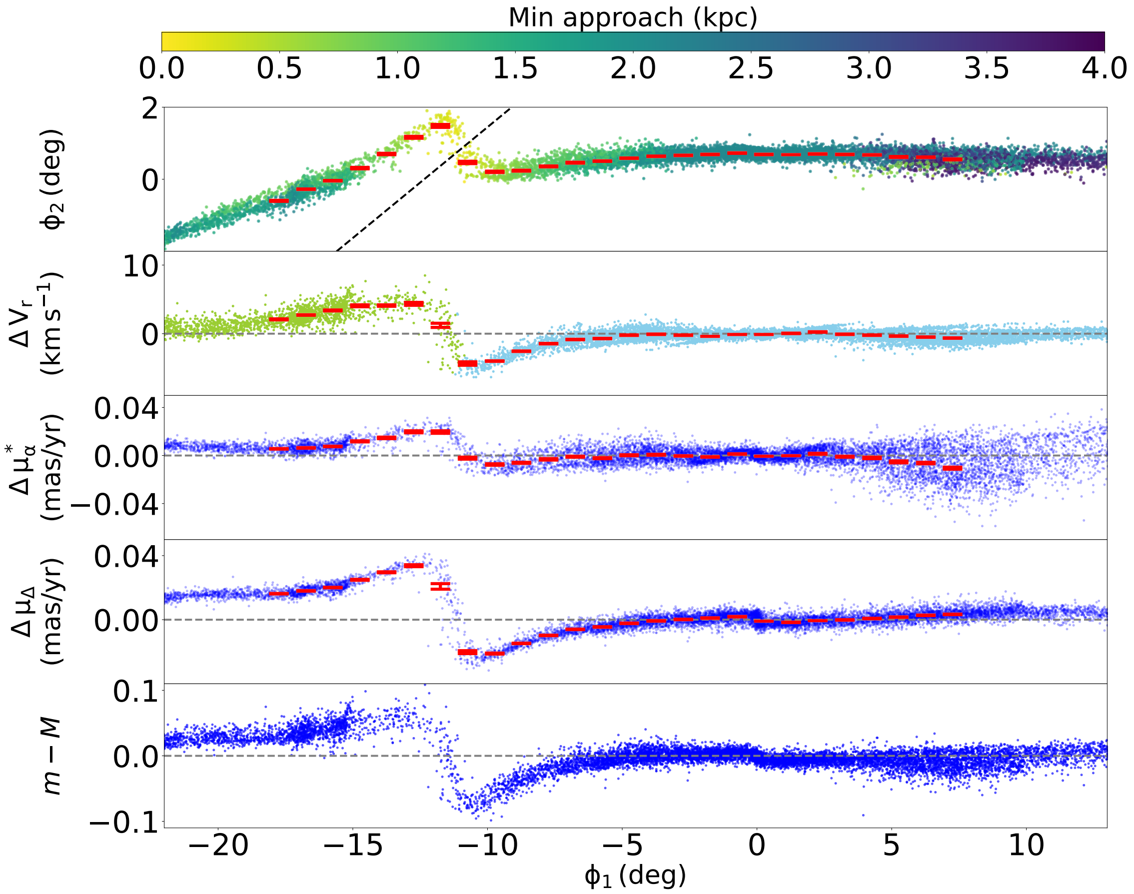

Figure 2.11: The data of our mock perturbed stream with no observational errors, errorbars instead showing the spread in 1 deg bins in ϕ_1. An exception is made in the stream track, as explained in Section 2.4.1 where we inflate the error to account for minor variations in the random seed. Top: Stream track, with the minimum distance achieved between individual mock stream stars and the subhalo shown in the colour bar. The black data points highlight the radial velocity and proper motions of stars in the panels below. We also show a dotted line that separates the observed stars as belonging to either the ATLAS half of the stream (right of the kink) or the Aliqa Uma half (left of the kink). Second row: The radial velocity differences between the mock perturbed stream and a fourth-order polynomial fit of V_{GSR} for the unperturbed model, with mock observables shown as red error bars. The stars belonging to the ATLAS part of the stream are shown in light blue and Aliqa Uma in green. Third and fourth row: The proper motion differences between the perturbed stream and a fourth-order polynomial fit, with mock observables shown once again as red error bars, much in the same vein as the radial velocities. Bottom row: Distance modulus difference between the perturbed stream and a fifth-order polynomial fit to the unperturbed model.

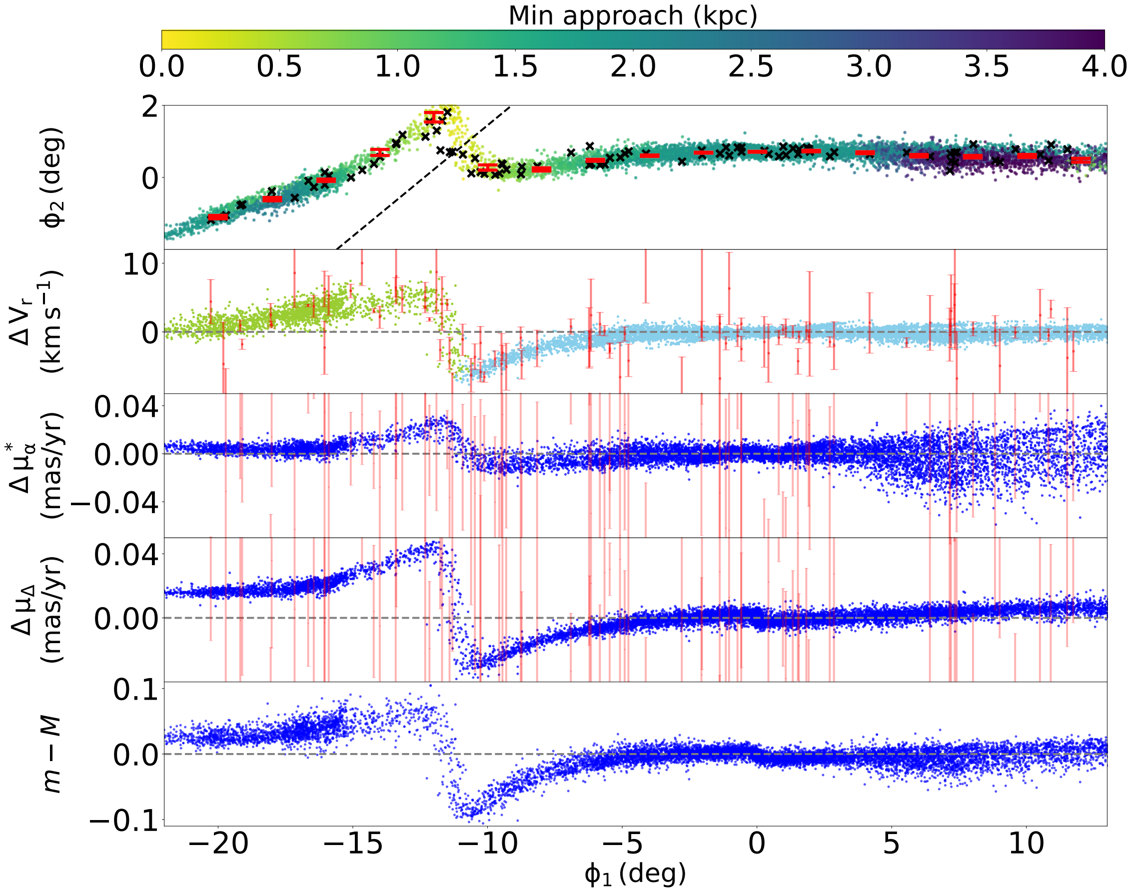

Figure 2.12: The data of our mock perturbed stream with data following present-day errors overlaid. Top: Stream track, with the minimum distance achieved between individual mock stream stars and the subhalo shown in the colour bar. The black data points highlight the radial velocity and proper motions of stars in the panels below. We also show a dotted line that separates the observed stars as belonging to either the ATLAS half of the stream (right of the kink) or the Aliqa Uma half (left of the kink). Second row: The radial velocity differences between the mock perturbed stream and a fourth-order polynomial fit of V_{GSR} for the unperturbed model, with mock observables shown as red error bars. The stars belonging to the ATLAS part of the stream are shown in light blue, and Aliqa Uma in green. Third and fourth row: The proper motion differences between the perturbed stream and a fourth-order polynomial fit, with mock observables shown once again as red error bars, much in the same vein as the radial velocities. Bottom row: Distance modulus difference between the perturbed stream and a fifth-order polynomial fit to the unperturbed model.

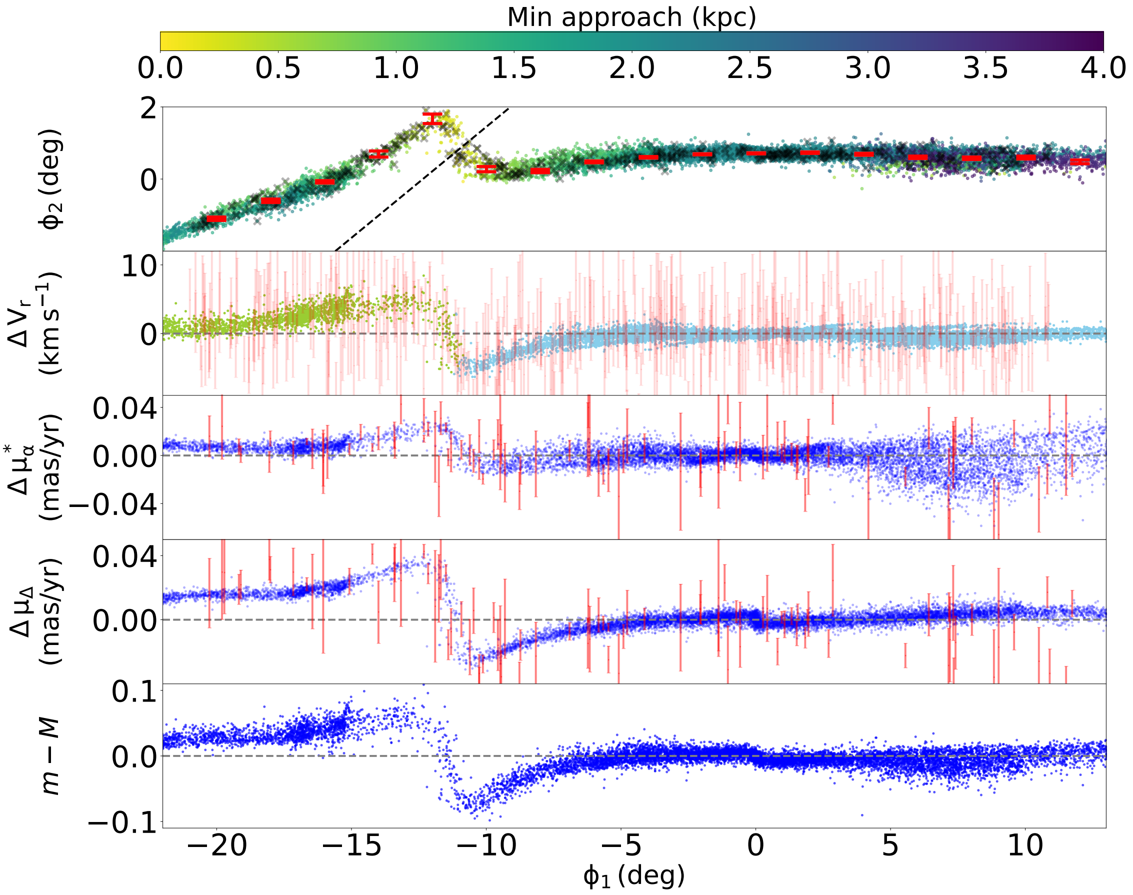

Figure 2.13: The data of our mock perturbed stream with data following future predicted errors overlaid. Top: Stream track, with the minimum distance achieved between individual mock stream stars and the subhalo shown in the colour bar. The black data points highlight the radial velocity and proper motions of stars in the panels below. We also show a dotted line that separates the observed stars as belonging to either the ATLAS half of the stream (right of the kink) or the Aliqa Uma half (left of the kink). Second row: The radial velocity differences between the mock perturbed stream and a fourth-order polynomial fit of V_{GSR} for the unperturbed model, with mock observables shown as red error bars. The stars belonging to the ATLAS part of the stream are shown in light blue and Aliqa Uma in green. Third and fourth row: The proper motion differences between the perturbed stream and a fourth-order polynomial fit, with mock observables shown once again as red error bars, much in the same vein as the radial velocities. Bottom row: Distance modulus difference between the perturbed stream and a fifth-order polynomial fit to the unperturbed model.

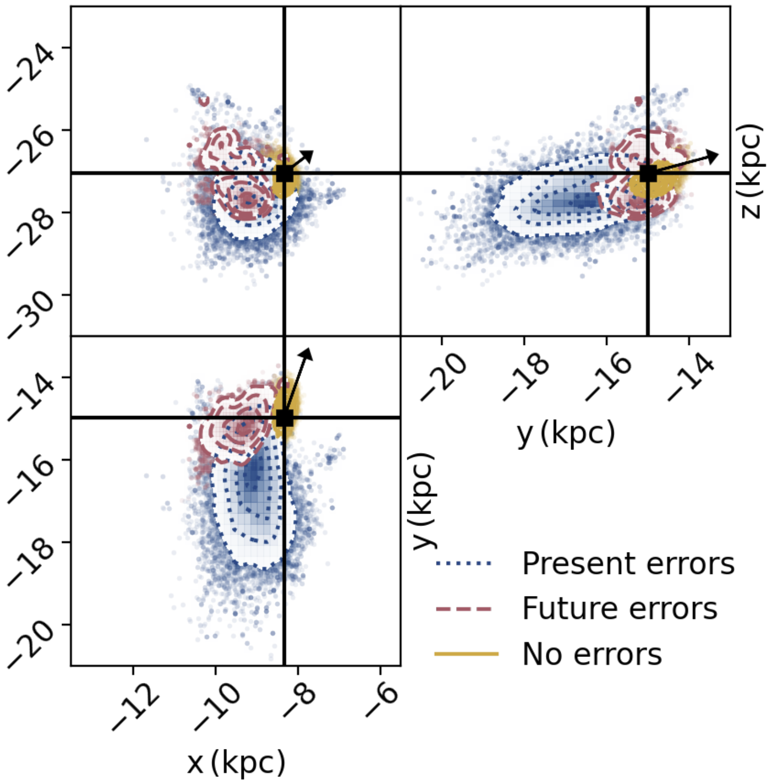

Figure 2.14: The recovery of the subhalo in the present day for 2500 randomly sampled MCMC runs for all 3 scenarios, with the positions shown in galactocentric coordinates. Yellow: No observational errors, Blue: Present-day observational errors, Red: Future predicted observational errors. The contour levels represent the sigma levels for all 2500 steps, and the scatter shows the full range of possible subhalo positions from the subhalo-stream encounters used. The subhalo position of the mock impact is shown in black, with its direction of orbit also shown.

Chapter 3

Measuring the properties of a Milky Way subhalo with the ATLAS-Aliqa Uma stream

In the previous Chapter, I showed that it was possible to measure the properties of a subhalo using mock observations of the AAU stream with present-day observational uncertainties. The goal of this chapter is to now fit the real AAU data and try to measure the properties of a subhalo which can reproduce the observations, as the subhalo properties could make for a very important result towards constraining the dark matter particle. As part of this, I show a new sample of data taken by the S5 survey since the publication of Li et al. (2021), which changes the morphology of the kink. In order to do these fits, I also outline a new approach to likelihood estimation to best fit the subhalo-stream encounters to the kink.

3.0.1 Advances in AAU observations

Our understanding of the AAU stream has evolved significantly compared to when it was first detected. In Shipp et al. (2018), the ATLAS and Aliqa Uma streams were originally presented as two independent streams since they appeared disconnected on the sky. Follow-up spectroscopic observations from Li et al. (2021) showed that ATLAS and Aliqa Uma had consistent kinematics (i.e. radial velocities and proper motions) and also that the structures appeared to be connected. Observations showed a kink feature which would join the ATLAS stream and Aliqa Uma stream. Since Li et al. (2021), additional data has been taken by the S5 survey which has not been presented anywhere to date. In Figure 3.1 we show the likely members to the AAU stream, where the sky fields used to observe the stream now cover a broader range both perpendicular to the stream in ϕ_2 and especially along the stream in ϕ_1. The selection criteria for this new data is unchanged from Li et al. (2021) and more details on this can be found within.

Particularly for the kink, the new observations make this feature a great deal more complex than originally thought. Originally, both the ATLAS half, Aliqa Uma half and the kink appeared to form a continuous track. In Chapter 2, Figure 2.3 demonstrates both how the older AAU data appeared that way, and how we treated the mocks accordingly. The mock perturbation was generated to be one continuous track with a kink across, and we would

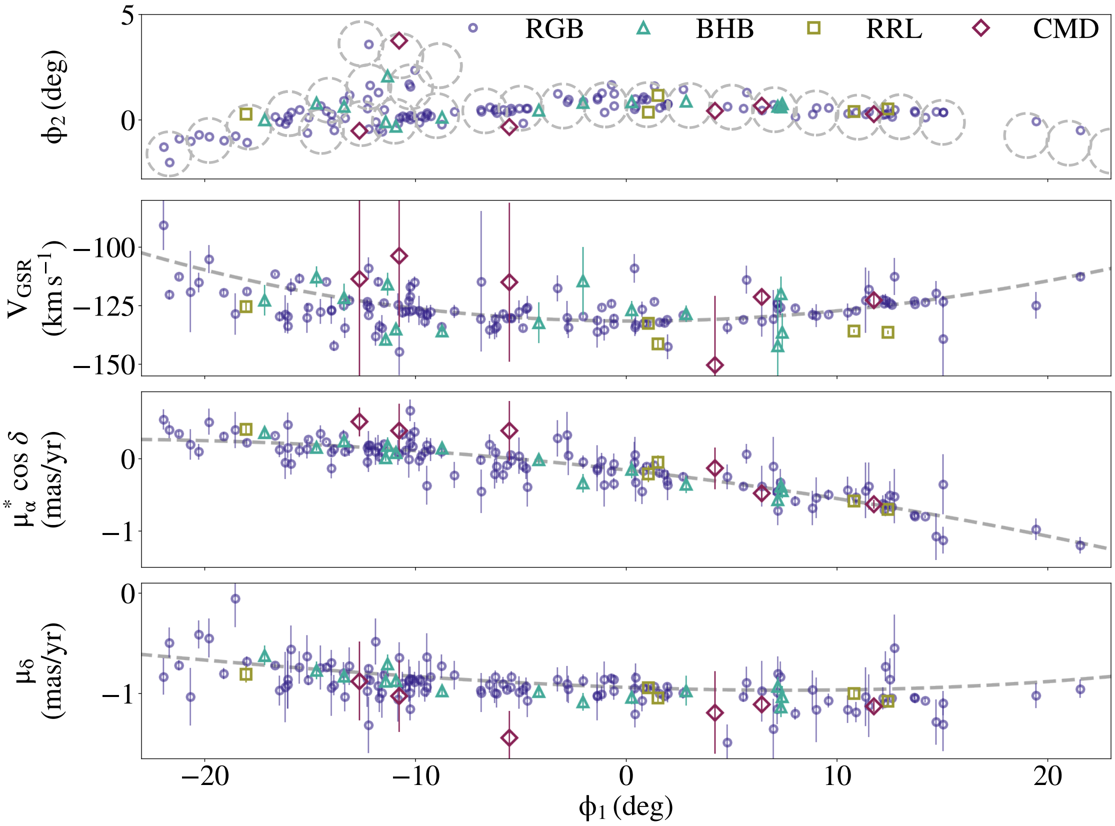

Figure 3.1: The most recent obervations performed on the AAU stream, showcasing the additional data present around the kink and the spectroscopic members that make up the stream. These consist of Red Giant Branch (RGB), Blue Horizontal Branch (BHB), RR-Lyrae (RRL) stars, along with some identified on a colour-magnitude diagram which are not members of any above group (CMD). The top panel represents the stream track, the same rotated coordinate system as in our mock impact in Chapter 2. Here, all the fields where we have performed observations are shown in the dashed grey circles as well. The bottom panels show the kinematics of the stream, consisting of the velocities at the Galactic Standard of Rest, v_{GSR}, alongside the proper motions. We show polynomial fits to the bottom 3 panels by fitting to an unperturbed stream initially used to fit the ATLAS track of the AAU stream, which is the same progenitor used for our fits in Chapter 2 along with the fits to follow in this section.

separate the two halves of the stream at the kink. While the ATLAS and Aliqa-Uma parts of the stream still appear unperturbed, the kink itself now has a longer extension of the ATLAS half of the stream which effectively goes beneath the Aliqa-Uma half. Is is difficult to tell which part of the stream these belong to, and it is likely in the kink region we cannot reliably define stars as belonging to either ATLAS or Aliqa-Uma any more. The radial velocities and proper motions meanwhile show a similar trend to the what was previously seen by Li et al. (2021).

3.1 Changes to the encounter setup

The process of running subhalo-stream interactions uses largely the same method as in Chapter 2. We do however, make a few minor changes to the stream generation and subhalo properties, along with some quite significant changes to the likelihood estimation.

First, we modified the stream generation and encounter process to better fit the properties of the AAU stream itself, along with the shape of the kink compared to our mock kink from before. Due to the velocity dispersion along the AAU track on average being greater than past fits in Li et al. (2021) and Chapter 2, we elected to use a higher progenitor mass of $8 \times 10^4 \mathrm{M}_\odot$. The resulting stream is thicker along ϕ_2 compared to these past fits, and more closely matches the radial velocity dispersion seen in the AAU data.

We also modify the subhalo to use a Hernquist profile over the formerly used Plummer Sphere as well. The Hernquist profile is cusp versus the core of the Plummer sphere which makes for more realistic subhaloes. This carries an additional effect at distances beyond the scale radius of the subhalo, as the density dropoff is $\rho \propto \mathrm{r}^{-5}$ for the Plummer model and $\rho \propto \mathrm{r}^{-4}$ for the Hernquist profile. This results in our fits using slightly less compact subhaloes beyond the scale radius than in Chapter 2.

3.2 Fitting the perturbed stream

Similar to in Chapter 2, we estimate the likelihood for most of the 4 observable parameters using the standard equation below:

$$\ln \mathcal{L} = \sum_{\mathrm{i}} \left(\ln \left(\frac{1}{\sqrt{2\pi\sigma_{\mathrm{i}}^2}} \right) - \frac{(\mathrm{o_i} - \mathrm{m_i})^2}{2\sigma_{\mathrm{i}}^2} \right) \tag{3.1}$$

Once again, i denotes the bin in ϕ_1 along the stream, $\mathrm{o_i}$ represents the centroid for the simulated data with σ_i its error, and $\mathrm{m_i}$ representing the centroid for the model mock data. This is carried out on the 4 observables, which are the stream track $\phi2$, radial velocities $\Delta\,\mathrm{V_r}$, and 2 proper motions μ_α^* and μ_δ. Likewise we follow Erkal & Belokurov (2015b) in the same manner, where we assume that these 4 observables are independent, so total log likelihood of a subhalo stream encounter is determined by simply summing the 4 individual observables.

With the nature of the data here already being similar to a scenario covered in that work, we once again analyse the radial velocities and proper motions as individual stars, over the spline fitting used for the sky positions. We do, however, make some considerable changes to the way we compute the likelihood in the vicinity of the kink, which is further discussed in Section 3.2.2. We define this kink region in ϕ_1 as $-15.5\,\mathrm{deg} \leq \phi_1 \leq -7.8\,\mathrm{deg}$. This region is chosen as it covers where the ATLAS and Aliqa Uma streams overlap and it is no longer possible to distinguish which stars belong to which portions of the stream.

3.2.1 Restriction of the simulated data

Our first major change is how we treat and compare the the observables to the simulated data. In Chapter 2, we binned only in ϕ_1 when comparing data. The exception to this was splitting the data in ϕ_2 along a line we drew to separate stars above and below the kink. We no longer use this approach due to the complex morphology observed in AAU. Instead, within the range defined above, we restrict model stars used for analysis to circular fields corresponding to the real fields we used for observations of AAU. These fields are shown in Figure 3.1, though because the stream is relatively unperturbed outside the kink we keep the prior method of using the full range of model data within the 1 deg bin in ϕ_1. We elect to take this approach since we only have observations of the stream within these fields. By using these fields, we restrict our simulated stream to be observed in the same patches of the sky.

3.2.2 Modifications to the likelihood

Given the complex morphology of the stars in the new AAU data in Figure 3.1, we no longer make the prior assumption that the the streams sky location is simply a function of its angle along the stream. As a result, we no longer use the standard likelihood function within the kink to allow the stream density to be a function of ϕ_1 and ϕ_2. Now we employ a Kernel Density Estimation (KDE) for both the track and the radial velocities, applying this to individual observed stars along the kink instead of the spline fittings that were previously used along the track. Below, we show how we approach the KDE in order deliver a more reliable likelihood estimation for the AAU kink.

Kernel Density Estimates about the kink

Kernel density estimation is a technique for getting a smoothed probability density estimation from a discrete sample. For the purpose of the fits described here, we take a KDE approach to describe the probability distribution of the model stream and then evaluate the likelihood of the observed stars given this model. We use a similar approach with determining likelihoods using a KDE for both the track and the radial velocities.

We determine the probability density function $\mathrm{P}(\phi_2|\phi_{1,\mathrm{fields}})$ and $\mathrm{P}(\mathrm{V_r}|\phi_1^{\mathrm{fields}}, \phi_2)$ through the following equations

$$\mathrm{P}(\phi_2|\phi_1^{\mathrm{fields}}) = \mathrm{P}(\phi_2, \phi_1^{\mathrm{fields}})/\mathrm{P}(\phi_1^{\mathrm{fields}}) \tag{3.2}$$

$$\mathrm{P}(\mathrm{V_r}|\phi_1^{\mathrm{fields}}, \phi_2) = \mathrm{P}(\mathrm{V_r}, \phi_1^{\mathrm{fields}}, \phi_2)/\mathrm{P}(\phi_1^{\mathrm{fields}}, \phi_2) \tag{3.3}$$

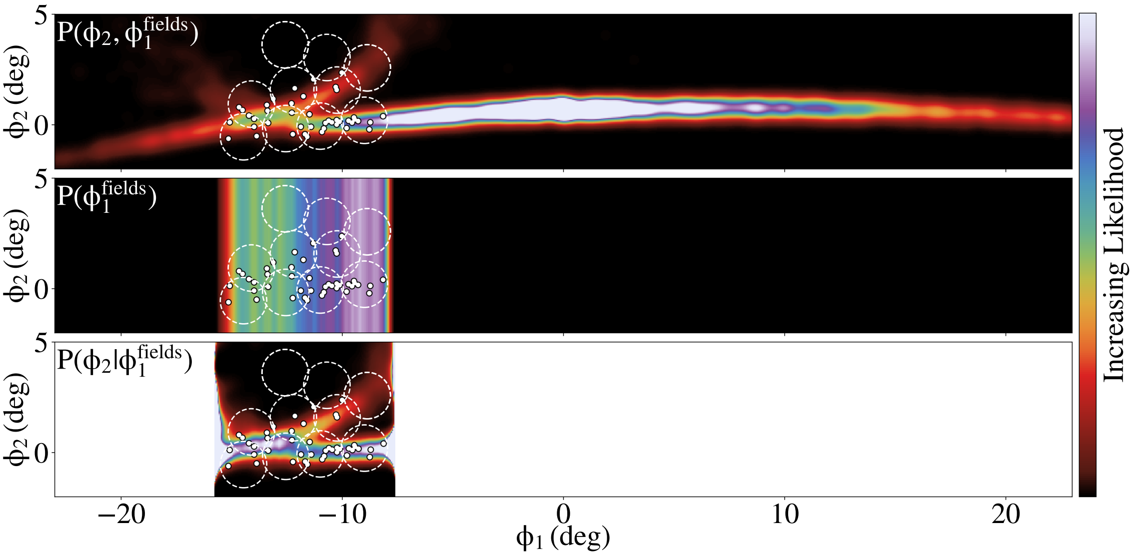

Figure 3.2: Demonstration of the Kernel Density Estimation used at the ATLAS-Aliqa Uma kink, and the estimation of the likelihood for the stream track using this. Here, the exact probability density function each panel represents is shown on the top left of each panel. Specifically, the panels represent the following; Top: A Gaussian Kernel applied to both the ϕ_1 and ϕ_2 values of bandwidth 1 deg; Centre: An Epanechnikov Kernel applied to the ϕ_1 values only of bandwidth 0.5 deg; Bottom: the resulting likelihood space produce from the two Kernel Density Estimations. Fields are shown in dotted white circles, with the observed ATLAS-Aliqa Uma stars shown as the black and white points. The corresponding value in likelihood space these points lie in is summed up to generate the total likelihood about the kink in stream track.

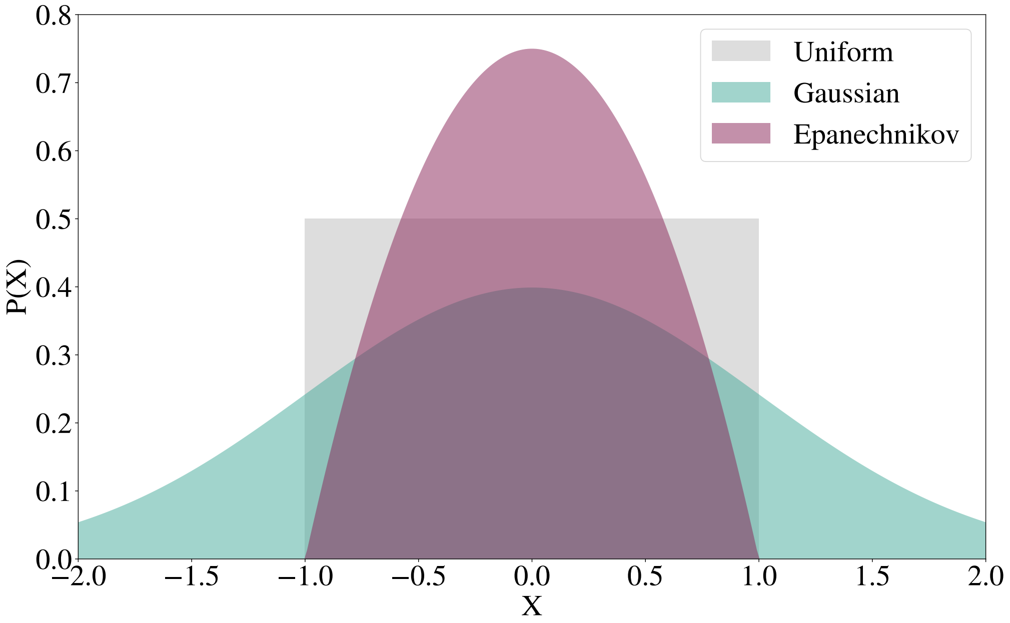

Figure 3.3: A comparison of the kernel type used in our Kernel Density Estimation. Here, we show the Gaussian kernel and how it compares to the more strict Epanechnikov Kernel used for P(ϕ_1^{fields}) with likelihood along the sky positions or P($\phi_1^{\text{fields}}, \phi_2$) for likelihood for radial velocities. A uniform distribution is shown as a comparison as well. All kernels here use a bandwidth of 1.

For each of these, we compute the probability density function using a combination of 2 different Kernels. These are visualised in Figure 3.3 and are as follows:

• A Gaussian Kernel of all model data (including those outside the fields and kink region) applied to the observed AAU stars within the kink. This is done on ϕ_1 and ϕ_2 combined when determining likelihoods in the track, and on ϕ_1, ϕ_2 and $\mathrm{v_r}$ combined for radial velocity likelihoods. In addition, we renormalise this using the ratio of the total number of model stars in the range $-23\,\mathrm{deg} \leq \phi_1 \leq 23\,\mathrm{deg}$ and $-2\,\mathrm{deg} \leq \phi_2 \leq 5\,\mathrm{deg}$, to the total number model stars within the fields. This makes the integral of the probability distribution within these fields equal to 1. The resulting probability density function as a result of the re-normalisation is effectively $\mathrm{P}(\phi_2, \phi_1^{\mathrm{fields}})$, or $\mathrm{P}(\mathrm{V_r}, \phi_2, \phi_1^{\mathrm{fields}})$ with the radial velocity observable, hence, representing the top panel in Figure 3.2.

• An Epanechnikov Kernel applied for model data inside fields within the kink. This is only applied to their ϕ_1 values for likelihood along the track, with the inclusion of ϕ_2 for radial velocities. This will hence, produce the probability density functions $\mathrm{P}(\phi_1^{\mathrm{fields}})$ or $\mathrm{P}(\phi_1^{\mathrm{fields}}, \phi_2)$.

The 2 different KDEs used here, have two main benefits. The first of this, is to allow us to normalise density of stars along the stream. Our simulated streams will have a much higher density of stars approaching the stream progenitor, as it is continually adding stars in order for them to be stripped (as shown in $\mathrm{P}(\phi_2|\phi_{1,\mathrm{fields}})$ as we go towards ϕ_1 of 0 in Figure 3.2). The likelihood being a ratio between these two eliminates this and results in a similar likelihood along the stream track instead of higher likelihoods being focussed only on the densest part of the stream (which would lie outside the kink region anyway). While we have seen from the results in Li et al. (2021) that the Aliqa Uma portion of the stream has lower densities than ATLAS, we both are not confident enough in the data to consider this in the likelihood, and do not have a stream generation method that is designed to recreate these results. Over the 4 Gyr period a stream is generated using our method, the rate at which stars are injected and stripped averages out to a constant rate and there is no time dependence here.

The choice of 2 different kernels carrys the second benefit. The probability density function of the Epanechnikov kernel only goes as far as its bandwidth (as opposed to Gaussian, as shown in Figure 3.3, which ensure a more consistent distribution of stars along the stream. This is because while the Gaussian kernel follows an exponential form, the Epanechnikov kernel follows a quadratic form of $1-x^2$, which is negative (hence, 0 probability) for values outside its bandwidth x. This causes the probability density function at any given point to be completely unaffected by stars further than our bandwidth of 0.5 deg from it, allowing us to consider only those very local to the observed stars within the kink. Given we do not expect any gaps to be present close to the observed stars even with the kink present, we can ensure the fits will always have model stars along and nearby observed stars. We further ensure this by reducing the bandwith for the KDEs that use an Epanechnikov Kernel compared to those with the Gaussian kernel.

For the radial velocities, this Epanechnikov kernel is however, applied to both ϕ_1 and ϕ_2. While for the track, model stars with very different ϕ_2 to the AAU data can affect the likelihood here, this is not the case for the stars to include in radial velocities. We only want to consider model stars very close in sky positions (within 0.5 deg) to the observed data when determining the likelihoods for radial velocities, as we have found even in Chapter 2 that the radial velocity features would make us want to avoid doing simple bins in ϕ_1, grouping stars together with very different radial velocity values that aren't near eachother in the sky.

3.3 A stochastic exploration of parameter space

We applied this new likelihood calculation to a few different methods to explore parameter space. For our previous work in Chapter 2, we started our fits using EMCEE close to the true solution and demonstrated how it could recover the the impact parameters. With these fits to real data, we are not able to make assumptions like this and instead do a preliminary exploration using both the DYNESTY MCMC (Speagle, 2020) and the scipy optimization function, differential evolution.

The choice of this initial exploration stems from the main limitation of emcee. The approach of emcee to likilihood space means it gets very easily trapped in a certain solution if the likelihood space has a local maximum. It will rarely go too far from this and will therefore, struggle to obtain other potential solutions if their impact parameters differ significantly. As a result, we aim to first obtain a list of possible solutions using the above methods of dynesty and differential evolution, which we can then run MCMC fits of.

We demonstrated in Chapter 2 that a direct impact will likely have to be very recent to produce a kink. We however did not consider impacts further away from the kink, which could cause the perturbed stars to instead drift into and form the kink over longer timescales. Based off of our progenitor properties, the kink is on the trailing end of the stream, which leaves room for encounters very far up the stream which would not affect stars local to the kink at the time of impact. By perturbing these stars to higher energies, or values in ϕ_2, their orbital periods would then be slower and these stars would drift down the stream. To explore potential impacts like this, we ran some encounters ourselves and explored a grid of impact time between 2 Gyr and 3 Gyr in steps of 0.1 Gyr, stream angle between 0 deg and 10 deg in steps of 0.1 deg, and subhalo mass between $10^6\,\mathrm{M}_\odot$ and $10^8\,\mathrm{M}_\odot$ in steps of $10^6\,\mathrm{M}_\odot$. This was further motivated from the fact that the feature is now less clear on where it is one continuous track with a kink in ϕ_2, similar to how it was treated in Chapter 2, or if it is closer to a spur/nearly parallel group of stars branching off of the track. In the case of the latter, this encounter process would potentially be able to produce such an effect as evidenced in Figure 3.6 which will be further discussed in Section 3.5.2.

3.4 MCMC fits of the kink

We ran a series of MCMC fits to the AAU stream, with initial guesses based off of both our mock impact in Chapter 2, along with our own exploration of older impacts. The recent impact using initial guesses from Chapter 2 stems from the fact we chose mock data to look like the AAU kink in the first place, so it would make a good starting point for the fits.

3.4.1 Exploration and fits using dynesty

Performing fits using dynesty use only an input of priors that govern the parameter space to explore. This is unlike emcee, where we must input an initial guess as a starting position for the walkers. In total, we ran 4 dynesty MCMCs, with these priors all remaining identical except for the impact time T_a. The parameters below are similar to the limits of emcee used in Chapter 2

- A uniform prior on b, the distance of closest approach, of 0 and 1 kpc.
- A uniform prior on α, the orientation of the closest approach relative to the Galactic centre, between 0 and 360 deg.
- A normal prior on $V_\perp$, the subhalo velocity perpendicular to the direction of the stream, with a mean of 0 and σ of 194.2 $\mathrm{km\,s^{-1}}$.
- A normal prior on $V_\parallel$, the subhalo velocity parallel to the direction of the stream, with a mean of 0 and σ of 194.2 $\mathrm{km\,s^{-1}}$.
- A uniform logarithmic prior of base 10 on subhalo mass, M_{sat}, between 10^4 and $10^8\,M_\odot$.
- A uniform prior on impact time, t_a, between the following 4 ranges: $0-0.5$ Gyr; $0.5-1$ Gyr; $1-2$ Gyr; $2-3$ Gyr.
- A uniform prior on the impact angle along the stream, ϕ_a, between -10 and 10 deg.
- A uniform logarithmic prior of base 10 on the subhalo scale radius, rs_{sat}, between 10^{-3} and 1 kpc.

The choice of prior and dispersion in the velocities here is to allow for both positive and negative values of velocity. By equating the dispersion to double the circular velocity at that radius (97.1 $\mathrm{km\,s^{-1}}$) and centering the distribution on 0, we can allow for encounters of all orientations while covering a similar range for the magnitude of the velocity as the Maxwellian distribution used in Chapter 2.

We use 4 different impact times here to ensure a particularly detailed exploration into this parameter, as all attempts to fit features such as the AAU kink were very recent, within 0.5 Gyr ago or less. This MCMC sampler would still explore all ranges of t_a

Our first 2 ranges of $0-0.5$ Gyr and $0.5-1$ Gyr were both focused on encounters which follow this similar idea of a recent interaction directly where the kink is. An example being the style of encounters used in our mock fits in Chapter 2. The first range would aim to find encounters such as this, while the second range would follow a possibility that a similar perturbation could instead be happening roughly one orbital prior to the present position (which for our generated progenitor, has a period of ~ 0.69 Gyr). This second range was chosen as Erkal & Belokurov (2015b) found that fits separated by one orbital period could still produce similar looking gaps for present day data quality. It is unlikely that encounters could be occurring too far away within these time priors as stars would not be able to drift into the kink fast enough. Instead, this mainly seeks to fit a stream-subhalo interaction directly where the kink is.

The last 2 impact times of $1-2$ Gyr and $2-3$ Gyr were then to explore the idea of a perturbation further up the stream, which will then result in stars being perturbed to higher radii and drifting down with their longer orbital periods. We believe over these timescales, small velocity kicks even smaller than 1 $\mathrm{km\,s^{-1}}$ could still manage to cause stars to drift from leading in front of the progenitor to behind it at the kink. Meanwhile at these times, we would not expect to see any remnants of a direct impact at the kink, based off of how we expect gap formation to behave from Chapter 2.

3.4.2 Fits using emcee

All fits through MCMC did converge on a similar style of stream (see Figure 3.13), which we further explore in section 3.6.2. In particular, all streams generated ended up with a higher mass, dense subhalo which goes through along the length of the stream, as shown by the minimum separation between every star and the subhalo being close to 0 kpc, a direct impact. This creates a highly diffuse perturbed stream which ended up suiting the likelihood estimation.
It is worth noting that the emcee fits had not approached their convergence times of 50x the autocorrelation time. Typically, for these fits the autocorrelation times were in the order of 2000 or higher. Each encounter meanwhile would take $\sim$3 minutes, which in the context of running the MCMC for this long would not be feasible to to reach these autocorrelation times.

3.5 The potential nature of a subhalo encounter with the AAU stream

Here we will present some scenarios of AAU fits that were performed either by eye, or were initial results output from dynesty or differential evolution. In the latter case, the results did later on veer into a similar fit to what was shown above. The choice if these 2 is to showcase 2 very different styles of impacts regarding how long ago it would have occurred, where along the stream it impacted and the scale radius of the subhalo. Still, both produce a feature which on an initial qualitative look, would fit most of the observed stars on the track.

We have 2 scenarios shown below which could produce features in the track similar to the our current observations. This involves a recent encounter directly at the kink, in a similar fashion to our work in Chapter 2, and one significantly further along the stream at $\phi_1 \sim 40$ deg that causes perturbed stars to drift into the kink region over a few Gyr.

We use 3 key figures to showcase each fit and the how they each produce the kink in a unique way, Figures 3.2, 3.4 and 3.5 for the recent impact, and Figures 3.6, 3.7 and 3.8. This includes a panel of all observables in a similar fashion to Figure 2.3, though with the addition of a panel of the velocity kick, alongside the proper motions being shown in ϕ_1 and ϕ_2. These proper motions are used to better highlight how the stars in the kink would be expected to move in the track over time. We also show a figure of their dispersions, both as the width in the track and the velocity dispersion. Finally, we also show a figure displaying the PDFs used for likelihood estimation.

3.5.1 A recent encounter from a dense, compact object

The first encounter we show here is rather similar in nature to the mock impact used in Chapter 2 and is shown in figures 3.4, 3.5 and 3.2. These parameters are obtained from preliminary results of dynesty fits. Here, our subhalo has the following 8 parameters

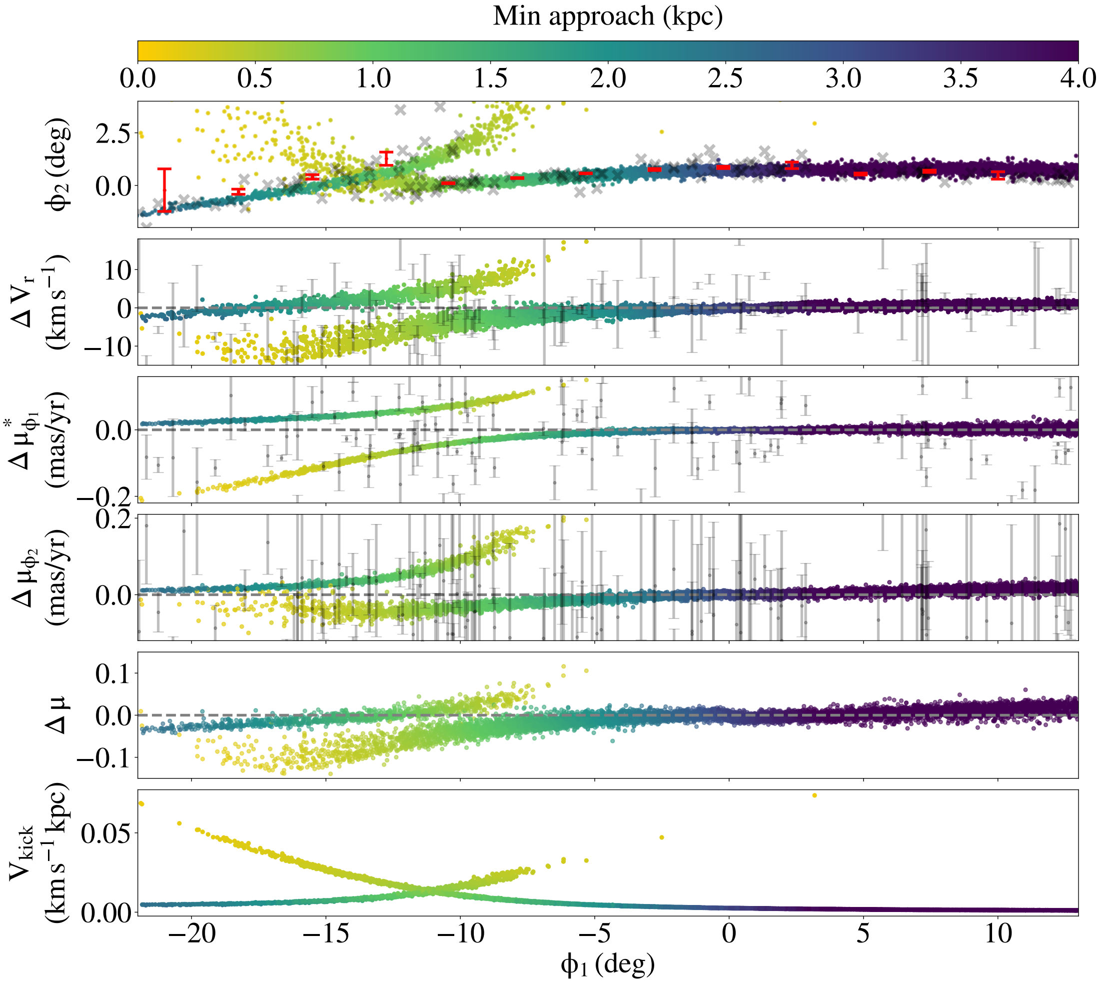

Figure 3.4: Observables of the fit to the AAU stream for a very recent, very dense subhalo scenario. In each panel, the simulated stream is shown in points coloured by their closest approach to the subhalo. Additionally, where applicable, the observed AAU stars are shown in gray colourbars or crosses. **Top panel:** The stream track in rotated sky coordinates. Here, we additionally show red errorbars which represent the spline fits made using AAU data just as what is shown in Li et al. (2021). **Second panel:** The radial velocity difference between the simulated data and a fourth order polynomial fit on an unperturbed model. This model being generated using a progenitor with the same initial conditions as the perturbed stream here. **Third and Fourth panel:** The proper motion difference between the simulated data and a fourth order polynomial fit on an unperturbed stream, much in the same vein as the second panel. Proper motions are in ϕ_1 and ϕ_2 for the third and fourth panels, respectively. **Fifth panel:** The difference in distance modulus between the perturbed model and a fourth order polynomial fit to the unperturbed model, once again in the same vein as the second, third and fourth panels. **Bottom panel:** the velocity kick received by each star).

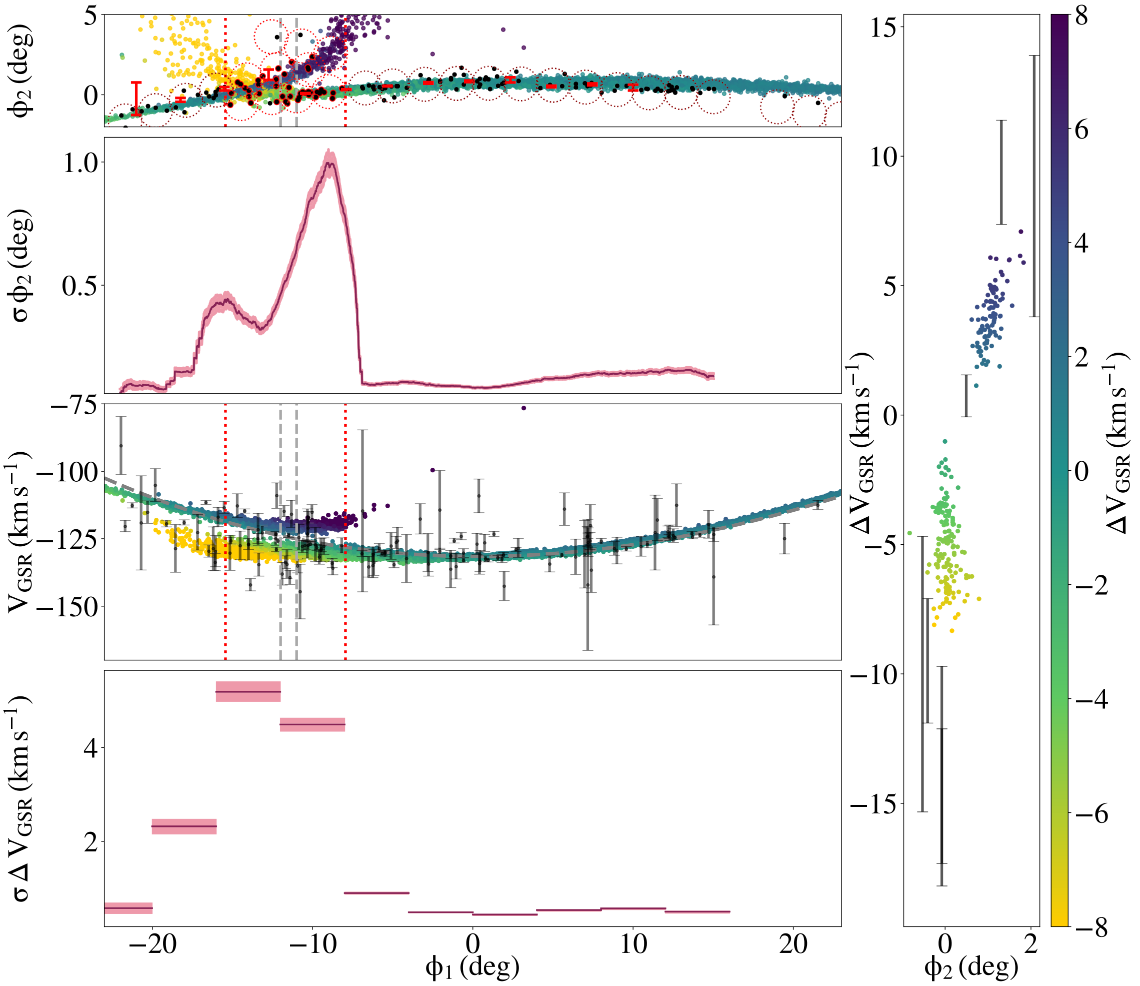

Figure 3.5: Dispersions along the stream track and velocities. Simulation stars for all plots in this figure are also coloured according to their V_{GSR} values relative to a polynomial fit to the radial velocities, explained further below. **Left:** The top 2 panels here show the stream track along with the width of the stream. The fields specifically used for the likelihood estimation are shown in the red dotted circles, with only those enclosed in the vertical red dotted lines utilised. These remaining fields however are stilled used to restrict the data when determining stream width. The actual observed AAU stars are shown in black points (with those points inside the fields highlighted in red). Additionally, the spline fits along the AAU track are shown in red errorbars here. The shaded region above and below the stream widths here showcase the $1-\sigma$ uncertainties. The bottom 2 panels here meanwhile show the velocity V_{GSR} along this same stream, with the velocity dispersion on the bottom. We show the observed AAU data as grey errorbars here. A polynomial curve is fit to V_{GSR} as the dashed grey curve, fit to a stream generated without a subhalo, with the same progenitor properties as our fits. The velocity dispersion is shown here in 4 deg slices, set up so that we have 2 bins here over the kink region. Just like the stream widths, we restrict model data used to determine the dispersion to the fields along the whole stream, and the shaded region here is used to show the $1-\sigma$ uncertainties. **Right:** The difference between the V_{GSR} values for stars and the fitted curve on the left panel. This is taken only for stars within a slice between ϕ_1 of -11 and -12 deg, which is shown by the vertical gray dashed lines in the panels on the right. The observed AAU stars are included here as dark gray error bars.

governing the encounter: $b \approx 0.12\,\mathrm{kpc}$; $\alpha \approx 285\,\mathrm{deg}$; $v_\perp \approx 65\,\mathrm{km\,s^{-1}}$; $v_\parallel \approx 64\,\mathrm{km\,s^{-1}}$; $T_a \approx 0.14\,\mathrm{Gyr}$; $\phi_a \approx -3.7\,\mathrm{deg}$; $M_{sat} \approx 8\mathrm{x}10^7\,M_\odot$; $rs_{sat} \approx 0.005\,\mathrm{kpc}$.

The resulting stream follows a lot of our expected features of a direct impact of a subhalo on a stream, notably, how in Figure 3.5, we have a stream here with high width and dispersions along the kink, but a relatively constant and very thin width and dispersions outside of this. This is no surprise given the size of the feature here, which is a far more significant perturbation than our mock impact of section 2. The 2 individual spurs on the track also leave behind very clear signatures on the rest of the observables in Figure 3.4, with the features present in these observables very easily being matched to the stars in the track on the top panel.

When using these impact parameters in emcee instead of the later dynesty parameters, the dense subhalo here did not need to be changed much to produce a fit with a very high stream width and higher likelihood.

3.5.2 A very old encounter further along the stream

The second encounter shown here is from a grid search we ran ourselves as explained in Section 3.3, and we show the results in Figures 3.6, 3.8 and 3.7. With a fixed impact time and stream angle, we could increase the mass, effectively increasing the velocity kick and the feature would drift further to the left in the top panel of Figure 3.6, along with eventually joining back onto the stream. We chose the sample that qualitatively seemed to best match the AAU data, which involved the following impact parameters: $b = 0\,\mathrm{kpc}$; $\alpha = 90\,\mathrm{deg}$; $v_\perp = 30\,\mathrm{km\,s^{-1}}$; $v_\parallel = -80\,\mathrm{km\,s^{-1}}$; $T_a = 3\,\mathrm{Gyr}$; $\phi_a = 10\,\mathrm{deg}$; $M_{sat} = 6\mathrm{x}10^7\,M_\odot$; $rs_{sat} = 0.1\,\mathrm{kpc}$.

A clear proper motion signature of the drifting stars can be seen in the third panel in this figure, with the stars with a very close approach to the subhalo having the only significant proper motions in ϕ_1. We note though that for all panels these proper motion differences are significantly smaller to the first fit. There does appear to also be a population of stars formerly on the left of the stream which are drifting further up the stream too based off of their slightly positive proper motions in ϕ_1. Unlike the fit in Section 3.5.1, there are no significant features in radial velocity, though we note based off of Figures 3.8 and 3.6, the velocity dispersion is slightly higher throughout with the exception of the kink region for our recent impact.

We attempted to get fits of this based off of inputting similar priors as the grid search into dynesty, along with inputting this encounter directly into emcee afterwards. Both were still unable to return promising results if either sampler was ran for more than a few days. An example of these results is discussed in Section 3.6.2.

3.6 Discussion

3.6.1 The qualitative fits to AAU

The fits shown in Section 3.5 alongside the AAU data itself reveal a great deal towards the difficulties on discerning the type of subhalo interaction that could produce the AAU

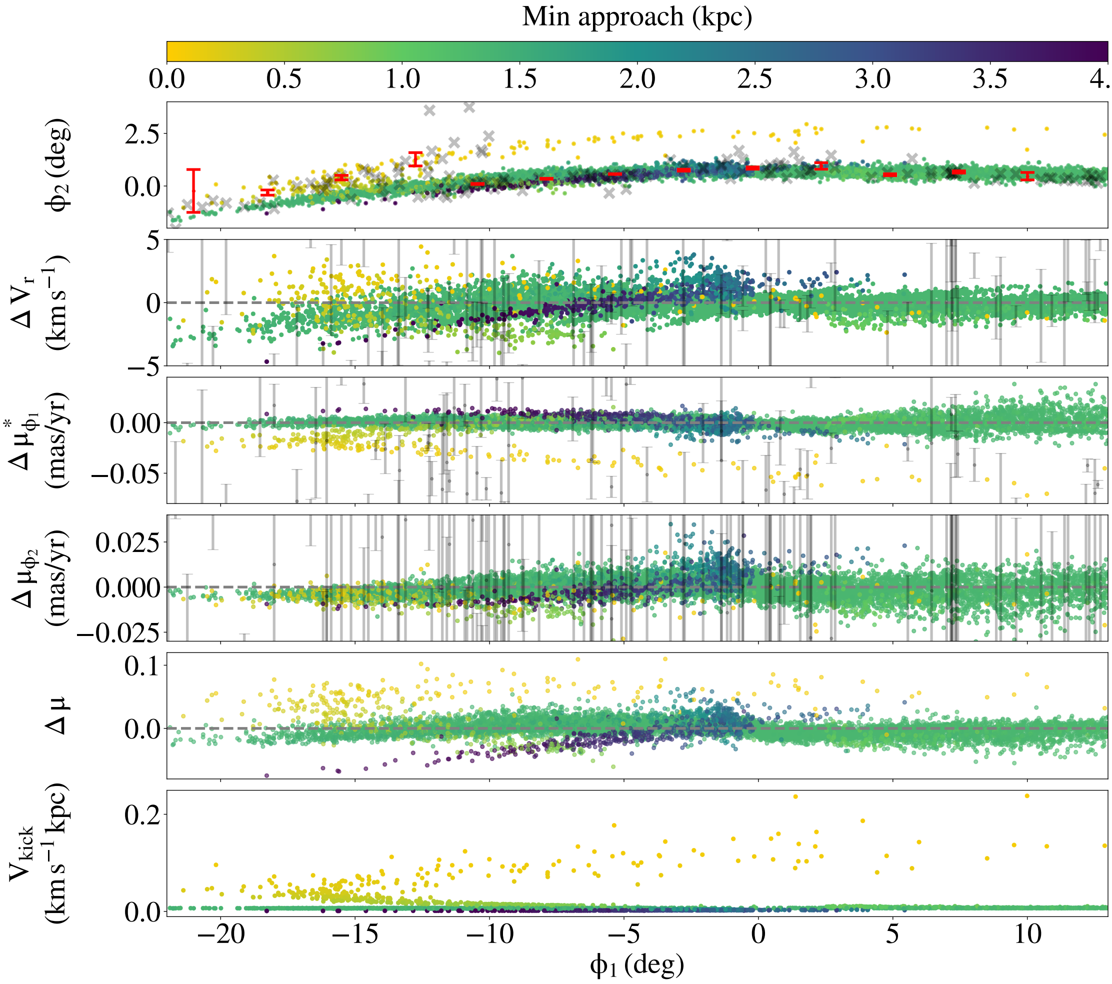

Figure 3.6: The same as Figure 3.4 for our second stream-subhalo scenario. This encounter consisting of a an older interaction to stars further up the stream, which drift into the kink after being perturbed. Note that the limits for most panels of observables are far smaller here, since this was a smaller perturbation applied very early in stream generation.

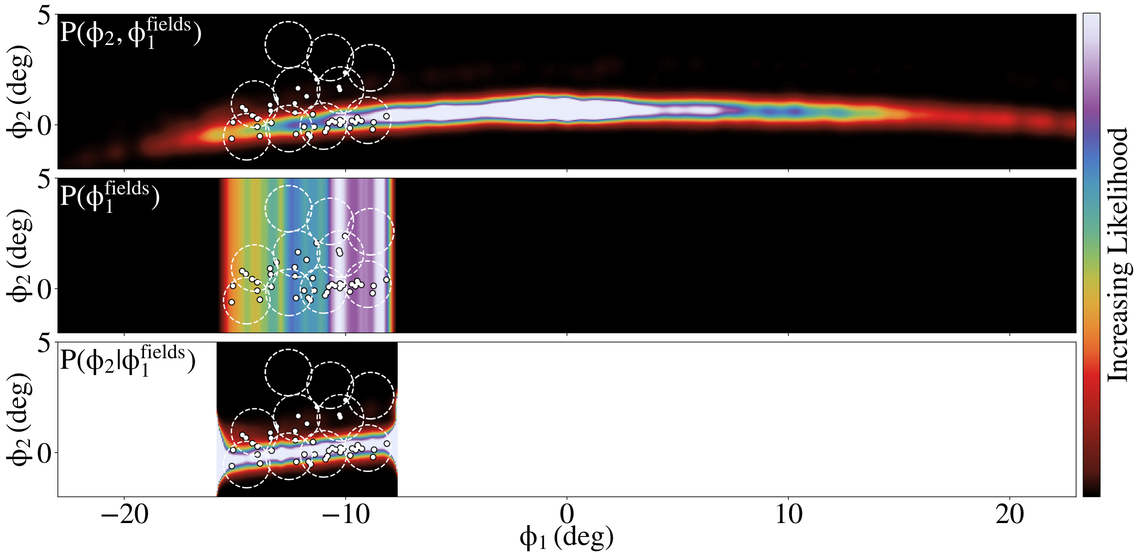

Figure 3.7: The same as Figure 3.2 for the older subhalo encounter further up the stream. This highlights how the lower density of particles that make the kink for this interaction have smaller effects on the likelihood when determined using the KDE.

stream. With particular focus on figures 3.5 and 3.8, they each have some similarities with either their morphology or kinematics to the AAU data.

On the morphology front, AAU has noticable differences in the stream width when comparing its Aliqa-Uma part against the ATLAS part, with Aliqa Uma still maintaining broader stream widths than ATLAS even outside of the kink region. We note that Figure 3.5, along with similar fits with subhalo impacts directly on the kink do not behave in this way. By making this direct impact on the stream track which otherwise covers the whole AAU track, the perturbed stream we generate has very similar stream widths and density either side of the kink. Our older fit meanwhile in Figure 3.8 manages to recreate these widths, as the group of stars that drifted down the stream is now what is forming Aliqa Uma (along with its different stream width), with the stars that are above the ATLAS part of the stream too far above the main track and outside the fields to influence the width. With this in mind and the fits we have been able to create, the morphology of AAU suggests we are more likely to be dealing with an older impact not local to the kink.

Moving on to the kinematics of the AAU data, these show that across the kink has a very steep slope between $\Delta\,\mathrm{V_{GSR}}$ and ϕ_2, going from $\sim -15\,\mathrm{km\,s^{-1}}$ to $\sim 10\,\mathrm{km\,s^{-1}}$ over a difference in ϕ_2 of only 2 deg. This is matched fairly well by our recent impact on the right panel of Figure 3.5, though the older impact in Figure 3.8 has a significantly shallower slope. Given the mechanism by which we have to fit AAU by drifting stars into it from further up the stream, we could not recreate the morphology with any significant feature in radial velocities. The very long timescale the stars have to drift into place meant we could only use very slight radial velocity kicks. While we explored a similar mechanism to this by using a heavier subhalo at earlier times, the result was a more diffuse stream relatively speaking due to the fact that the more

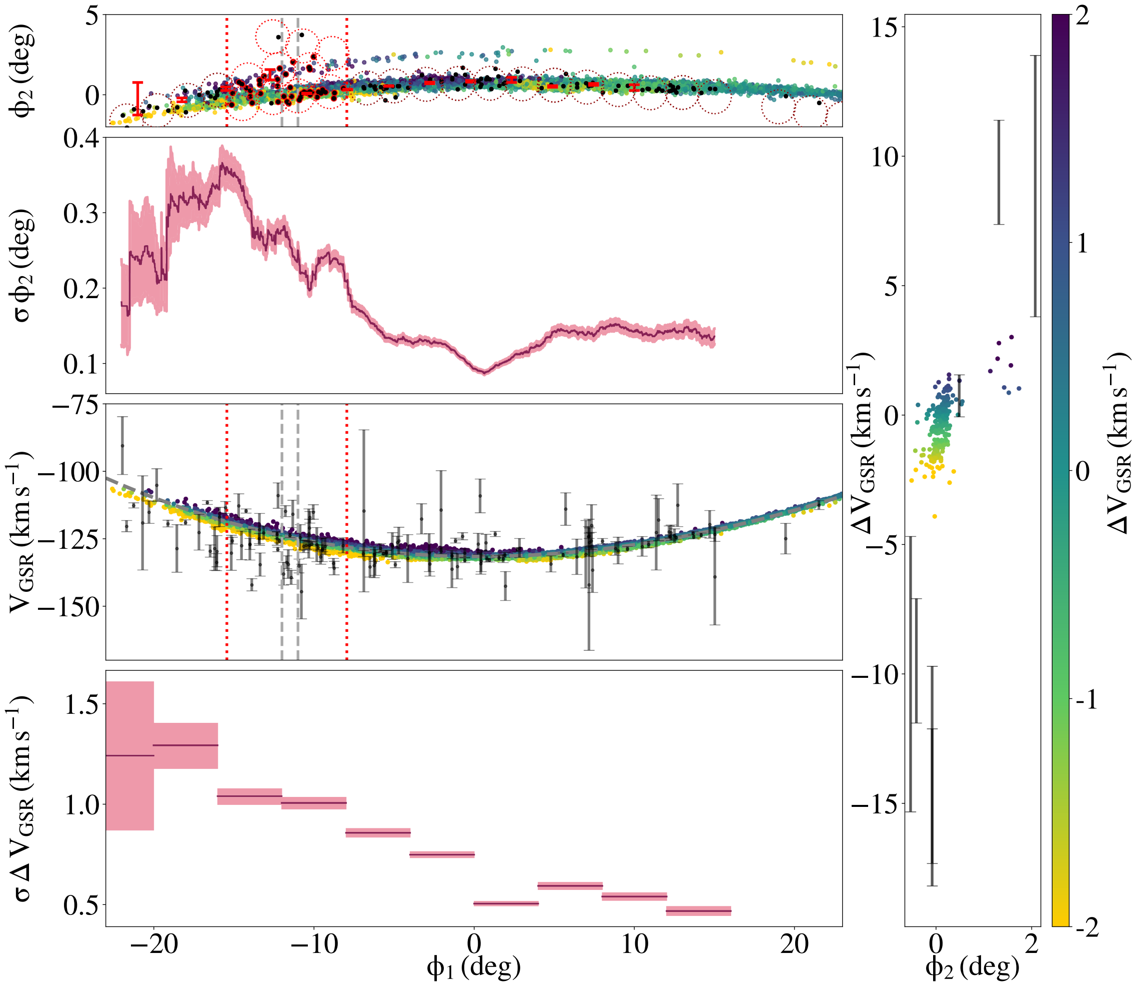

Figure 3.8: The same plot as 3.5 but for our older impact. Here, we adjust the range used for colouring the points due to the fainter gradient between ϕ_2 and $\Delta\,V_{GSR}$, to better highlight potential radial velocity features in the track.

populated the stream is with stars. This meant we did have populations of stars drifting into similar ϕ_1 values, but they would differ on average in ϕ_2 due to the greater velocity perturbation. A direct impact that is recent meanwhile is not likely to have this issue, due to the size of the perturbation needed to produce a kink in such a short timescale. The does make the kinematics of AAU instead, favour a recent impact directly on the kink.

Another significant difference between these features is in the length and shape of the stream. We showcase the full stream across ϕ_1 in Figures 3.9 and 3.10 instead of the previous figures limiting the range to where we have data. As expected the recent impact has very little impact on the stream beyond the kink region and would match the length of an unperturbed stream with this progenitor. The older fit meanwhile ends up with a significantly longer stream. Based off of the minimum approaches in Figure 3.10, they suggest the extended parts of the stream above $\phi_1 = \sim$ 50 deg are the perturbed stars from the impact at $\phi_1 = \sim$ 40 deg which continued drifting down into a long trailing arm. We do note that the subhalo does have multiple near encounters for the second fit, and Figure 3.11 shows that a large portion of the leading end of the stream does get very close to the subhalo. We note that Figure 3.6 does have the population of stars that seemed to have received a perturbation causing their proper motions to increase in ϕ_1, hence their drifting further up the stream and resulting in the less populated, higher stream width to the left of the kink. While their closest distance to the subhalo here is quite large, this is reflected by the far smaller proper motion feature they have compared to the stars that drifted down the stream into the kink.

We can also clearly see now the behaviour of the feature for the first fit of a recent subhalo encounter. The proper motion signatures in Figure 3.4 show the clear halves of this loop and how the stars are drifting due to their proper motions. The positive proper motions in ϕ_1 for the perturbed stars on the right appeared unusual at first, especially given their positive proper motions in ϕ_2 as well, which we would expect to result in a higher radius orbit and hence the stars beginning to drift to the left. With the perturbation being so recent, where the track is still in fact connected after the subhalo flyby, we are probably dealing with a very short lived feature which matches Figure 2.3. There, proper motion signatures are directly from the subhalo perturbation and these positive proper motions in ϕ_1 will likely begin to decrease now due to the higher energies of the stars and the feature will mostly smooth out and gap formation will occur as explained in Erkal & Belokurov (2015a). While these are qualitative results, an advantage of an impact such as this fit is how the subhalo will remain in close vicinity to the stream. The results of Chapter 2 show that using emcee we can constrain the subhalo locations well for a recent impact. We could use this to attempt to find any traces of potentially unobserved GCs in this region to better discern if this could be a dark matter subhalo without any population of stars.

Subhalo properties

Our findings for the main 2 scenarios, along with the typical masses produced by dynesty, emcee and Differential Evolution all show subhaloes that are far denser than ΛCDM predicts. The least dense subhalo we find is produced from our second, very old impact consisting of a 6x10^7 $M_\odot$ subhalo with scale radius 100 pc. Under ΛCDM meanwhile, we would expect this scale radius to be at least 400 pc (Moliné et al., 2017). Conversely, our very recent first impact has a heavier subhalo of 8x10^7 $M_\odot$ with significantly smaller scale

Recent impact

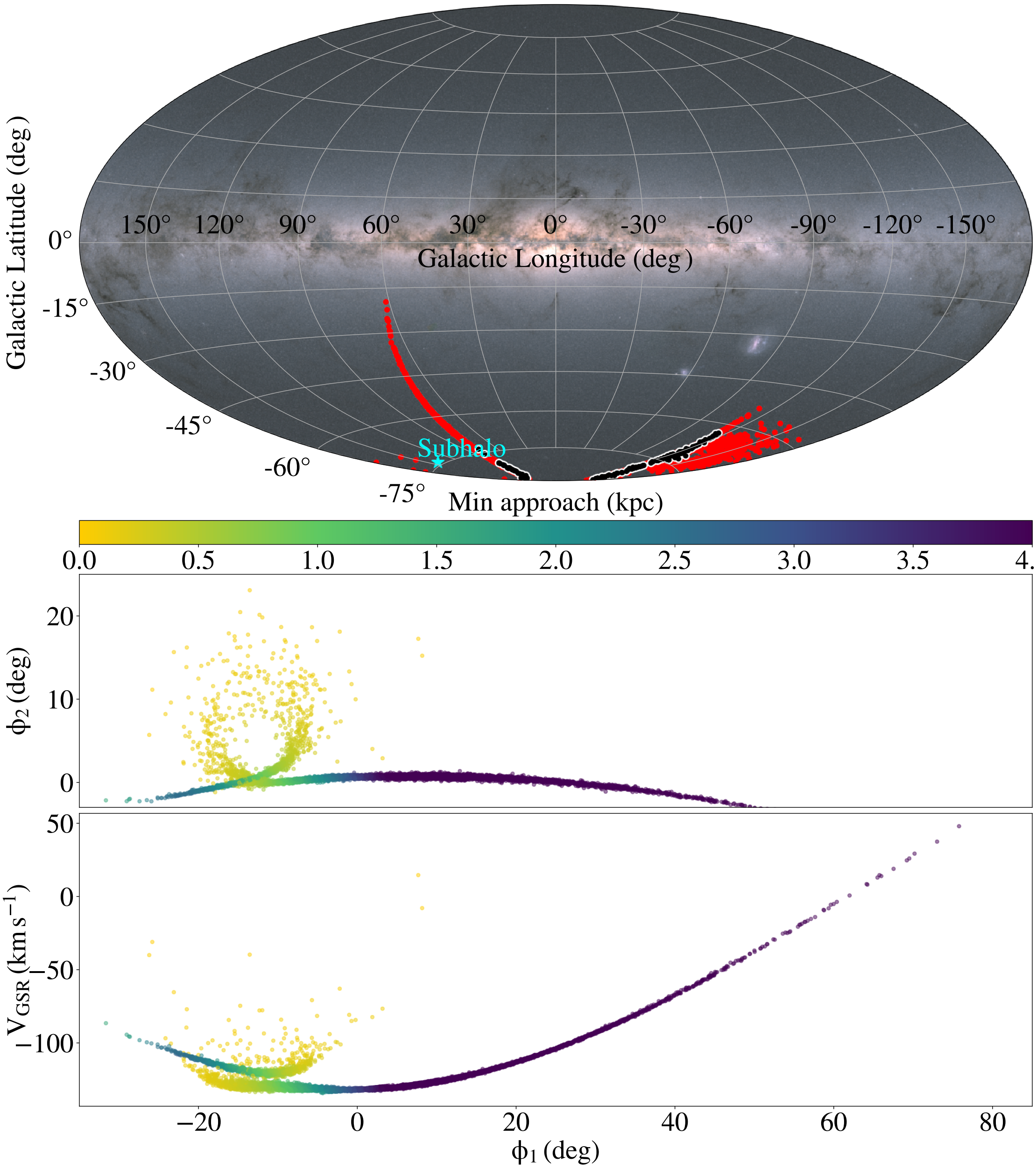

Figure 3.9: An overview of the perturbed for the recent impact, showcasing the shape and positions over the full length of the stream. **Top:** Sky positions of the stream, alongside the present day subhalo location. **Middle:** Full stream track of the impact, showcasing the full extent of the features present along this due to the impact, coloured by the closest distance between the model stars and subhalo. **Bottom:** Velocities in $\Delta\,V_{\rm GSR}$ accross the whole stream track.

Older impact

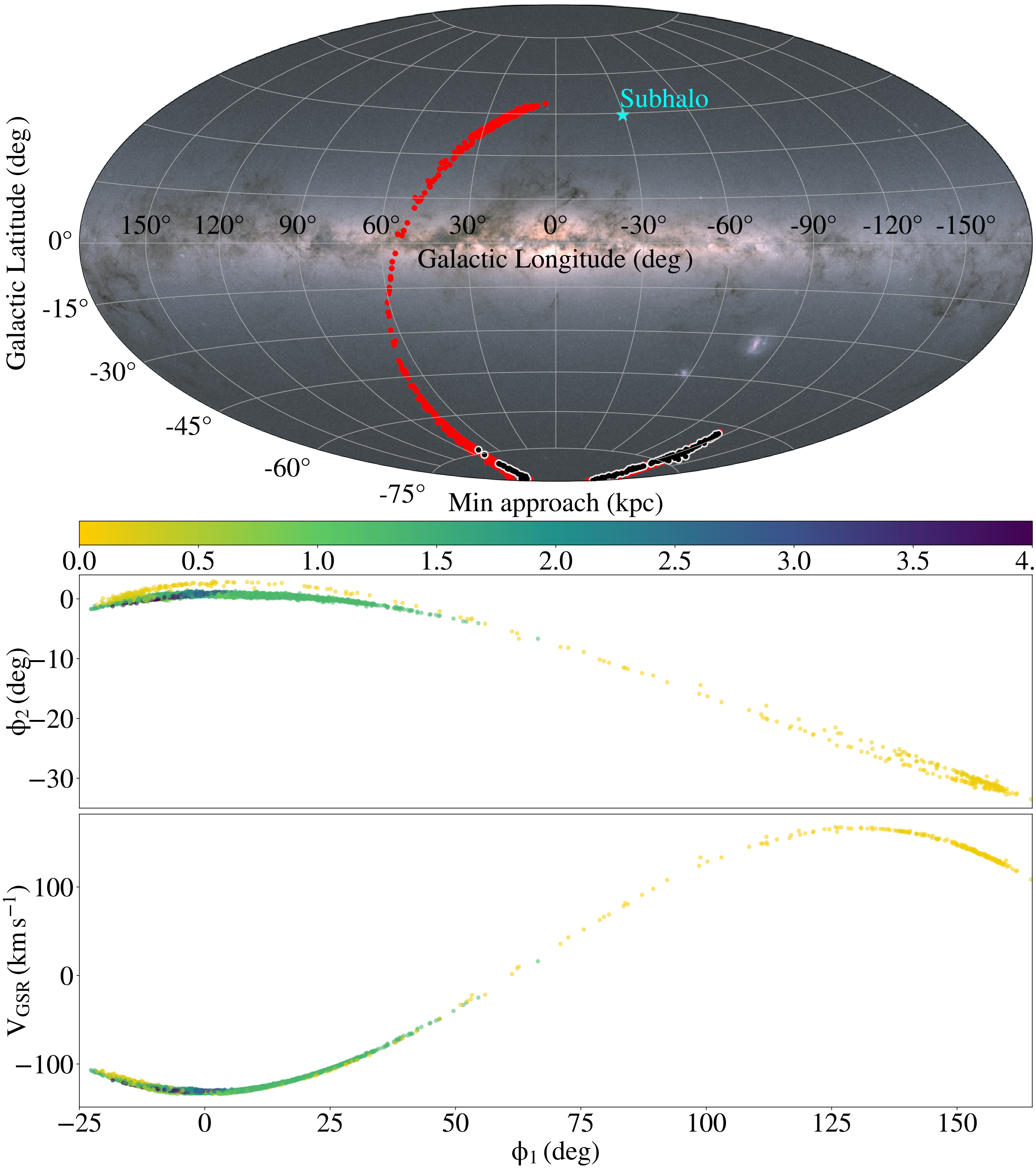

Figure 3.10: The same as Figure 3.9 but for the older impact. Note that the range in phi_1 covered in the bottom 2 panels is very different to the recent impact, with the stream being significantly longer from this impact.

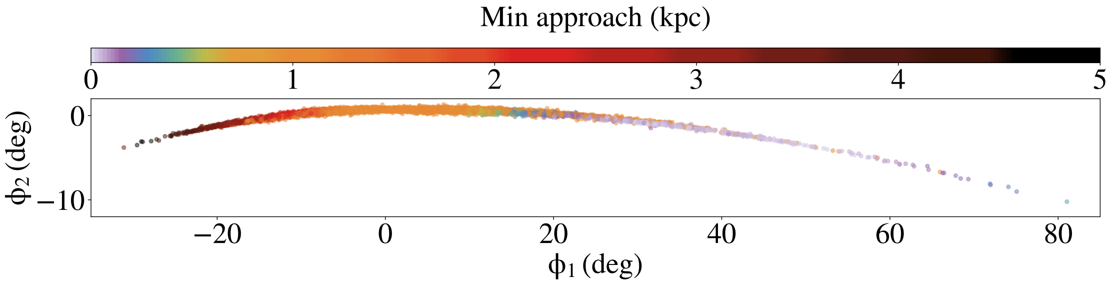

Figure 3.11: An unperturbed stream with progenitor properties identical to our AAU fits. Here, we use a massless subhalo with the same orbit as the older impact fit and show the closest approach distances to the stars along the unperturbed stream, showcasing where the older impact occured along the stream.

radius of $\sim$ 5 pc. These are in relatively good agreement however, with fits performed on the GD-1 stream by Bonaca et al. (2019). The subhaloes that Bonaca et al. (2019) found to produce similar features to what is seen in GD-1 had scale radii that did not go far above 100 pc, while maintaining masses in the region $10^6 - 10^8\,\mathrm{M}_\odot$. In some instances this would involve masses too high for GCs while maintaining the very low scale radius.

The energy and angular momentum of these subhaloes are additionally shown in figure 3.12. For our recent impact, the subhalo is on an orbit with pericentre and apocentre of $\sim$ 29 kpc and $\sim$ 44 kpc respectively. This also has an orbital period of $\sim$ 0.89 Gyr. The older impact meanwhile, features one on a much lower radius orbit with pericentre and apocentre of $\sim$ 13 kpc and $\sim$ 18 kpc, and an orbital period of $\sim$ 0.33 Gyr. Compared to larger known dwarf galaxies such as Sagittarius, the angular momentum of these orbits are clearly different, particularly in the Ly-Lz plane where classifications from Johnson et al. (2020), Petersen & Peñarrubia (2021) and Peñarrubia & Petersen (2021) would all exclude these subhaloes.

3.6.2 MCMC fits

In the sections above we have carried out an extensive look at the 2 main qualitative fits involving our own grid search and preliminary results. We now discuss the originally intended fits which would have been made following this initial exploration with the preliminary results and explore their attempts to fit the AAU kink.

As stated above, both EMCEE fits and dynesty produce similar results consisting of a very diffuse stream with in some cases, no thin stream evident anymore. Typically, all stars in the stream have had very recent encounters with the subhalo as shown in Figure 3.13. In general, the fits either have interactions which involve a subhalo on a similar orbit to the stream, which also produces a very slow encounter which applies a significantly higher perturbation, or there are times where the similar orbits result in numerous perturbations. There are fits here which have very fast subhalo encounters with only one interaction, though in these instances such as in Figure 3.13, the impact parameters end up in an interaction with the subhalo going roughly through the centre of track of the stream. While the subhalo-stream encounter setup is designed to define a closest approach, the

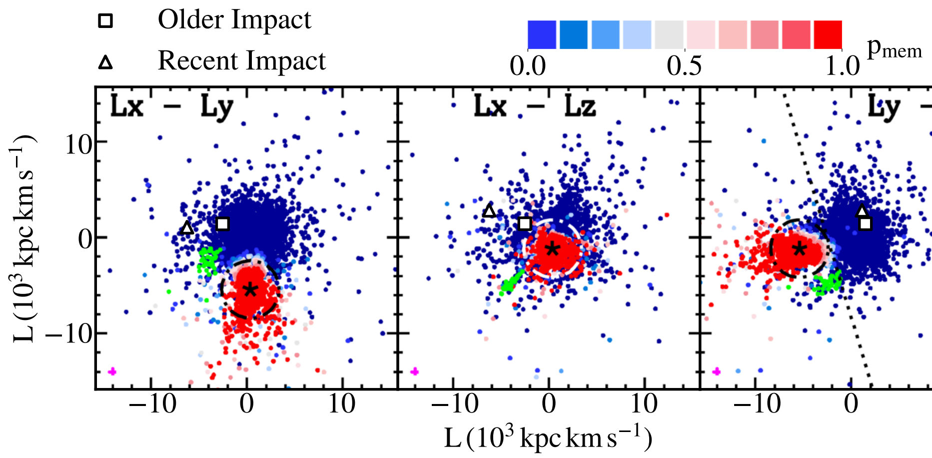

Figure 3.12: Angular momentum components of stellar halo stars as found in Figure 1 of Peñarrubia & Petersen (2021), including those which likely belong to Sagittarius with our 2 subhaloes from the qualitative fits overlaid. The stellar halo stars from their paper are coloured by probability of belonging to Sagittarius between blue and red. Displayed are also stars from the OC stream in green. Black star markers show the angular momentum of Sagittarius, with dashed circles in black or white showing a range of angular velocity from Sagittarius of 3000 kpc km s^{-1} which was used to classify member stars from previous work in Petersen & Peñarrubia (2021). There is also a dotted black line in the Ly-Lz panel, where Johnson et al. (2020) defined Sagittarius member stars as lying to the left of this line. Our own subhalo angular velocities are shown in the black and white triangle for the recent impact, and the square for the older impact. This demonstrates how these subhaloes are unlikely to belong to the Sagittarius stream

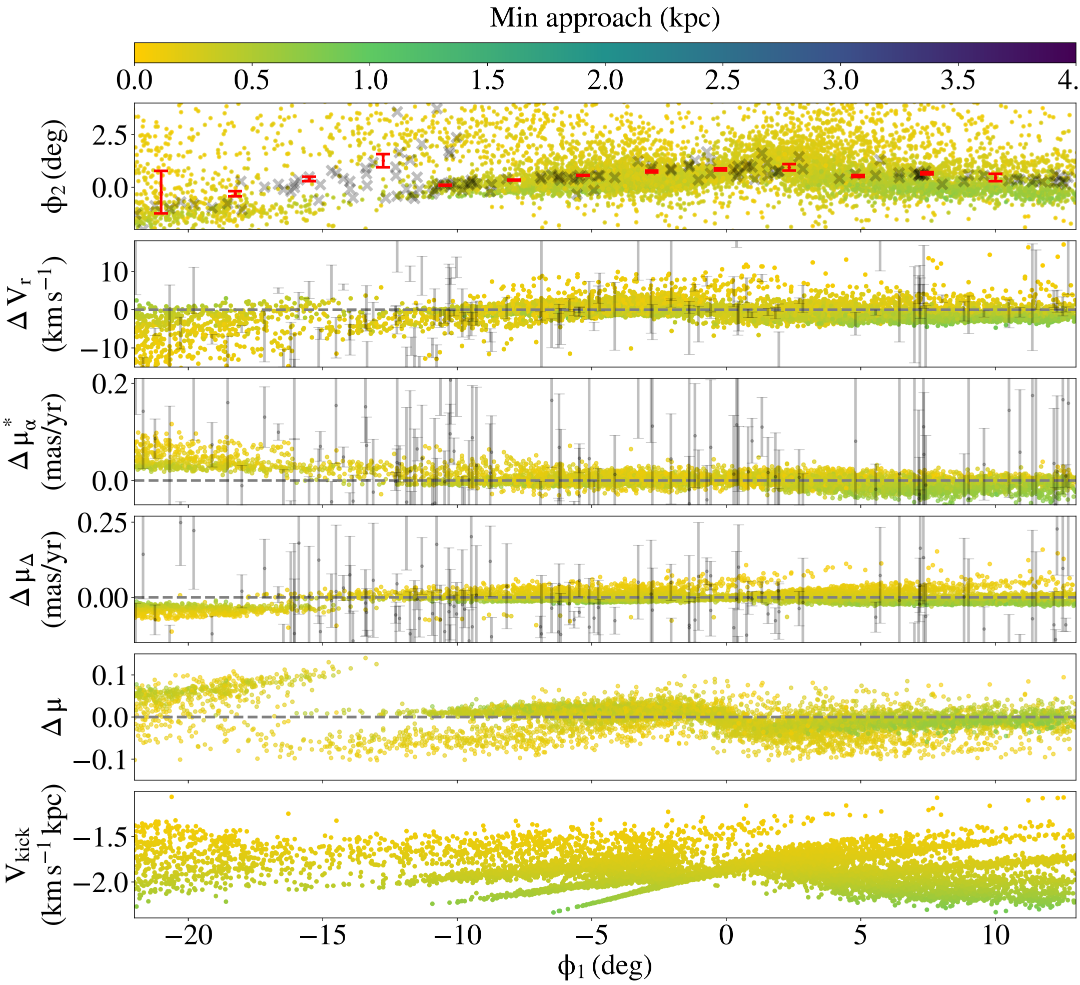

Figure 3.13: The same as Figure 3.4 but for one of our MCMC fits. This particularly highlights how every star in this region have had very close encounters with the subhalo, instead of the subhalo interacting with only a small group of stars along the stream.

assumption that the stream is travelling in a straight line results in some parameter setups that have a subhalo passing either multiple times, or travelling though the centre of the stream shortly after the impact as the orbit of the stream curves into and almost overlaps with the subhalo. This has highly unpredictable results on the stream track and velocities.

Limitations to the likelihood estimation

The KDE likelihood estimation for the track in Figure 3.14 shows how most fitting methods could have converged to a similar looking stream. In general, the 2 scenarios we show in Section 3.5 have some observed AAU stars on the cusp of a null value on the probability density function, which is returned for values outside the 0.5 deg bandwidth of the Epanechnikov Kernel in ϕ_1 for the track, or for this same bandwidth in both ϕ_1 and ϕ_2 when determining likelihood from radial velocity. The probability density function in Figure 3.14 meanwhile has no such regions in the probabilities that are this low near the AAU

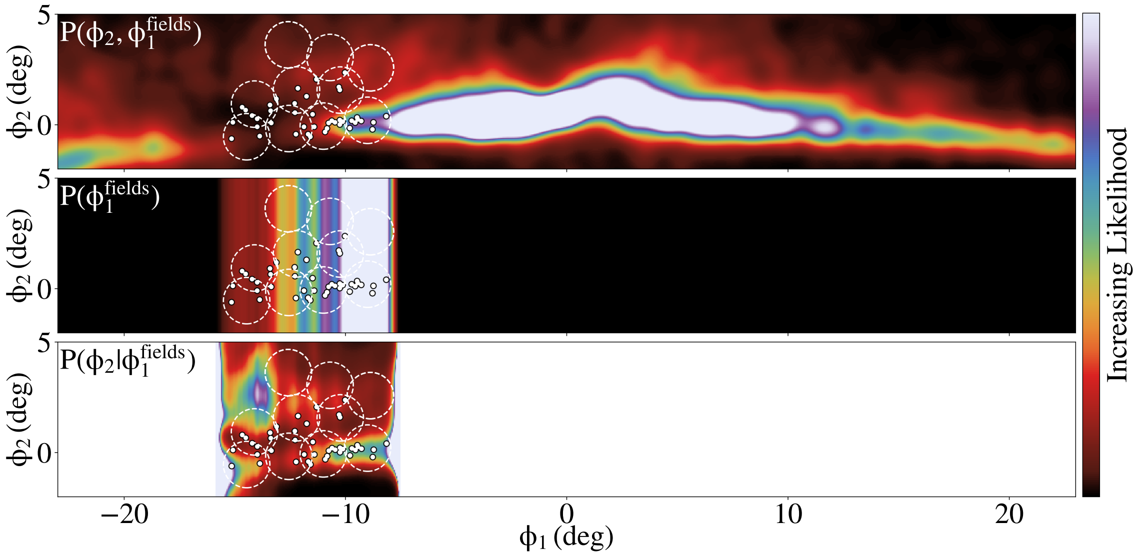

Figure 3.14: The same as Figure 3.2 but for one of our MCMC fits. The spread of the data highlights how there are no regions in $P(\phi_2|\phi_1^{\mathrm{fields}})$ which would return very low likelihoods.

data. This tends to balance out to higher likelihoods in the kink compared to the above 2 scenarios.

The higher stream width in the MCMC fits gives rise to higher likelihoods along the rest of the track as well, simply due to the larger errors compared to the extremely small stream widths seen in the 2 example scenarios we presented in section 3.5. This is made very apparent in Figure 3.15, where the stream width does not drop below ~ 0.4 deg anywhere along the stream, compared to the ~ 0.1 deg seen in Figures 3.5 and 3.8. A similar behaviour is present in the radial velocities as well. Outside the kink region and into the ATLAS part of the stream, the velocity dispersion is roughly $\sim 0.5\,\mathrm{km\,s^{-1}}$ for the 2 main scenarios, compared to $\sim 1\,\mathrm{km\,s^{-1}}$ at the MCMC fit example. The stream width and velocity dispersion at the kink for the MCMC fit however is similar in the case of the width, and lower for velocity dispersion than Figure 3.5. Due to the application of the KDE and only very local stars to the AAU data affecting likelihood, this does not necessarily have as significant an effect on the likelihoods as the likelihood estimation through ϕ_1 bins only for the regions outside the kink, hence why MCMC fits such as this still return higher likelihoods.

Given the findings above, we believe the incorporation of the stream width and radial velocity dispersion, along with density into the likelihood estimation would likely improve the fitting for the AAU stream. The former will obviously be able to punish the likelihood for the MCMC fit in Figure 3.15, even if we only apply this to regions outside the kink to not severely affect fits such as Figure 3.5 which otherwise has fairly narrow stream widths. The density meanwhile, would be harder to implement with our current stream generation method, and how the growth of streams remains roughly constant throughout integration.

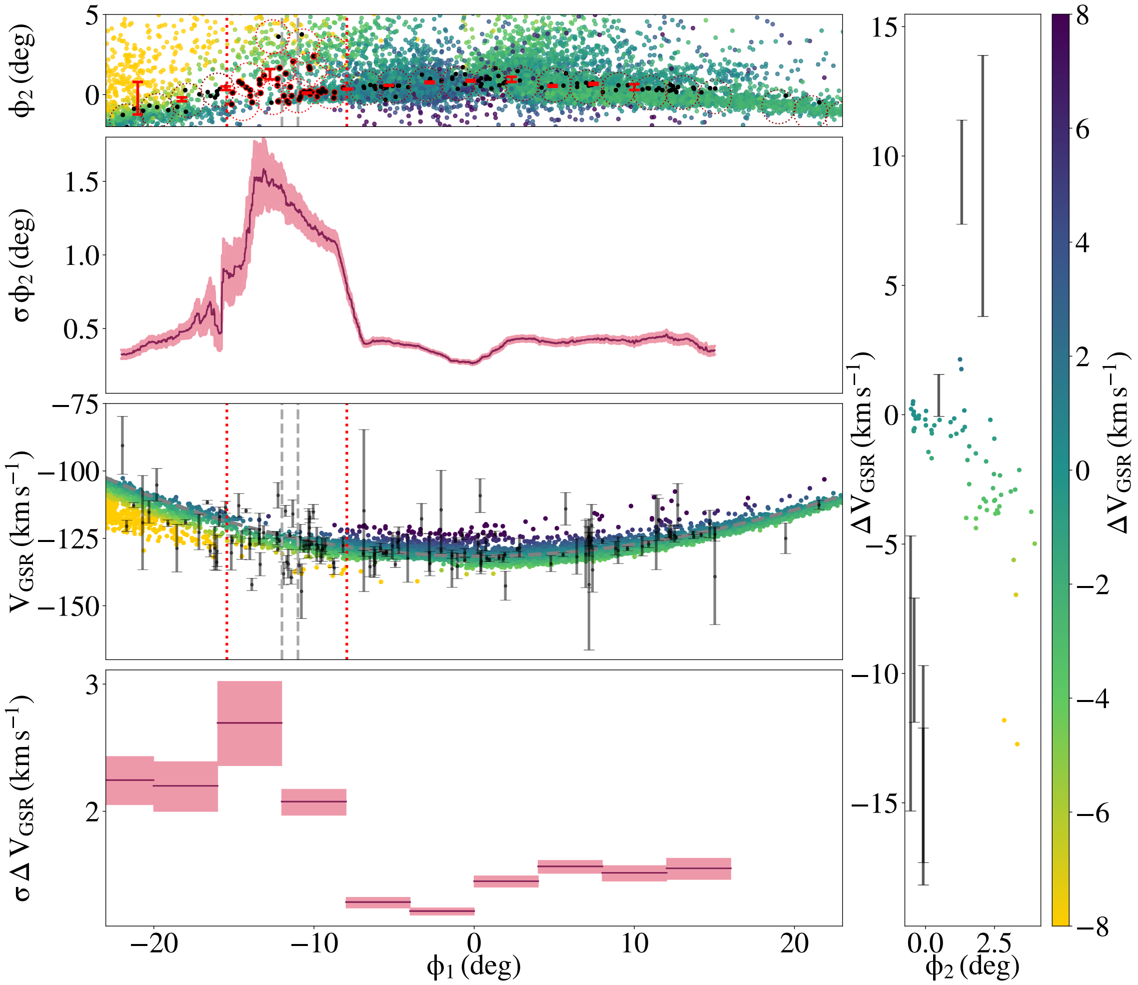

Figure 3.15: The same plot as 3.5 but for one of our MCMC fits. Different limits are used for the stream width and the velocity dispersion, due to the significantly higher values of these compared to the other qualitative fits. The drop in stream width outside the kink is simply due to the fact that the region the stream width is determined is still restricted to only the fields in the red dotted circles along the stream track.

Additional parameter exploration

For our fits here, we varied 8 parameters, all of which are used as key parameters to define the subhalo stream encounter. This does not include the progenitor properties of the AAU stream and hence, these have remained fixed alongside the background MW and LMC potentials. Effectively, we are attempting to fit the AAU stream for only one specific progenitor, making the assumption these progenitor properties must match AAU. While this had been considered for these fits, the rate at which fits were being performed in Chapter 2 given the convergence times as well would, with the current quality of data, take longer than the time allowed during this research. Likewise, a time dependent potential for the MW and LMC, while formerly demonstrated to have major impacts on orbits of streams such as the OC stream, would also considerably add to the computation time (Lilleengen et al., 2023).

Additional parameters relating to the progenitor carry a myriad of benefits on the fits. The most direct affect would relate to the stream width, which as explained above would benefit the likelihood estimation if it were included, with some fits benefitting from either a slightly thicker or thinner width. Additionally, the fit shown in Figure 3.5 appears to deviate from the data. At $\phi_1 > 15$ deg there are few observed AAU stars present here, but improvements to it may reveal real data of the stream that sits far above with a different arc in sky positions. This is all aspects of the model stream that would be able to be fixed by modifying progenitor properties, however for simplicity and bearing in mind computation times we chose to fix these.

3.7 Conclusions

We attempted to fit and recover properties of an AAU perturber. This process involved running a series of different statistical samplers, including EMCEE, dynesty and Scipy function Differential Evolution to explore potential stream-subhalo interactions that could fit the AAU stream. While the original plan was to achieve a quantitative fit of the stream, difficulties in optimising the likelihood estimation lead to issues fitting the perturber using all of EMCEE, dynesty and Differential Evolution. We still show 2 qualitative fits involving highly different mechanisms of producing the AAU kink. These include a recent impact from a heavier, denser subhalo directly onto where the kink is, along with a significantly older on the leading end of the stream, where the perturbed stars then drift down into the kink region. We list the main conclusions below:

- Additional observations to AAU reveal a more complex kink than what was formerly seen in Li et al. (2021). The kink, previously appearing as one continuous track along the stream, now appears to show 2 heavily overlapping tracks over a few deg in ϕ_1. Additionally, the AAU data combined with what we were able to produce from our stream-subhalo interactions implies the need for simultaneously a recent impact when studying kinematics, to create a steep enough velocity feature across the kink, along with an older impact when focusing on morphology to get the correct estimates on stream width.

- A far more robust likelihood estimation is needed to accurately fit the AAU stream. This result is partially due to the improvements in the data, and part of the estimation likely requires better data to incorporate details such as the stream width. It would also greatly benefit from the density of the stream to make for a more accurate use of a KDE in the estimation which does not punish less dense regions in the kink such as our fit using a very old subhalo impact

• Additional parameters should be used in MCMC samplers to fit the kink, particularly on the progenitor properties, to account for the ranges in stream width and velocity dispersion in the AAU data, along with time dependent MC and LMC potentials which could alter the orientation of the stream further. Using only one progenitor for all our fits was partially done due to time constraints, though it is clear now this may be necessary to better match the features in the track especially as data for AAU improves.

• Nonetheless, we have demonstrated some unique ways subhalo-stream encounters can appear in observations, particularly with how very old impacts can produce convincing spur like features in streams by allowing perturbed stars to drift down. The morphology and kinematics of the AAU stream also can help decipher the nature of an impact that would be needed to fit both the AAU kink, and other perturbed streams we may be yet to observe.

Looking forward, this work demonstrates how the complex morphology of the AAU stream requires more sophisticated modelling techniques, alongside likelihood estimation for future fits. Furthermore, having a broad view of the stream is also critical to understand the different impact scenarios and discerning whether we are dealing with a more recent or older subhalo impact, assuming we are still dealing with a subhalo-stream encounter. Upcoming surveys such as 4MOST (de Jong et al., 2012), LSST (Ivezić et al., 2019) and DESI (DESI Collaboration et al., 2016a,b) will be able to measure the stream morphology out to larger distances from the stream, ultimately helping us to understand how the stream was perturbed.

Chapter 4

An exploration of the baryonic candidates of AAU

In this chapter, we demonstrate the effects of some baryonic perturbers on the AAU kink. This serves two purposes, both to further show how the kink is unlikely to be the sole result of baryonic structure in the disk, but also to see if these may have smaller effects affecting the whole stream which may affect the subhalo fits attempted above. In Chapter 3, we discussed how we did not change the progenitor properties, and implementing this into fits could have minor affects on the curvature of the stream track, radial velocities etc. If baryonic structure in the disk is able to do this to the AAU stream too, this could add another layer of complexity on attempting to fit a subhalo-stream interaction to the AAU kink. The work outlined here includes my contributions to Li et al. (2021), titled *Broken into Pieces: ATLAS and Aliqa Uma as One Single Stream*. Specifically, my work below on spiral structure relates to what I performed for that publication. We additionally implement a more realistic bar potential below compared to what was in Li et al. (2021), with a different set of default MW parameters. Finally, in line with our previous chapters, we carry out this analysis on the heavier progenitors to generate a thicker stream which better matches the expanded AAU data than what was in Li et al. (2021).

4.1 Perturbations from the disk

The work from Li et al. (2021) demonstrated how a stream generated in a MW like potential alongside the LMC, with background the same as in Chapter 2, could provide a reasonable fit to the AAU stream. This was the first fit performed on AAU, since it was formerly regarded as two separate streams (Shipp et al., 2018), and the ϕ_2 positions could be well constrained when fitting to just the ATLAS part of the stream ($\phi_1 \geq -13$ deg). This analysis included implementation of various baryonic candidates such as GMCs, bars and spiral structure. Each of these have proven to result in gaps forming in other streams, the most well known examples being Palomar 5 and Ophiuchus, and this is usually from the pericentric passage of a stream aligning with the orbits of these objects (Price-Whelan et al., 2016; Amorisco et al., 2016; Hattori et al., 2016; Pearson et al., 2017; Banik & Bovy, 2019). For AAU however, the only one candidate capable of recreating a kink like feature and fitting the Aliqa-Uma portion of the stream is Sagittarius (Li et al., 2021).

We perform similar analysis to Li et al. (2021) to the new AAU data, and compared to their work we now model the stream slightly differently using the higher mass progenitor for a larger velocity dispersion. As explained in Chapter 1, the 3 main baryonic features of the MW disk that could perturb stellar streams include the Galactic bar, spiral structure and GMCs. We focus on the bar and spirals below due to their significantly higher masses than GMCs, which given AAU does not have such close encounters to the disk, would be more likely to have an effect on the stream than GMCs.

The introduction of these structures to stream generation is rather simple as we simply add individually either a bar, or spiral structure to the background potential. By adding these to the background, this also means that when integrating the stream progenitor backwards this will also be in the presence of these objects. Since we are not attempting to use these to directly fit the AAU kink with a subhalo, instead to just perform a more broad exploration of their capabilities on the AAU stream as a whole, there is no inclusion of a subhalo. Outside of that, the stream generation and background potential is largely the same as in previous chapters and specifically as described in Section 1.4.1. The implementation of the bar however did require minor modifications to the background as we explain below.

4.1.1 Spiral Structure using the Cox & Gomez potential

In order to assess the impact of spiral arms, we follow largely the same procedure as Banik & Bovy (2019). Namely, we use the analytical spiral arm potential from Cox & Gómez (2002) and implement it following a sinusoidal density distribution. In addition, the magnitude of the density of this potential has exponential dropoff with radius, which follows the similar dropoff seen within the disk. This profile, with effectively an equal negative density in the inter-arm regions, results in a net density of zero when averaged over the galactic disk. The spiral arms occupy 50% of the disk, meanwhile, the negative density inter-arm regions occupy the other half, resulting in a total change in mass of 0. The density profile of this potential is shown in Figure 4.2. The expectation is that at sufficiently long distances, there no net change in forces even though it changes the density distribution through the disk. This also allows it to very easily be implemented in any galaxy potentials due to no change in in enclosed mass accross the whole disk. The potential is defined by the following:

$$\Phi_s(R, \phi, z, t) = \frac{A}{R_s K D} \cos \gamma_s \left[\text{sech} \frac{Kz}{\beta} \right]^{\beta} \tag{4.1}$$

where K, β, D and γ_s are themselves, functions of R, ϕ and t. They are defined as follows below:

$$K(R) = \frac{2}{R \sin p} \tag{4.2}$$

$$\beta(R) = K(R) h_s (1 + 0.4 K(R) h_s) \tag{4.3}$$

$$D(R) = \frac{1 + K(R) h_s + 0.3 [K(R) h_s]^2}{1 + 0.3 K(R) h_s} \tag{4.4}$$

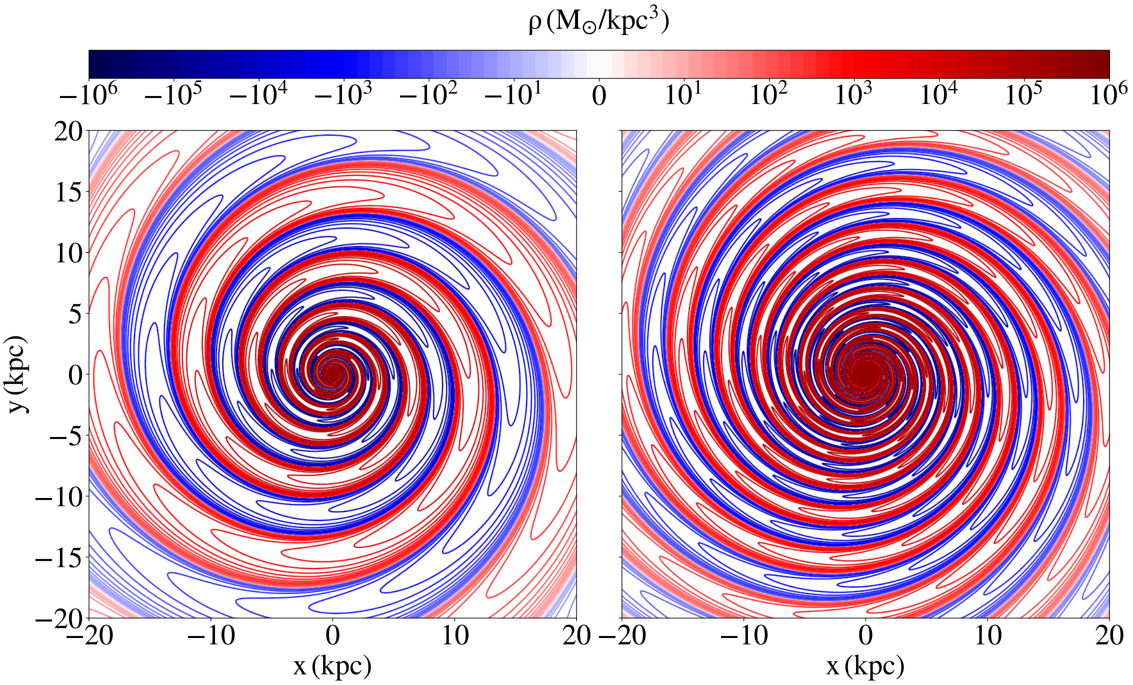

Figure 4.1: A face-on view of the resulting Cox & Gomez spiral potential used to recreate Milky Way like spirals for our fits. Left is a 2-armed spiral and right is a 4-armed spiral mode. Both share a radial scale length of 3 kpc, vertical scale height of 0.3 kpc, pattern speed of 22 $\mathrm{km\,s^{-1}\,kpc^{-1}}$ and a constant pitch angle of 9.9°. The spiral amplitude was chosen such that at 8kpc, their potential accounts for 1% of the total background disk potential, equal to 345 $\mathrm{km^2\,s^{-2}}$. The negative densities of this spiral potential are present to make the mean density 0, allowing it to be included in any galaxy potential without modifying the mass.

$$\gamma_s(R,\phi,t) = 2\left[\phi - \phi_s - \Omega_s t + \frac{\ln R/R_s}{\tan p}\right] \tag{4.5}$$

Here, A, governs the amplitude of the spirals (maintaining equally negative density in the inter-arm regions), $\mathrm{R_s}$ is the radial scale-length of the potential and reference radius for the angle of the spirals, $\mathrm{h_s}$ is the vertical scale-height and p is the pitch angle.

My implementation of spiral structure into stream generation used spirals following Monari et al. (2016). This involves tightly wound spirals with a constant pitch angle of 9.9 deg, with amplitude chosen such that the maximum force an object at 8 kpc from the Galactic center would receive from spiral arms is 1% of the force it would experience from the disk at that distance. This amplitude is determined using spirals arms with scale lengths and heights of 3 kpc and 0.3 kpc respectively, as used by Banik & Bovy (2019), and the exact amplitude used here is 345 $\mathrm{km^2\,s^{-2}}$. While we fix these parameters which define the instantaneous spiral potential, we modify the pattern speed to see how this may affect stream generation. We use a grid of pattern speeds ranging from Ω_{spiral} = 10 to 34 $\mathrm{km\,s^{-1}\,kpc^{-1}}$ in steps of

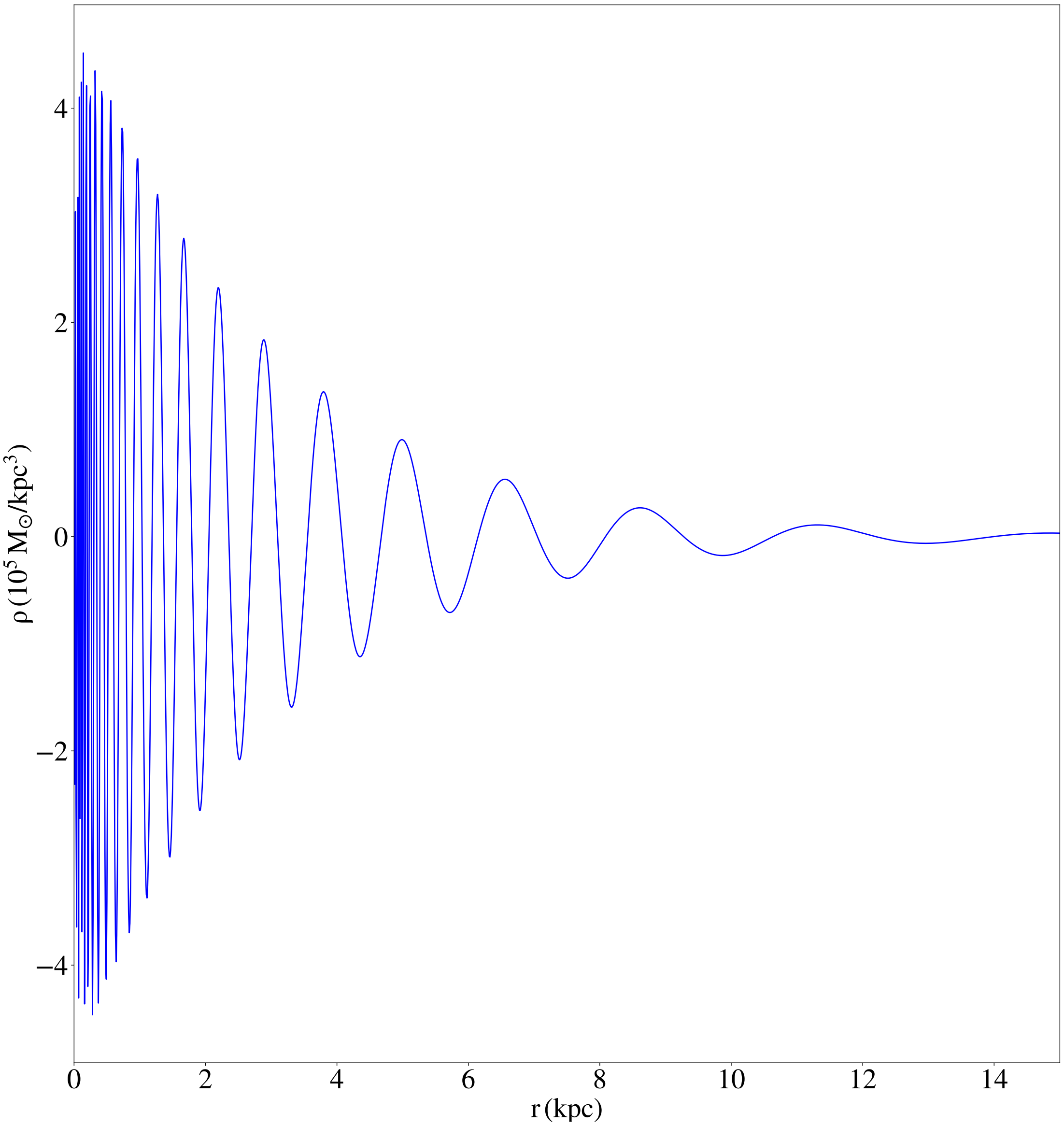

Figure 4.2: The density of the Cox & Gomez spiral potential along a line from the Galactic centre, showing the radial density profile. This demonstrates the exponential decay of the spiral density with radius and how this potential with the negative density inter-arm regions results in no net change in the enclosed disk mass.

$\Omega_{\rm spiral} = 3\,{\rm km\,s^{-1}\,kpc^{-1}}$. Furthermore, we consider both 2 armed and 4 armed spirals, as shown in Figure 4.1. As stated previously, 2 armed spirals are believed to be the closest match to MW spiral structure, with the disk beyond the bar dominated by the Scutum-Centaurus and Perseus arms (Benjamin et al., 2005; Churchwell et al., 2009). The 4-armed spirals result in a smoother potential on average, particularly for the longer distances between AAU and the MW disk, so we would expect smaller perturbations. With this in mind, we nonetheless consider a fiducial setup with a pattern speed of $\Omega_{\rm spiral} = 1000\,{\rm km\,s^{-1}kpc^{-1}}$ to account for any smooth change to the potential due to the spirals. Due to the nature of this potential and our spiral arm numbers, we therefore assume a grand design dominated disk and do not consider any potential transition to a flocculent nature in the outer disk. Flocculent spiral arms would result in a more smooth potential compared to these 2 and 4-armed Cox & Gomez spirals, so our implementation is likely to give rise to slightly stronger perturbations.

4.1.2 Galactic bars using the McGough potential

The exploration of the bar in Li et al. (2021) had utilised the Long & Murali bar (Long & Murali, 1992), however, we seek to update from this and use a new more accurate bar model. Here, we instead use the McGough bar, which serves as an expansion of the widely used Long & Murali bar. This bar features a density profile that more closely resembles the Milky Way compared to previous models. This includes an exponentially falling density along the bar major axis, and a Gaussian density distribution for the fall of density along the bar minor axis (McGough et al., 2020). The Long & Murali bar instead had the minor axis falloff following a Plummer sphere. The density profiles of a typical McGough bar following MW bar parameters is shown in Figure 4.4. The equation for the potential is as follows:

$$\Phi_{bar} = -\frac{GM}{2b(1-e^{-a/b})}\int_0^1 H_{conv}(x,y,z)\,dm \tag{4.6}$$

where

$$H_{conv} = \sqrt{\frac{1}{m^2(1-m^2\epsilon^2)}}E(m,y,z)F_s(m,x) \tag{4.7}$$

and

$$E(m,y,z) = \exp\left[-\frac{m^2y^2}{2\sigma^2} - \frac{m^2z^2}{2\sigma^2(1-m^2\epsilon^2)} + \frac{\sigma^2}{2b^2m^2}\right] \tag{4.8}$$

$$F_s(m,x) = e^{-\frac{x}{b}}\left(\mathrm{erf}\left(\frac{bm^2(a-x)+\sigma^2}{\sqrt{2}bm\sigma}\right) - \mathrm{erf}\left(\frac{-bm^2x+\sigma^2}{\sqrt{2}bm\sigma}\right)\right) \tag{4.9}$$

The main bar parameters that define the shape of the bar are a, b, σ and ϵ. Here, a represents the length of the bar, b controls its flatness along the major axis, σ is the overall length scale and variance of the underlying Gaussian density and ϵ the bar's flattening

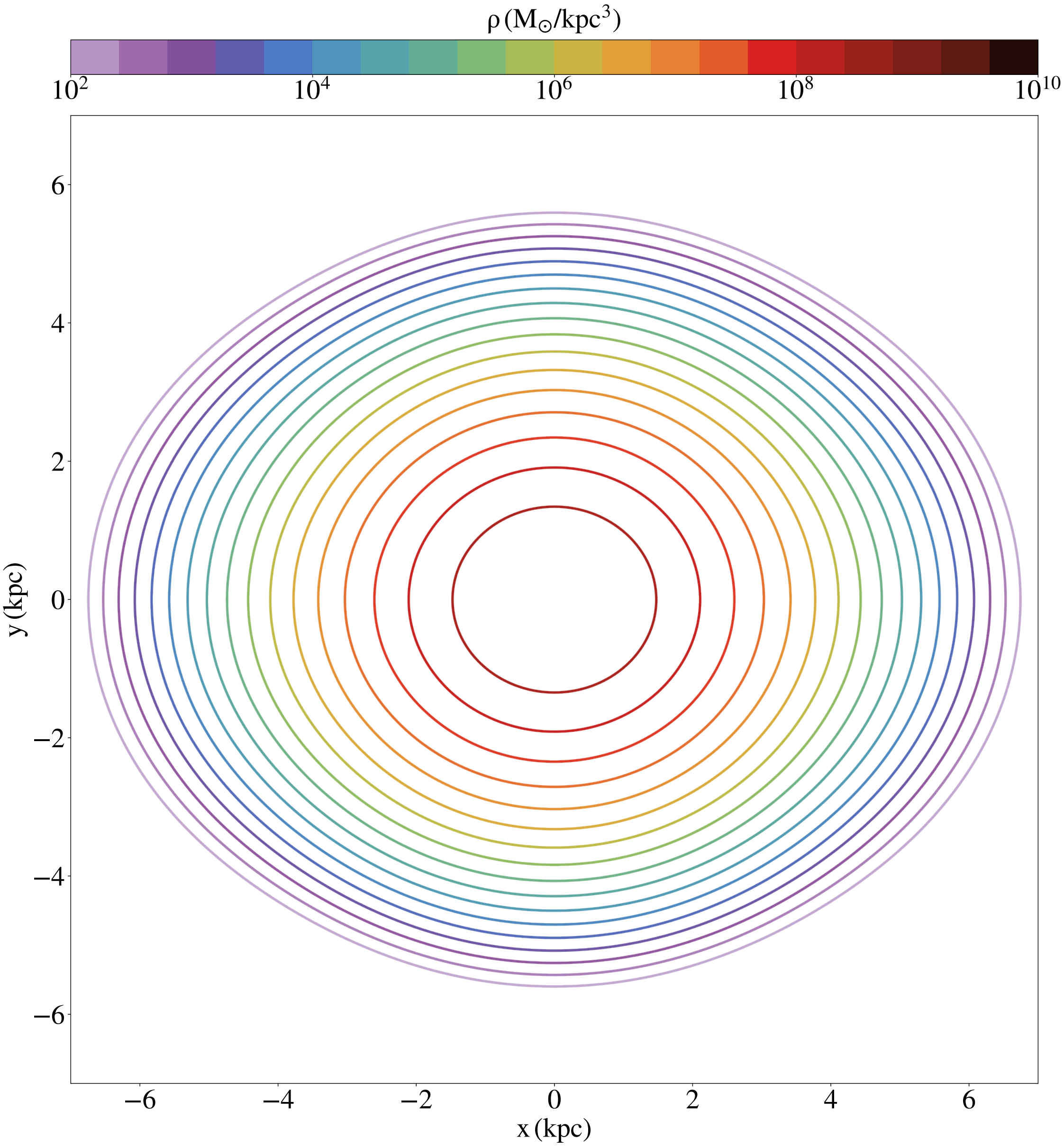

Figure 4.3: A face-on view of the resulting McGough bar potential used to recreate a more accurate MW like bar for our fits. This bar is defined by the following parameters: bar length, $a = 2.89\,\mathrm{kpc}$; flatness along bar, $b = 0.35$; overall length scale and variance of the underlying Gaussian, $\sigma = 1$; vertical flattening in z, $\epsilon = 0.37$. Further parameters include a bar orientation of 33 deg and pattern speed of $41\,\mathrm{km\,s^{-1}\,kpc^{-1}}$. These parameters that were used here are the parameters in McGough et al. (2020) to match the simulations of Sanders et al. (2019) which itself, matches the MW bar well. Note that the scale of densities in this figure is different to in figures 4.1 and 4.2. This bar only has positive density, and these reach 4 orders of magnitude higher than spiral structure.

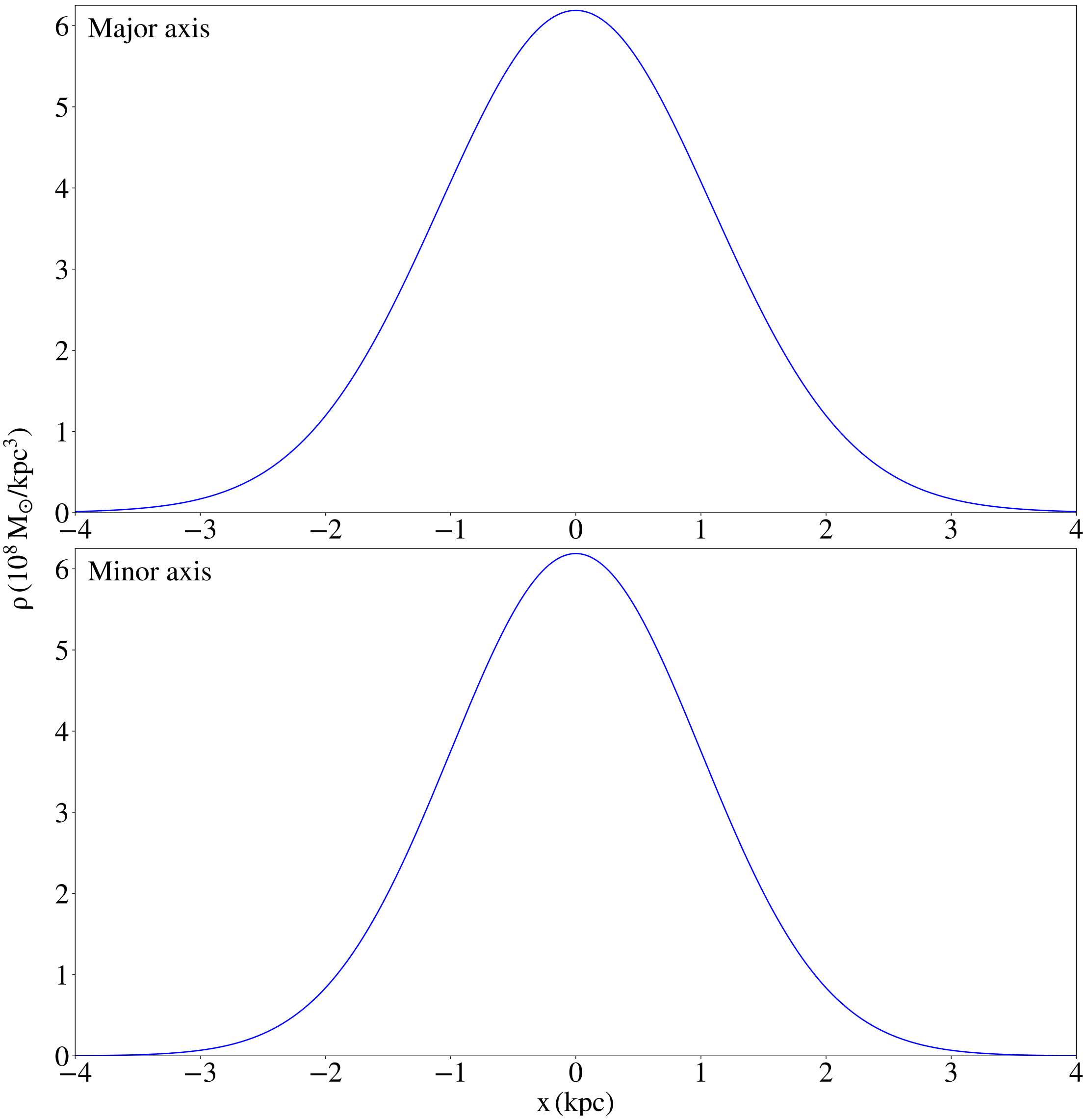

Figure 4.4: The densities of the McGough bar along a cross section of both its major axis, governing the length of the bar, and minor axis, its width. The parameters used here are the same as in Figure 4.3.

in the z axis. Note that compared to the Long & Murali bar, the bar minor axis isn't parameterised, instead, being the result of a combination of ϵ and σ. The full range of different bars that can be produced using this model is very diverse, and the full effects of modifying these parameters can be further explored in McGough et al. (2020).

As explained in their work, the potential above required a mixed approach of both an analytic and numerical solution. This is required at the lower limit of the integral as $\mathrm{m} \rightarrow 0$. As a result, the integral in equation 4.6 is split at the value $\mathrm{m} = \mathrm{Osc}(\sigma, \mathrm{b})$, where $\mathrm{Osc}(\sigma, \mathrm{b})$ defines the onset of numerical stability as $\mathrm{m} \rightarrow 0$. We now end up with 2 integrals, the first which can be solved with an analytic solution between $\mathrm{Osc}(\sigma, \mathrm{b})$ and 1, and the second requiring a numerical solution on a Taylor expansion of it between 0 and $\mathrm{Osc}(\sigma, \mathrm{b})$. In order to provide a conservative switchover point to avoid null results in the integration, $\mathrm{Osc}(\sigma, \mathrm{b})$ is slightly overestimated and is defined as follows:

$$Osc(\sigma, b) = 0.2\frac{\sigma}{b} \tag{4.10}$$

Solving the numerical solution to this integral is then done using Gauss-Legendre quadrature (Abramowitz & Stegun, 1972). The amount of steps within this integral will affect how accurate the result is, alongside the order of the Taylor expansion. We are able to investigate this, and follow the approach from McGough et al. (2020) by use of Poisson's equation:

$$\nabla \cdot F_{bar} = -4\pi G \rho_{bar} \tag{4.11}$$

The very long distances of AAU compared to the MW centre mean we needed to use higher order Taylor expansions and steps within each numerical solution using quadrature. For all our bar models, we use 7th order Taylor expansions, and each numerical solution to the integral is determined using 100 steps. This was determined by using Poisson's equation for force calculations at a distance of 50 kpc from the Galactic centre. Given the apocenter of AAU is $\sim$ 41 kpc, this provides a far enough safety net to account for any particles that go beyond this distance (Li et al., 2021). The thickness of the stream may cause particles to be slightly further than the apocentric distance, and the disk structures may alter the orbit itself to slightly further distances too, but we deem it unlikely to change orbits enough to account for an extra $\sim$ 9 kpc.

Our bar largely follows the same parameters used in McGough et al. (2020) to set up a MW like bar using their model, and we show a face-on view of this potential in figure 4.3. Their parameters were chosen specifically to match the bar in the simulations of Sanders et al. (2019), which were found to be accurate MW models in line with past work (Wegg et al., 2015; Hattori et al., 2016; Erkal et al., 2017; Portail et al., 2017b; Bovy et al., 2019). This consists of a bar of mass $\mathrm{M_{bar}} = 10^{10}\mathrm{M_{\odot}}$, with $\mathrm{a} = 3\mathrm{kpc}$, $\mathrm{b} = 0.35$, $\sigma = 1$ and $\epsilon = 0.37$. Additionally, the bar orientation is 33 deg and its pattern speed is $41\,\mathrm{km\,s^{-1}\,kpc^{-1}}$. This represents a bar leaning more towards the longer and more slowly rotating end (Sanders et al., 2019). Similar to our methods for spiral structure, we still explore a range of pattern speeds for the bar while keeping most parameters which define the instantaneous potential the same. In this case, our pattern speed ranges from $\Omega_{\mathrm{bar}} = 21$ to $61\,\mathrm{km\,s^{-1}\,kpc^{-1}}$ in steps of $\Omega_{\mathrm{bar}} = 5\,\mathrm{km\,s^{-1}\,kpc^{-1}}$. Since implementing the bar potential is effectively adding mass to the potential unlike the spiral potential, we also subtract this mass from the disk potential to maintain the same total background mass. Similar to spiral structure, since the bar slightly changes the mass distribution of the Milky Way potential, we compare these streams with a fiducial setup involving rapidly rotating bar with pattern speed $\Omega_{\rm bar} = 1000\,{\rm km\,s^{-1}\,kpc^{-1}}$. These pattern speeds are fast enough that we expect both the bar and spiral effect to be smoothed out.

4.2 Results & Discussion

In order to understand how the bar and spiral arms can affect the AAU stream, we follow Li et al. (2021) and look at how the observables of the stream change compared to an unperturbed model. In particular, we will look at stream observables including the stream track, widths, alongside the radial velocities and dispersions, highlighting most of the properties in figures 3.5, 3.8, 3.15 in Chapter 3. We focus on the stream track and radial velocity since these are the best measured. In contrast, the proper motions are not well constrained enough to see smaller scale perturbations in proper motions as evidenced in Chapter 3. It has already been reasonably established that the bar and spiral structure would not be able to produce the AAU kink, so while we seek to prove this remains the case for the new bar model, we are also more concerned with if they can make any significant changes in the track orientation, width and velocity dispersion for our AAU fits. This would in turn affect how much these baryonic structures will need to be considered for future fits. As part of this, the stream width and velocity dispersion is no longer restricted to stars only within the AAU fields, and we use all stars along the track. Using these, we highlight one pattern speed for each of the bar and spiral structure, in the case of the spirals representing a more extreme value approximately 50% faster rotating than typical MW estimates. We compare these to streams generated both in their respective fiducial setups, shown in Figure 4.6 for the spirals and Figure 4.8 for the bar.

It is important to note in these figures that due to how streams are generated as in chapter 1.4.1, there is a considerable dip in stream width at the progenitor for all these unperturbed models. This is simply due to how the stream generation works, as the perturbed stars are injected at the progenitor's Lagrange points, which later will move to different radii and drift. By the end of stream generation, the progenitor mass tends towards zero and so does the tidal radius and distance between Lagrange points. This results in a thinner stream.

4.2.1 Spiral structure

The fastest spiral arm here was chosen due to having the most clear difference to the fiducial setup in Figure 4.6. This is made from a 2-armed spiral with the fastest pattern speed in our grid of parameters, where $\Omega_{\rm spiral} = 34\,{\rm km\,s^{-1}\,kpc^{-1}}$. We additionally show the maximum differences in stream track, velocities and dispersions between both the 2 and 4-armed spirals, along with their 9 sampled pattern speeds to fiducial setup in Figure 4.7.

Differences in the stream track and velocities between these spirals is rather minimal, with maximum differences of 0.1 deg seen in the faster rotating spirals. These differences in ϕ_2 values are significantly higher than our analysis performed in Li et al. (2021), though these

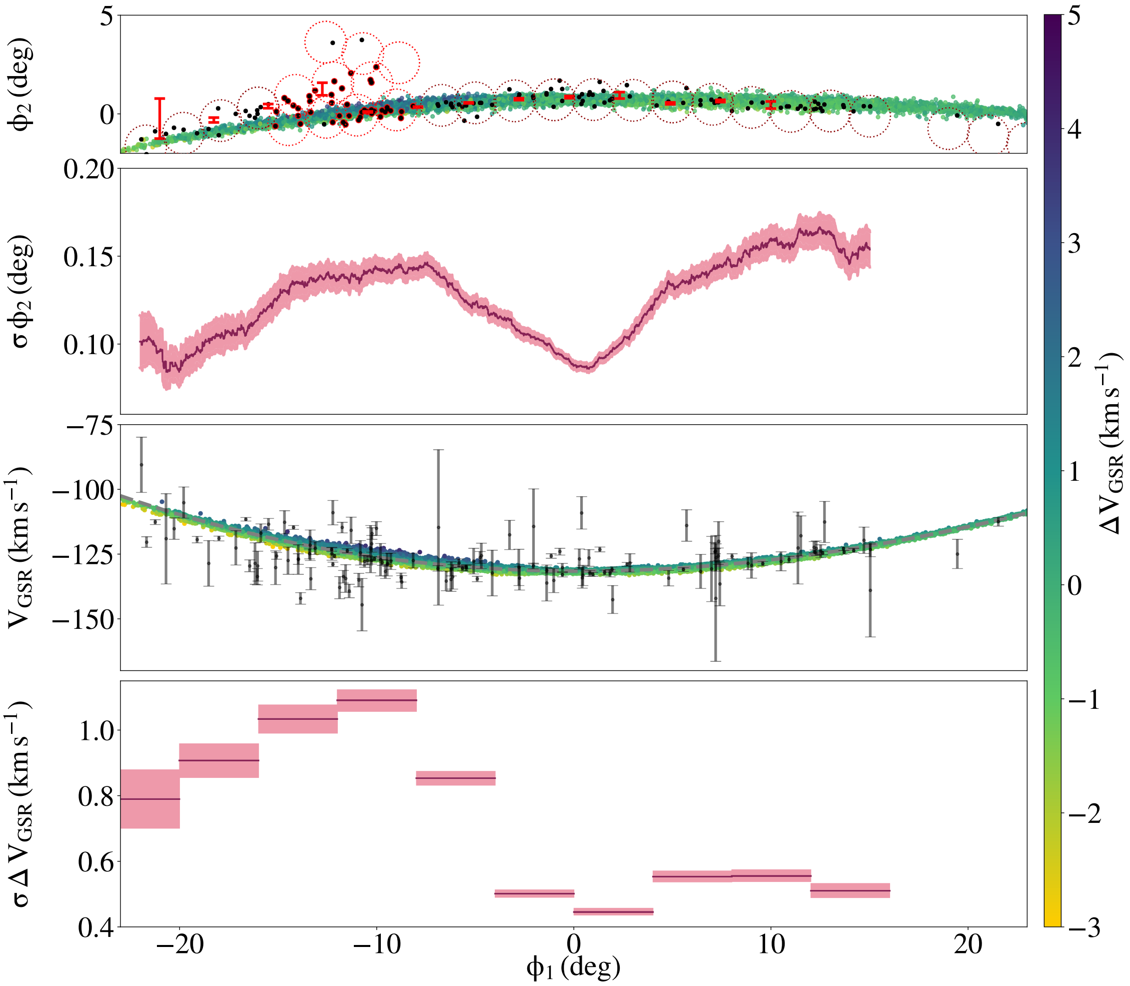

Figure 4.5: Stream track and radial velocity observables for fiducial stream model which is evolved in a MW without bar or spiral structure. Progenitor properties the same as those used when fitting subhalo-stream encounters. The plot follows the same layout as figure 3.5, with the exclusion of the right panel showing the gradient between V_{GSR} and ϕ_2 near the kink. Stars are coloured here by their V_{GSR} values relative to a polynomial fit to the radial velocities, explained further below. The top 2 panels are stream track and stream width. While the S5 fields are shown, they are not used for determining the width. The actual observed AAU stars are shown in black points, with those in the fields highlighted in red. Additionally, the spline fits along the AAU track are shown in red errorbars here. The shaded region above and below the stream widths here showcase the $1-\sigma$ uncertainties. The bottom 2 panels here meanwhile show the velocity V_{GSR} along this same stream, with the velocity dispersion on the bottom. We show the observed AAU data as grey errorbars here. The polynomial curve is fit to V_{GSR} as the dashed grey curve for this particular stream, with the same fit used in figures in Chapter 3 and the figures below. The velocity dispersion is shown here in 4 deg slices, and the shaded region here is used to show the $1-\sigma$ uncertainties.

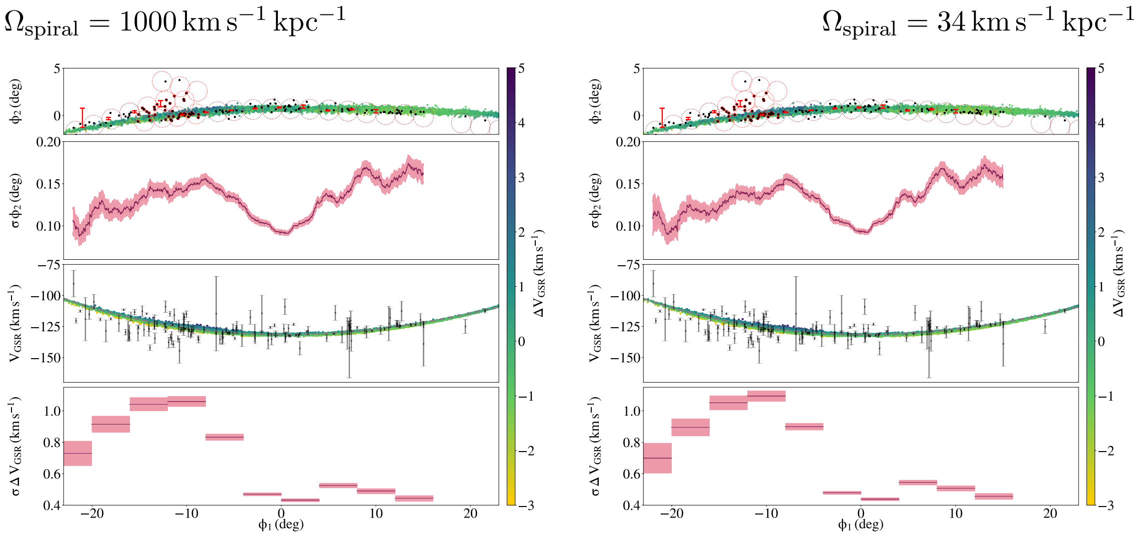
$\Omega_{\rm spiral} = 1000\,{\rm km\,s^{-1}\,kpc^{-1}}$

$\Omega_{\rm spiral} = 34\,{\rm km\,s^{-1}\,kpc^{-1}}$

Figure 4.6: Figures in the same style as figure 4.5, however for a stream generated in a 2-armed Cox & Gomez spiral arm potential (Cox & Gómez, 2002). Both have the pattern speed for the spiral arms shown above. The left figure showcases a fiducial setup to account for the modified density distribution in the disk by implementing the potential. The right features the fastest rotating spiral arms in the grid of parameters described in section 4.1.1. A slight change in the curvature of the stream can be seen from the location of the some peaks and troughs in the stream width between the fiducial setup and the spirals rotating with pattern speed $\Omega_{\rm spiral} = 34\,{\rm km\,s^{-1}\,kpc^{-1}}$. These are particularly apparently from the trough near $\phi_1 = -22$ deg shifting further up the stream to $\phi_1 = -20$ deg in for the figure on the right. Meanwhile, a peak in the left figure around $\phi_1 = 13$ deg has instead shifted down the stream to $\phi_1 = 12$ deg.

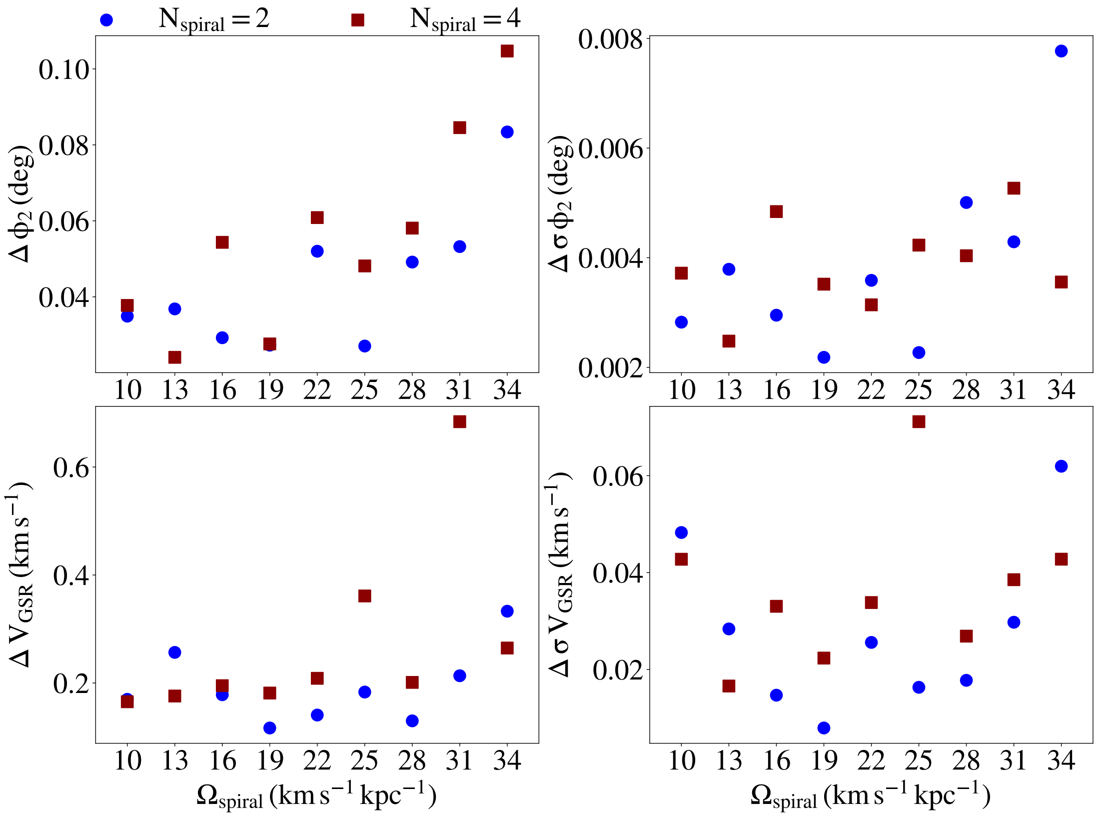

Figure 4.7: The differences seen between each of our spiral arm models to the fiducial setup. Each panel shows the maximum change between the spiral model and the fiducial setup for 4 different parameters, which include the track, ϕ_2, the width in the track $\sigma\,\phi_2$, the velocity V_{GSR} and dispersion $\sigma\,V_{GSR}$. Both the 2-armed and 4-armed spirals are shown here.

maximum differences tend to be at $\phi_1 < 20$ deg and $\phi_1 > 10$ deg. These are beyond the regions analysis was performed on the AAU stream in Li et al. (2021) due to how little data was available at these regions at the time.

Stream widths appear to have some faint but noticable changes with spiral structure as well. Once again this is most noticable compared to the fiducial setup at the higher pattern speeds, where in Figure 4.6 the stream widths are slightly noisier, with often higher error too. This does reasonably match the idea of how they introduce small density variations, which could in turn have small fluctuations along the stream track similar to what was found from the minor spiral arm effect in Li et al. (2021). These widths also highlight how pattern speed does appear to potentially play a role in the shape and curvature of the stream. When looking at the positions of the peaks and troughs for the stream width in Figure 4.6, most notably the dip in width at $\phi_1 = -22$ deg for the fiducial setup on the left, this is still present in the spirals on the right but shifted to $\phi_1 = -20$ deg. Meanwhile, peaks at positive ϕ_1 values very slightly shifted the opposite direction, from roughly $\phi_1 = 13$ deg to $\phi_1 = 12$ deg. The shape of the stream has almost compressed in a sense, likely resulting from a very minor change in the curvature. This does not appear for any other pattern speeds, so it is possible that this specific pattern speed could have lead to a alignment of a spiral with the stream pericenter, slightly altering the orbit of the progenitor.

The stream properties relating to $V_{\rm GSR}$ and its dispersion however are very unchanged between all spiral models. Given these very small changes across all observables in Figure 4.7, this also means the differences between the 4-armed model with the 2-armed has very little affect for the AAU stream. At the distances between the stream and spirals for most of the orbit of AAU, it is likely having different numbers of spirals will make little difference as their effect is more dependent on an alignment with the stream pericenter. Instead, streams with on average much closer orbits would better suit an exploration into the number of spirals.

4.2.2 Galactic bar

The results are of a McGough bar with pattern speed of $41\,\mathrm{km\,s^{-1}\,kpc^{-1}}$, shown in Figure 4.8. Like with the spiral structure, we also show the the maximum differences across all nine pattern speeds sampled to the fiducial model in figure 4.9.

The bar features significantly smaller variations in the stream track compared to spirals, with maximum differences ~ 0.02 deg. Between the bar models as well, there is very little variation, and in general the bar impact from the McGough bar has a far smaller impact that what the Long & Murali bar could previously do to the AAU stream, where in Li et al. (2021) the maximum changes in track were ~ 0.1 deg with a median change of ~ 0.03 deg. Likewise, the density variations of 25% that were found in Li et al. (2021) do not appear to be as prevalent here as there is almost no variation in stream widths.

The bar model in Figure 4.3 and Figure 4.4 do show a more spherical bar than the prior Long & Murali bar, which featured a set scale length and width of 3 kpc and 1 kpc respectively, but it is also possible that, similar to what could have happened with our faster spiral model in Figure 4.6, there were brief alignments of the bar and stream in pericenter

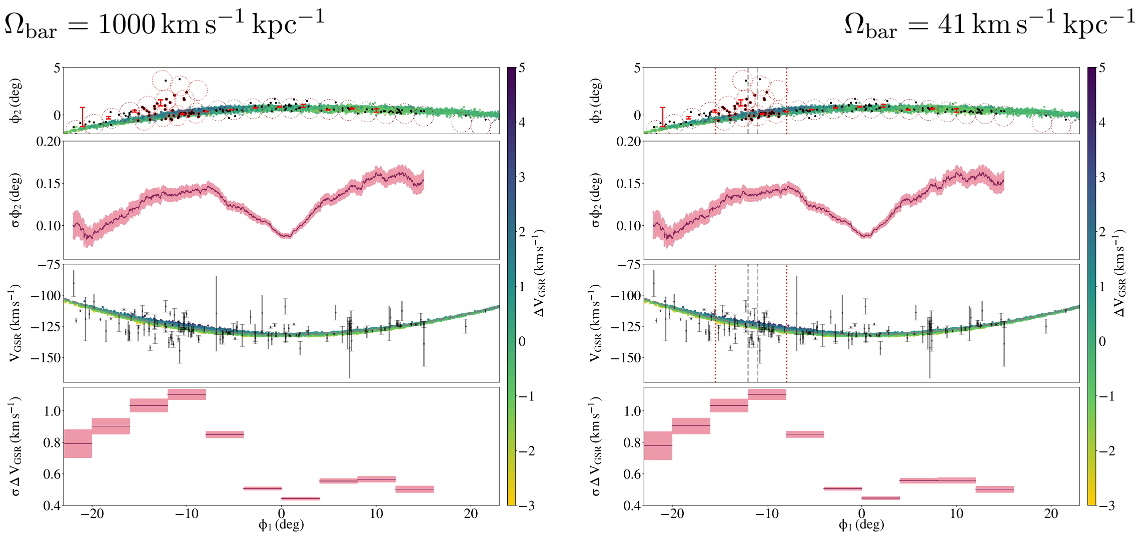
$\Omega_{\mathrm{bar}} = 1000\,\mathrm{km\,s^{-1}\,kpc^{-1}}$ $\Omega_{\mathrm{bar}} = 41\,\mathrm{km\,s^{-1}\,kpc^{-1}}$

Figure 4.8: Figures in the same style as figure 4.5, however for a stream generated in a McGough bar potential (McGough et al., 2020). Both have the pattern speed for the bar shown above. The left figure showcases a fiducial setup to account for the modified density distribution in the disk by implementing the potential. The right features a bar rotating with typical MW estimates from (Sanders et al., 2019).

which we did not have here. This has been shown previously such as in Hattori et al. (2016) that streams can be rendered shorter due to the torque on parts of the stream from these alignments. We are using a heavier progenitor here, and with how stream generation works by integrating backwards first to ensure the progenitor is at a chosen present day location, the heavier progenitor will be at a slightly different orbit to the previous work. Combined with the slightly different bar orientation and pattern speeds used, we may have simply not had any situation in our stream generation where these aligned to give rise to much more significant perturbations.

4.3 Conclusions

In line with the work of Li et al. (2021), we further continued analysis of the galactic bar and spiral structure on potential effects they have on the AAU stream. This includes observing effects on further stream properties such as the velocity dispersion. We performed comparisons with these structures of various pattern speeds about their generally accepted MW values to both a fit to the AAU stream in the presence of no spiral structure or galactic bar, along with additional fiducial setups of them with extremely high pattern speeds. This was done to see how both the pattern speeds of these structures can play an influence on the size of perturbations, along with how they changes to the density distribution in the disk, regardless of pattern speed, can alter stream properties. We also test a relatively new bar model by McGough et al. (2020) with a new set of parameters they use to match their model to recent simulations of MW like bars in Sanders et al. (2019).

Similar to the findings of Li et al. (2021), neither bar nor spiral structure was able to produce a substantial effect on the stream and thus cannot explain the kink. We however,

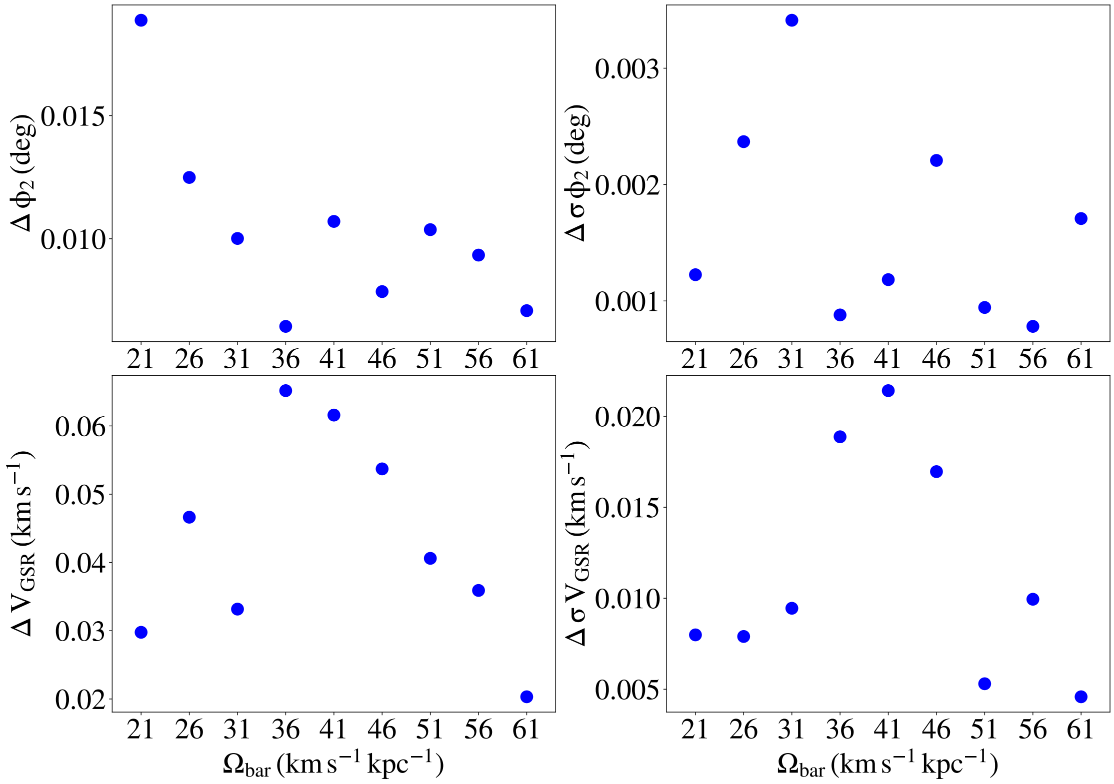

Figure 4.9: The differences seen between each of our bar models to the fiducial setup. Each panel shows the maximum change between the bar model and the fiducial setup for 4 different parameters, which include the track, ϕ_2, the width in the track $\sigma\,\phi_2$, the velocity $\mathrm{V}_{\mathrm{GSR}}$ and dispersion $\sigma\,\mathrm{V}_{\mathrm{GSR}}$.

did find that spiral structure could, on one specific pattern speed of of $34\,\mathrm{km\,s^{-1}\,kpc^{-1}}$ result in significantly larger differences to stream track than some previous findings. In ϕ_2 values, this does still only simply give very minimal changes of ~ 0.1 deg. Where it does appear more significant instead is in ϕ_1 values where there appear to be some considerable shifts in the variations of stream width by as much as 2 deg in ϕ_1. Since this only appeared for one pattern speed scenario, it is likely this happened to result in an alignment of the stream at pericenter with a spiral arm, resulting in a small relative spike in the forces experienced from the disk. For the McGough bar, a combination of a more spherical shape in its density and the possibility that there were no alignments with the stream during generation meant the effects of the bar were very smaller, less so than spiral structure. Further research into this, such as understanding the exact situation between the stream and either spiral or bar that gives rise to these effects along the track has interesting implication of better contraining their own properties as well by using stellar streams. For example, if a past orientation of a spiral arm could be determined from this, this could lead to novel constrains on the pattern speed if they could be linked to the current observed MW spirals. This would match findings of Hattori et al. (2016) with the Ophiuchus stream, and how it may be shorter due to alignments of parts of the stream with the bar. This could be extended to a larger sample of streams and in turn be used to then recover bar and spiral parameters.

4.3.1 Use of the McGough bar

For the McGough bar, we note that due to the nature of this potential and the numerical solution using Gauss-Legendre Quadrature, generating streams in this potential becomes dramatically more computationally intensive. Typically, generating a stream in completed in a matter of minutes, while the inclusion of this bar raises the duration to up to several hours, increasing the total calculation time by as much as 2 orders of magnitude. When we additionally consider that the subhalo encounters require generation of a stream twice, once without a subhalo and once with it included, the time to carry out a subhalo-stream encounter in the presence of this bar could as much as double. Given the issues reaching convergence for our MCMCs in chapter 3, along with the fact we already have explained the need for additional parameters in the fits, this would make fitting encounters to the AAU stream with this bar infeasible.

We do note that part of these issues with the computational time lie with the large distances between AAU and the bar, and how this requires higher order Taylor expansions and steps in our Gauss-Legendre quadrature. It is possible that the calculation times for streams with far lower radii are far more reasonable and would not increase the calculation time so dramatically. Adding a dependence on the steps in the Gauss-Legendre quadrature calculation and order of the Taylor expansion, with the distance of the particle, could potentially also have sped up the fits here. Given the pericenter of AAU lies at $\sim$ 13.3 kpc, calculations at these shorter distances will be able to use Taylor expansions only to the third order, with 20 instead of 100 steps in the numerical solutions to the integral. The Taylor expansion in particular gets extremely long at the 6th and 7th order terms and removing these will no doubt improve computation times.

Chapter 5

Conclusions

In this thesis, I explored the nature of stellar streams and perturbations to them, particularly how dark matter substructure can influence how they look today from prior encounters. The main focus was the ATLAS-Aliqa Uma (AAU) stream, with its most striking feature the kink which sees a change in track as much as 2 deg perpendicular to the stream, and one which currently has no obvious baryonic candidate for reproducing it (Li et al., 2021). This makes a stream-subhalo interaction an excellent candidate, and I sought to explore how it could be possible to fit this encounter, hence, recovering properties of the subhalo itself which could lead to more constraints on the dark matter particle candidate. The key results for each chapter are highlighted below:

I was able to demonstrate using mock observables of streams in N-body simulations that subhalo properties could be recovered from a perturbed stellar stream, including when the encounter took place, the subhalo mass and its scale radius, and its kinematics which could allow its sky positions to be determined. This used streams in a more realistic scenario of generating stellar streams in elliptical orbits and in the presence of a subhalo throughout the simulation, allowing for other encounters to take place before or after the predefined parameters. Furthermore, by generating these mock observables with different quality of data, I could see how the process of fitting these parameters may change in the future as data improves, while also demonstrating that present day observations of streams could still allow us to recover subhalo properties reasonably well. This demonstrates that in intuition from the analytic impulse approximation used in Erkal & Belokurov (2015b) can be extended to realistic streams on eccentric orbits. Additionally, on the context of stream features like the AAU kink, I also demonstrated how direct impacts will need to be recent as a result of generating the mock data.

Using the findings of chapter 2, I explored potential subhalo encounters to fit the ATLAS-Aliqa Uma stream. As part of this, I developed a more robust approach to determining the likelihood on stellar stream fits which better considers the 2-dimensional structure of the on-sky track to better tackle features such as the AAU kink. Part of this was due to the fact that after new data, the AAU kink is no longer a single shift in ϕ_2 along a continuous track, and instead could be a spur joining onto the stream from above. Nonetheless, I still found that fitting a feature such as this, especially with the new data requires more considerations than just the subhalo properties and the kinematics of the subhalo-stream encounter. Including the progenitor properties likely would make for a good first step as it can allow the stream width, velocity dispersions, on sky densities and the orientation of the track to be modified in fits. Finally, while some recent direct subhalo impacts could produce interesting qualitative results, I could also show that subhalo encounters that happen elsewhere on the stream, most notably further along the stream, could produce features similar to the AAU kink. Very old impacts can cause the perturbed stars to drift down the stream as they are pushed into higher radius orbits with longer time periods, and in some instances reconnect onto the stream as a second track or spur coming out of the stream. These two styles of subhalo encounters leave very different dynamic and morphological tracers in the stream, such as the very small radial velocity features of the old impacts which drift into the kink, though can give rise to large changes in the stream width where they connect to the stream. This could make for a good venture towards other stream fits, such as GD-1 which has a spur like feature on its track.

Finally, I explored some baryonic structure in the disk, the galactic bar and spiral structure and their effects to the AAU kink. With this, I had both further showed in line with contributions to Li et al. (2020) that the AAU kink cannot be produced from baryonic structure, and explored their effects on other stream properties such as the stream width and velocity dispersion. While they do have some minor effects even on streams such as AAU, with changes to the ϕ_2 positions of up to 0.1 deg, this is unlikely to be much influence to the stream track. Instead, where they can have more significant effects is by smaller scale changes to the orientation to the stream, most likely by past encounters with the stream progenitor, where if the progenitor has a small enough pericenter to be influenced by spirals or potentially even the bar, the orbit itself can be altered. This potentially makes them quite important to consider for fitting certain streams, as this effect of them could potentially influence progenitor properties. With more dedicated work towards the exact process that goes on during stream generation with these structures, it is possibly that streams could conversely be used to constrain past orientations of the bar and spiral structure.

5.1 Future work

Overall, stellar streams remain an excellent detector for measuring the properties of dark matter subhaloes. Much work still remains to be done to finalize the fits for the AAU stream and to fit other streams in the Milky Way, and this will remain a good path to take this research. Still, the main goal will be to try and obtain a quantitative fit the AAU kink and this will likely require the consideration of progenitor properties and modifying the MW potential. From there, we can constrain the present day positions of the subhalo and try and find baryonic candidates in this region or search for possible gamma ray emissions, which has recently seen use to detect subhaloes with a machine learning approach from Mirabal & Bonaca (2021). This has the potential to both provide additional evidence of dark matter, along with the provide novel constraints on the dark matter particle.

As observational data improves on streams, it also opens pathways to using them to study the MW potential further, including objects such as the Galactic bar and spirals. We would first aim to improve the bar and spiral models used for streams. Spirals will benefit from consideration of its more flocculent nature at the outer MW, and both them and the bar would benefit from implementing a more time dependent nature on their pattern speed and length (Quillen, 2002; Petersen et al., 2019; Hilmi et al., 2020). Still, the effect of these structures on streams proved to be quite promising when studying their radial velocities and dispersions, so a worthwhile endeavour could be to explore how reliably we could use streams as a novel approach to fitting properties of these structures in the disk.

Exploring how to modify and improve the code would be useful in the future. Our fits are very time consuming and computationally expensive, and we have already discussed how adding even more parameters will be necessary. Machine learning methods which may be able to differentiate the output stream relative to the input subhalo parameters could dramatically improve these computation times. There are stream codes that employ this such as SSTRAX, developed by Alvey et al. (2023). This is built on JAX (Bradbury et al., 2018), and the autodiff function or use of sstrax could potentially be used for our subhalo impacts to see if this could improve computation times while maintaining good fits.

The results of Chapter 3 in this thesis also have far reaching consequences for other streams. For example, the GD-1 stream has a spur like feature, which potentially could be fit using our older impact we attempted to fit to AAU, which has stars drift down the stream and connect to the track. This is also not necessarily intrusive on other fits to different aspects of the GD-1 stream, due to how the kinematics and proper motions of the stream are otherwise fairly unchanged. This will not only be limited to the AAU and GD-1 stream however, and continuing to fit streams can potentially reveal different kinds of interactions that affect streams in their own unique ways compared to our 2 scenarios explored here. This could lead to new ways to consider fitting stellar streams, and could be made possible with the broader views of streams we will get with future surveys. Using data from surveys including 4MOST (de Jong et al., 2012), LSST (Ivezić et al., 2019) and DESI (DESI Collaboration et al., 2016a,b) have the potential to dramatically improve the fits to these streams while also better understanding the nature of subhalo-stream interactions.

For a stream such as AAU and its multiple features, we would also aim to incorporate additional methods such as in Bovy et al. (2017a), which employs random statistical sampling in a realistic population of subhaloes. While our method could be used for the AAU kink itself, we could apply this statistical approach to our perturbed stream to then fit the remaining AAU features such as the broadening of the stream at higher ϕ_1 and match our fit to the AAU power spectrum. While the method in Bovy et al. (2017a) uses the analytic impulse approximation, which is less accurate than our own, it can suit fitting the less drastic features to avoid the time consuming approach such as our method such as smaller scale density fluctuations along the track.

Bibliography

Abramowitz M., Stegun I. A., 1972, Handbook of Mathematical Functions

Alvey J., Gerdes M., Weniger C., 2023, sstrax: Fast stellar stream modelling in JAX, Astrophysics Source Code Library, record ascl:2306.008 (ascl:2306.008)

Amorisco N. C., Gómez F. A., Vegetti S., White S. D. M., 2016, MNRAS, 463, L17

Banik N., Bovy J., 2019, MNRAS, 484, 2009

Banik N., Bovy J., Bertone G., Erkal D., de Boer T. J. L., 2021a, MNRAS, 502, 2364

Banik N., Bovy J., Bertone G., Erkal D., de Boer T. J. L., 2021b, MNRAS, 502, 2364

Banik N., Bovy J., Bertone G., Erkal D., de Boer T. J. L., 2021c, J. Cosmology Astropart. Phys., 2021, 043

Bar-Or B., Fouvry J.-B., Tremaine S., 2019, ApJ, 871, 28

Bellazzini M., Ferraro F. R., Ibata R., 2003, AJ, 125, 188

Belokurov V., et al., 2006, ApJ, 642, L137

Belokurov V., et al., 2007, ApJ, 658, 337

Belokurov V., Erkal D., Evans N. W., Koposov S. E., Deason A. J., 2018, MNRAS, 478, 611

Benjamin R. A., et al., 2005, ApJ, 630, L149

Berezinsky V., Dokuchaev V., Eroshenko Y., 2003, Phys. Rev. D, 68, 103003

Bernard E. J., et al., 2016, MNRAS, 463, 1759

Binney J., Gerhard O., Spergel D., 1997, MNRAS, 288, 365

Bittner A., Gadotti D. A., Elmegreen B. G., Athanassoula E., Elmegreen D. M., Bosma A., Muñoz-Mateos J., 2020, in Valluri M., Sellwood J. A., eds, Vol. 353, Galactic Dynamics in the Era of Large Surveys. pp 140–143 (`arXiv:1910.01139`), doi:10.1017/S1743921319008160

Bland-Hawthorn J., Freeman K., 2000, Science, 287, 79

Bode P., Ostriker J. P., Turok N., 2001a, ApJ, 556, 93

Bode P., Ostriker J. P., Turok N., 2001b, ApJ, 556, 93

Bonaca A., Geha M., Kallivayalil N., 2012, ApJ, 760, L6

Bonaca A., Hogg D. W., Price-Whelan A. M., Conroy C., 2019, ApJ, 880, 38

Bond J. R., Szalay A. S., 1983a, ApJ, 274, 443

Bond J. R., Szalay A. S., 1983b, ApJ, 274, 443

Bournaud F., et al., 2007, Science, 316, 1166

Bovy J., Erkal D., Sanders J. L., 2017a, MNRAS, 466, 628

Bovy J., Erkal D., Sanders J. L., 2017b, MNRAS, 466, 628

Bovy J., Leung H. W., Hunt J. A. S., Mackereth J. T., García-Hernández D. A., Roman-Lopes A., 2019, MNRAS, 490, 4740

Bradbury J., et al., 2018, JAX: composable transformations of Python+NumPy programs, `http://github.com/google/jax`

Buckley M. R., Peter A. H. G., 2018, Phys. Rep., 761, 1

Bullock J. S., Boylan-Kolchin M., 2017, ARA&A, 55, 343

Burkert A., 2020, ApJ, 904, 161

Carlberg R. G., 2009, ApJ, 705, L223

Carlberg R. G., 2012, ApJ, 748, 20

Carlin J. L., Yam W., Casetti-Dinescu D. I., Willett B. A., Newberg H. J., Majewski S. R., Girard T. M., 2012, ApJ, 753, 145

Carraro G., Zinn R., Moni Bidin C., 2007, A&A, 466, 181

Chabrier G., 2005, in Corbelli E., Palla F., Zinnecker H., eds, Astrophysics and Space Science Library Vol. 327, The Initial Mass Function 50 Years Later. p. 41 (`arXiv:astro-ph/0409465`), doi:10.1007/978-1-4020-3407-7_5

Chakrabarti S., et al., 2020, ApJ, 902, L28

Choi J., Dotter A., Conroy C., Cantiello M., Paxton B., Johnson B. D., 2016, ApJ, 823, 102

Churchwell E., et al., 2009, PASP, 121, 213

Clowe D., Bradač M., Gonzalez A. H., Markevitch M., Randall S. W., Jones C., Zaritsky D., 2006, ApJ, 648, L109

Collins M. L. M., et al., 2011, MNRAS, 417, 1170

Conroy C., Naidu R. P., Garavito-Camargo N., Besla G., Zaritsky D., Bonaca A., Johnson B. D., 2021, Nature, 592, 534

Cox D. P., Gómez G. C., 2002, ApJS, 142, 261

DESI Collaboration et al., 2016a, arXiv e-prints, p. arXiv:1611.00036

DESI Collaboration et al., 2016b, arXiv e-prints, p. arXiv:1611.00037

Da Costa G. S., Armandroff T. E., 1995, AJ, 109, 2533

Dark Energy Survey Collaboration et al., 2016, MNRAS, 460, 1270

Davis M., Efstathiou G., Frenk C. S., White S. D. M., 1985, ApJ, 292, 371

Debattista V. P., Sellwood J. A., 1998, ApJ, 493, L5

Dehnen W., 1999, ApJ, 524, L35

Dehnen W., 2000, AJ, 119, 800

Dehnen W., Binney J., 1998a, MNRAS, 294, 429

Dehnen W., Binney J. J., 1998b, MNRAS, 298, 387

Diemand J., Moore B., Stadel J., 2005, Nature, 433, 389

Dotter A., 2016, ApJS, 222, 8

Du X., Behrens C., Niemeyer J. C., 2017, MNRAS, 465, 941

Duffau S., Zinn R., Vivas A. K., Carraro G., Méndez R. A., Winnick R., Gallart C., 2006, ApJ, 636, L97

Elmegreen D. M., Elmegreen B. G., 1995, ApJ, 445, 591

Elmegreen B. G., Elmegreen D. M., Leitner S. N., 2003, ApJ, 590, 271

Erkal D., Belokurov V., 2015a, MNRAS, 450, 1136

Erkal D., Belokurov V., 2015b, MNRAS, 454, 3542

Erkal D., Belokurov V. A., 2020, MNRAS, 495, 2554

Erkal D., Belokurov V., Bovy J., Sanders J. L., 2016, MNRAS, 463, 102

Erkal D., Koposov S. E., Belokurov V., 2017, MNRAS, 470, 60

Erkal D., et al., 2019, MNRAS, 487, 2685

Erkal D., et al., 2021, MNRAS, 506, 2677

Eskridge P. B., et al., 2000, AJ, 119, 536

Eyer L., et al., 2012, in Richards M. T., Hubeny I., eds, Vol. 282, From Interacting Binaries to Exoplanets: Essential Modeling Tools. pp 33–40 (`arXiv:1201.5140`), doi:10.1017/S1743921311026822

Fellhauer M., et al., 2007, MNRAS, 375, 1171

Fiacconi D., Madau P., Potter D., Stadel J., 2016, ApJ, 824, 144

Finkbeiner D. P., et al., 2016, ApJ, 822, 66

Flores R. A., Primack J. R., 1994, ApJ, 427, L1

Foreman-Mackey D., Hogg D. W., Lang D., Goodman J., 2013, PASP, 125, 306

Freeman K., Bland-Hawthorn J., 2002, ARA&A, 40, 487

Gaia Collaboration et al., 2018a, A&A, 616, A1

Gaia Collaboration et al., 2018b, A&A, 616, A12

Gaia Collaboration et al., 2023, A&A, 674, A1

Garrett K., Dūda G., 2011, Advances in Astronomy, 2011, 968283

Gentile G., Famaey B., Combes F., Kroupa P., Zhao H. S., Tiret O., 2007, A&A, 472, L25

Gibbons S. L. J., Belokurov V., Evans N. W., 2014, MNRAS, 445, 3788

Gibbons S. L. J., Belokurov V., Evans N. W., 2017, MNRAS, 464, 794

Gieles M., Erkal D., Antonini F., Balbinot E., Peñarrubia J., 2021, Nature Astronomy, 5, 957

Gilman D., Birrer S., Nierenberg A., Treu T., Du X., Benson A., 2020, MNRAS, 491, 6077

Gilmore G., Wyse R. F. G., Kuijken K., 1989, ARA&A, 27, 555

Gómez F. A., Besla G., Carpintero D. D., Villalobos Á., O'Shea B. W., Bell E. F., 2015, ApJ, 802, 128

Gonzalez O. A., Rejkuba M., Zoccali M., Valenti E., Minniti D., Schultheis M., Tobar R., Chen B., 2012, A&A, 543, A13

Grillmair C. J., 2006, ApJ, 645, L37

Grillmair C. J., Dionatos O., 2006a, ApJ, 643, L17

Grillmair C. J., Dionatos O., 2006b, ApJ, 643, L17

Grillmair C. J., Hetherington L., Carlberg R. G., Willman B., 2015, ApJ, 812, L26

Hannestad S., 2004, Phys. Rev. D, 70, 043506

Hannestad S., Scherrer R. J., 2000, Phys. Rev. D, 62, 043522

Harris W. E., 2010, arXiv e-prints, p. arXiv:1012.3224

Harris W. E., Harris G. L. H., Alessi M., 2013, ApJ, 772, 82

Hattori K., Erkal D., Sanders J. L., 2016, MNRAS, 460, 497

Hayashi E., Navarro J. F., 2006, MNRAS, 373, 1117

Helmi A., 2008, A&ARv, 15, 145

Helmi A., White S. D. M., de Zeeuw P. T., Zhao H., 1999, Nature, 402, 53

Helmi A., Babusiaux C., Koppelman H. H., Massari D., Veljanoski J., Brown A. G. A., 2018, Nature, 563, 85

Hernquist L., 1990, ApJ, 356, 359

Hezaveh Y. D., et al., 2016, ApJ, 823, 37

Hilmi T., et al., 2020, MNRAS, 497, 933

Hilmi T., et al., 2024, arXiv e-prints, p. arXiv:2404.02953

Hu W., Barkana R., Gruzinov A., 2000, Phys. Rev. Lett., 85, 1158

Hubble E. P., 1922, ApJ, 56

Hubble E., 1926, Contributions from the Mount Wilson Observatory / Carnegie Institution of Washington, 324, 1

Hui L., Ostriker J. P., Tremaine S., Witten E., 2017, Phys. Rev. D, 95, 043541

Ibata R. A., Gilmore G., Irwin M. J., 1994, Nature, 370, 194

Ibata R., Irwin M., Lewis G. F., Stolte A., 2001, ApJ, 547, L133

Ibata R. A., Lewis G. F., Irwin M. J., Quinn T., 2002, MNRAS, 332, 915

Ibata R. A., Lewis G. F., Thomas G., Martin N. F., Chapman S., 2017, ApJ, 842, 120

Ibata R. A., Malhan K., Martin N. F., 2019, ApJ, 872, 152

Iršič V., et al., 2017, Phys. Rev. D, 96, 023522

Irwin M., 1999, in Whitelock P., Cannon R., eds, Vol. 192, The Stellar Content of Local Group Galaxies. p. 409

Ivezić Ž., et al., 2019, ApJ, 873, 111

Jethwa P., Erkal D., Belokurov V., 2018, MNRAS, 473, 2060

Jin S., Lynden-Bell D., 2007, MNRAS, 378, L64

Johnson B. D., et al., 2020, ApJ, 900, 103

Johnston K. V., Sackett P. D., Bullock J. S., 2001, ApJ, 557, 137

Johnston K. V., Spergel D. N., Haydn C., 2002, ApJ, 570, 656

Juric M., 2012, LSD: Large Survey Database framework, Astrophysics Source Code Library, record ascl:1209.003 (ascl:1209.003)

Kalirai J. S., et al., 2010, ApJ, 711, 671

Kauffmann G., White S. D. M., Guiderdoni B., 1993, MNRAS, 264, 201

Kawasaki M., Kohri K., Sugiyama N., 2000, Phys. Rev. D, 62, 023506

King I., 1962, AJ, 67, 471

Klypin A., Kravtsov A. V., Valenzuela O., Prada F., 1999, ApJ, 522, 82

Koposov S., 2021, segasai/minimint: Minimint 0.3.0, doi:10.5281/zenodo.5610692, `https://doi.org/10.5281/zenodo.5610692`

Koposov S. E., Rix H.-W., Hogg D. W., 2010, ApJ, 712, 260

Koposov S. E., Irwin M., Belokurov V., Gonzalez-Solares E., Yoldas A. K., Lewis J., Metcalfe N., Shanks T., 2014, MNRAS, 442, L85

Koposov S. E., et al., 2023, MNRAS, 521, 4936

Küpper A. H. W., MacLeod A., Heggie D. C., 2008, MNRAS, 387, 1248

Küpper A. H. W., Kroupa P., Baumgardt H., Heggie D. C., 2010, MNRAS, 401, 105

Lagadec E., Zijlstra A. A., Mauron N., Fuller G., Josselin E., Sloan G. C., Riggs A. J. E., 2010, MNRAS, 403, 1331

Law D. R., Majewski S. R., 2010a, ApJ, 714, 229

Law D. R., Majewski S. R., 2010b, ApJ, 718, 1128

Law D. R., Majewski S. R., Johnston K. V., 2009, ApJ, 703, L67

Leaman R., 2012, AJ, 144, 183

Li T., S5 Collaboration 2021, Southern Stellar Stream Spectroscopic Survey: The First Public Data Release, doi:10.5281/zenodo.4695135, `https://doi.org/10.5281/zenodo.4695135`

Li T. S., et al., 2019, MNRAS, 490, 3508

Li T., Koposov S., Erkal D., S5 Collaboration 2020, in American Astronomical Society Meeting Abstracts #235. p. 316.06

Li T. S., et al., 2021, ApJ, 911, 149

Li Z., Shen J., Gerhard O., Clarke J. P., 2022, ApJ, 925, 71

Lilleengen S., et al., 2023, MNRAS, 518, 774

Lin C. C., Shu F. H., 1964, ApJ, 140, 646

Lindblad B., 1959, Handbuch der Physik, 53, 21

Lintott C., et al., 2011a, MNRAS, 410, 166

Lintott C., et al., 2011b, MNRAS, 410, 166

Long K., Murali C., 1992, ApJ, 397, 44

Lovell M. R., et al., 2012, MNRAS, 420, 2318

Lovell M. R., Frenk C. S., Eke V. R., Jenkins A., Gao L., Theuns T., 2014, MNRAS, 439, 300

Lynden-Bell D., Lynden-Bell R. M., 1995, MNRAS, 275, 429

Majewski S. R., 1993, ARA&A, 31, 575

Majewski S., 2003, in Piotto G., Meylan G., Djorgovski S. G., Riello M., eds, Astronomical Society of the Pacific Conference Series Vol. 296, New Horizons in Globular Cluster Astronomy. p. 447

Majewski S. R., Hawley S. L., Munn J. A., 1996a, in Morrison H. L., Sarajedini A., eds, Astronomical Society of the Pacific Conference Series Vol. 92, Formation of the Galactic Halo...Inside and Out. p. 119

Majewski S. R., Munn J. A., Hawley S. L., 1996b, ApJ, 459, L73

Majewski S. R., Skrutskie M. F., Weinberg M. D., Ostheimer J. C., 2003, ApJ, 599, 1082

Majewski S. R., Nidever D. L., Smith V. V., Damke G. J., Kunkel W. E., Patterson R. J., Bizyaev D., García Pérez A. E., 2012, ApJ, 747, L37

Malhan K., Ibata R. A., 2018, MNRAS, 477, 4063

Malhan K., Ibata R. A., Martin N. F., 2018, MNRAS, 481, 3442

Malhan K., Valluri M., Freese K., 2020, arXiv e-prints, p. arXiv:2005.12919

Marinova I., Jogee S., 2007, ApJ, 659, 1176

Marsh D. J. E., Silk J., 2014, MNRAS, 437, 2652

Martin N. F., Ibata R. A., Irwin M. J., Chapman S., Lewis G. F., Ferguson A. M. N., Tanvir N., McConnachie A. W., 2006, MNRAS, 371, 1983

Martin C., Carlin J. L., Newberg H. J., Grillmair C., 2013, ApJ, 765, L39

Massari D., Koppelman H. H., Helmi A., 2019, A&A, 630, L4

Mateu C., 2023, MNRAS, 520, 5225

Mathewson D. S., Cleary M. N., Murray J. D., 1974, ApJ, 190, 291

Mauron N., Azzopardi M., Gigoyan K., Kendall T. R., 2004, A&A, 418, 77

Mauron N., Kendall T. R., Gigoyan K., 2005, A&A, 438, 867

Mauron N., Gigoyan K. S., Kendall T. R., 2007, A&A, 475, 843

McConnachie A. W., 2012, AJ, 144, 4

McGough D. P., Evans N. W., Sanders J. L., 2020, MNRAS, 493, 2676

McMillan P. J., 2017, MNRAS, 465, 76

Milgrom M., 1983, ApJ, 270, 365

Minchev I., 2016, Astronomische Nachrichten, 337, 703

Mirabal N., Bonaca A., 2021, J. Cosmology Astropart. Phys., 2021, 033

Mocz P., et al., 2019, Phys. Rev. Lett., 123, 141301

Moliné Á., Sánchez-Conde M. A., Palomares-Ruiz S., Prada F., 2017, MNRAS, 466, 4974

Monari G., Famaey B., Siebert A., 2016, MNRAS, 457, 2569

Moore B., 1994, Nature, 370, 629

Moore B., Ghigna S., Governato F., Lake G., Quinn T., Stadel J., Tozzi P., 1999, ApJ, 524, L19

Nadler E. O., et al., 2021, Phys. Rev. Lett., 126, 091101

Navarro J. F., Frenk C. S., White S. D. M., 1997, ApJ, 490, 493

Newberg H. J., Carlin J. L., 2016, Tidal Streams in the Local Group and Beyond. Vol. 420, doi:10.1007/978-3-319-19336-6,

Newberg H. J., Yanny B., 2006, in Journal of Physics Conference Series. pp 195–204 (`arXiv:astro-ph/0507671`), doi:10.1088/1742-6596/47/1/024

Newberg H. J., Willett B. A., Yanny B., Xu Y., 2010, ApJ, 711, 32

Odenkirchen M., et al., 2001a, ApJ, 548, L165

Odenkirchen M., et al., 2001b, ApJ, 548, L165

Odenkirchen M., et al., 2003, AJ, 126, 2385

Oh S.-H., de Blok W. J. G., Brinks E., Walter F., Kennicutt Robert C. J., 2011, AJ, 141, 193

Oh S.-H., et al., 2015, AJ, 149, 180

Outmezguine N. J., Boddy K. K., Gad-Nasr S., Kaplinghat M., Sagunski L., 2023, MNRAS, 523, 4786

Peñarrubia J., Petersen M. S., 2021, MNRAS, 508, L26

Peñarrubia J., Ludlow A. D., Chanamé J., Walker M. G., 2016, MNRAS, 461, L72

Pearson S., Price-Whelan A. M., Johnston K. V., 2017, Nature Astronomy, 1, 633

Petersen M. S., Peñarrubia J., 2021, Nature Astronomy, 5, 251

Petersen M. S., Weinberg M. D., Katz N., 2019, arXiv e-prints, p. arXiv:1903.08203

Pietrzyński G., et al., 2019, Nature, 567, 200

Plummer H. C., 1911, MNRAS, 71, 460

Portail M., Gerhard O., Wegg C., Ness M., 2017a, MNRAS, 465, 1621

Portail M., Wegg C., Gerhard O., Ness M., 2017b, MNRAS, 470, 1233

Prada J., Forero-Romero J. E., Grand R. J. J., Pakmor R., Springel V., 2019, MNRAS, 490, 4877

Price-Whelan A. M., Bonaca A., 2018, ApJ, 863, L20

Price-Whelan A. M., Sesar B., Johnston K. V., Rix H.-W., 2016, ApJ, 824, 104

Queiroz F., 2017, in Proceedings of the European Physical Society Conference on High Energy Physics. 5-12 July. p. 80 (`arXiv:1711.02463`)

Quillen A. C., 2002, AJ, 124, 924

Raffelt G., Silk J., 1987, Physics Letters B, 192, 65

Rubin V. C., Thonnard N. T., Ford W. K. J., 1982a, AJ, 87, 477

Rubin V. C., Ford W. K. J., Thonnard N., Burstein D., 1982b, ApJ, 261, 439

Sanders R. H., McGaugh S. S., 2002, ARA&A, 40, 263

Sanders J. L., Bovy J., Erkal D., 2016, MNRAS, 457, 3817

Sanders J. L., Smith L., Evans N. W., 2019, MNRAS, 488, 4552

Schneider A., Smith R. E., Macciò A. V., Moore B., 2012, MNRAS, 424, 684

Schutz K., 2020, Phys. Rev. D, 101, 123026

Scowcroft V., Freedman W. L., Madore B. F., Monson A., Persson S. E., Rich J., Seibert M., Rigby J. R., 2016, ApJ, 816, 49

Sellwood J. A., Trick W. H., Carlberg R. G., Coronado J., Rix H.-W., 2019, MNRAS, 484, 3154

Shanks T., et al., 2013, The Messenger, 154, 38

Shanks T., et al., 2015, MNRAS, 451, 4238

Sheffield A. A., et al., 2012, ApJ, 761, 161

Shipp N., et al., 2018, ApJ, 862, 114

Shipp N., et al., 2019, ApJ, 885, 3

Shipp N., et al., 2021, ApJ, 923, 149

Siegal-Gaskins J. M., Valluri M., 2008, ApJ, 681, 40

Silverwood H., Easther R., 2019, Publ. Astron. Soc. Australia, 36, e038

Simon J. D., 2019, ARA&A, 57, 375

Simon J. D., Geha M., 2007, ApJ, 670, 313

Slater C. T., et al., 2013, ApJ, 762, 6

Slater C. T., et al., 2014, ApJ, 791, 9

Sofue Y., 2013, PASJ, 65, 118

Sofue Y., Rubin V., 2001, ARA&A, 39, 137

Somerville R. S., Davé R., 2015, ARA&A, 53, 51

Speagle J. S., 2020, MNRAS, 493, 3132

Spergel D. N., Steinhardt P. J., 2000, Phys. Rev. Lett., 84, 3760

Springel V., 2005, MNRAS, 364, 1105

Springel V., Frenk C. S., White S. D. M., 2006, Nature, 440, 1137

Springel V., et al., 2008, MNRAS, 391, 1685

Steigman G., Turner M. S., 1985, Nuclear Physics B, 253, 375

Struck C., 2015, MNRAS, 450, 2217

Tayler R. J. R. J., 1993, Galaxies, structure and evolution

The Dark Energy Survey Collaboration 2005, arXiv e-prints, pp astro–ph/0510346

Thomas G. F., Famaey B., Ibata R., Lüghausen F., Kroupa P., 2017, A&A, 603, A65

Thomas G. F., Famaey B., Ibata R., Renaud F., Martin N. F., Kroupa P., 2018, A&A, 609, A44

Totten E. J., Irwin M. J., 1998, MNRAS, 294, 1

Tulin S., Yu H.-B., 2018, Phys. Rep., 730, 1

Tyson J. A., Kochanski G. P., Dell'Antonio I. P., 1998, ApJ, 498, L107

Vasiliev E., Belokurov V., 2020, MNRAS, 497, 4162

Vasiliev E., Belokurov V., Erkal D., 2020, MNRAS,

Vasiliev E., Belokurov V., Erkal D., 2021, MNRAS, 501, 2279

Vegetti S., Lagattuta D. J., McKean J. P., Auger M. W., Fassnacht C. D., Koopmans L. V. E., 2012, Nature, 481, 341

Viel M., Becker G. D., Bolton J. S., Haehnelt M. G., 2013, Phys. Rev. D, 88, 043502

Vivas A. K., et al., 2001, ApJ, 554, L33

Watkins L. L., van der Marel R. P., Bennet P., 2024, ApJ, 963, 84

Wegg C., Gerhard O., Portail M., 2015, MNRAS, 450, 4050

Weinberg D. H., Bullock J. S., Governato F., Kuzio de Naray R., Peter A. H. G., 2015, Proceedings of the National Academy of Science, 112, 12249

White S. D. M., Frenk C. S., 1991, ApJ, 379, 52

White S. D. M., Rees M. J., 1978, MNRAS, 183, 341

Wilkinson M. I., Evans N. W., 1999, MNRAS, 310, 645

Willman B., Strader J., 2012, AJ, 144, 76

Yanny B., et al., 2000, ApJ, 540, 825

Yoon J. H., Johnston K. V., Hogg D. W., 2011, ApJ, 731, 58

York D. G., et al., 2000, AJ, 120, 1579

Zwicky F., 1933, Helvetica Physica Acta, 6, 110

de Blok W. J. G., McGaugh S. S., Bosma A., Rubin V. C., 2001, ApJ, 552, L23

de Jong R. S., et al., 2012, in McLean I. S., Ramsay S. K., Takami H., eds, Society of Photo-Optical Instrumentation Engineers (SPIE) Conference Series Vol. 8446, Ground-based and Airborne Instrumentation for Astronomy IV. p. 84460T (`arXiv:1206.6885`), doi:10.1117/12.926239

de Vaucouleurs G., 1958, ApJ, 127, 487

van der Marel R. P., Kallivayalil N., 2014, ApJ, 781, 121

von Hoerner S., 1957, ApJ, 125, 451